Marine gravity and bathymetry modelling from recent satellite altimetry

Abulaitijiang, Adili

Publication date:
2019

Document Version
Publisher's PDF, also known as Version of record

Marine gravity and bathymetry modelling from recent satellite altimetry

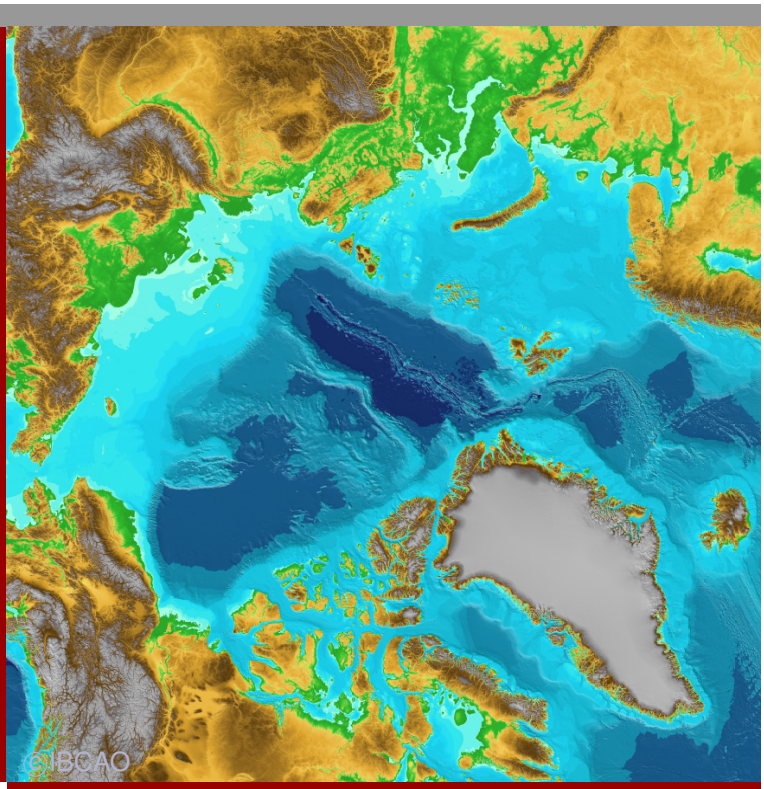

Adili Abulaitijiang
PhD Thesis
March, 2019

DTU Space
National Space Institute

Marine gravity and bathymetry modelling from recent satellite altimetry

Adili Abulaitijiang
National Space Institute
PhD Thesis, Kgs. Lyngby, March, 2019

http://www.space.dtu.dk

Dansk abstrakt

Marin tyngder er blevet bestemt fra satellite altimetry i mere end 20 år. Nøjagtigheden af afstandsbestemmelsen og den rumlige tæthed har vist sig at være de væsentlige faktorer som begrænser nøjagtigheden af altimetriske tyngdefelter. Siden opsendelsen af CryoSat-2 i 2010 er både afstandsbestemmelsen og den rumlige tæthed er blevet forbedret i forhold til ældre satellitter.

Ved at kombinere observationer fra Cryosat-2 med data fra de geodætiske missioner fra Jason-1 og SARAL/Altika er det første formål med afhandlingen at undersøge og udvikle forbedrede metoder til bestemmelse af tyngdefeltet i den kystnære zone, hvor tyngdefeltsbestemmelsen fra altimetri traditionelt er problematisk. Forbedrede metoder som "least squares collocation" er blevet undersøgt da det også kan give fejlestimater. Tilsvarende er CryoSat-2 observationer fra forskellige retrackere blevet undersøgt. Endelig er "Residual Terrain Modellering" (RTM) blevet undersøgt og udviklet således at det kan benyttes til reduktion af højdeanomalierne og derved i bestemmelsen af tyngdefeltet i kystzonen. Opløsningen af den digitale højde model (inklusiv bathymetrien) har dog vist sig at være en begrænsende faktor i brugen af RTM korrektionen. Resultater fra en case-studie i Middelhavet viser at RTM kun er delvis effektiv i at reduceret højde anomalierne og forbedre tyngdefeltet. Problemerne skyldes formodentlig at sedimenter i de dybe dele af oceanet sætter tvivl ved metodens brug af konstant densitet. Brugen af data retracket med "narrow peak" retrackeren gav det højst antal punkter og bedste præcision med 2.07 mGal i studiet i Middelhavet. I det andet case-studie i Indonesien sås en forbedret reduktion af højdeanomalierne med benyttelse af RTM korrektionen. Tyngdefeltet blev også forbedret men studiet viste problematisk residuale langbølgede signaler i Earth Gravitational Model 2008 (EGM08).

Det andet formål med studiet har omhandlet udvikling af metoder til bathymetri bestemmelse. State of the art bathymetrien for Arktis (IBCAOv3) er konstrueret ud fra spredte skibs målinger og digitaliserede dybde konturer. Bathymetrien kan bestemmes ved at invertere et nedad-fortsat tyngdefelt i et begrænset bølgelængde område. Det original filter fra *Smith and Sandwell* (1994) som bestemte dybder I 15−160 km intervallet er her blevet modificeret til kun at bestemme havdybderne i 15−57 km intervallet og samtidig er bestemmelse af skalerings-faktoren forbedret.

I dette studie præsenteres den første Arktiske bathymetri bestemt ud fra tyngdeinversion af et altimetrisk tyngdefelt (DTU17). Validering med to uafhængige multi-beam opmålinger resulterede I en absolut difference på hhv. 50.8 m and 36.9 m, med en standard afvigelse på hhv 119.5 m and 77.6 m. Dette er en forbedring på mere end 50% i sammenligning med brug af det originale filter. Bathymetri prædiktion viser også god overensstemmelse med skibs målinger. En 1000 meter dyb dal i Chukchi plateauet i "state of the art" bathymetrien er således fjernet i

den altimetriske bathymetri. Bathymetri inversion har derfor et stort potentiale i specielt de områder af det Artiske ocean hvor der ikke findes opmålinger fra skib i den næste version Artiske bathymetri.

Abstract

Marine gravity has been modelled from satellite radar altimetry for more than two decades. Range precision and spatial coverage of altimetry observations are the main factors limiting the accuracy of predicted gravity field. Since 2010, CryoSat-2 has been measuring sea surface heights with a 369-day repeat cycle. By combining these high precision and dense CryoSat-2 observations with Jason-1 and SARAL/Altika geodetic mission data, the accuracy of marine gravity is expected to improve not only over the open ocean, but also near the coastal zone.

This study aims to improve the gravity field near the coastal zone using least square collocation algorithm. CryoSat-2 observations obtained from different retrackers are used. Residual Terrain Modelling (RTM) is considered during the modelling process. The resolution of digital topography (including bathymetry) is the limiting factor in the application of RTM. Results from Mediterranean case study show that RTM is partly effective in reducing the residual height anomalies. Sediments in the deep ocean and constant density assumptions are believed to be the error sources. Prediction error for gravity anomalies is better than 4 mGal along the coast. Gravity field predicted from altimetry data with the most coastal coverage and retracked with the narrow primary peak retracker gives the best precision of 2.07 mGal. In the Indonesian case study, height anomalies are reduced by removing RTM effects. Strong signal in the remaining residual field suggests long wavelength problems from Earth Gravitational Model 2008 (EGM08).

Existing Arctic bathymetry is compiled from sparse ship soundings and digitized depth contours. Sea floor topography can be inverted from downward continued marine gravity anomalies in a limited wavelength band. Based on the original filter presented in *Smith and Sandwell* (1994), a modified version, which limits the prediction to the 15−57 km wavelength band, is proposed and successfully used for bathymetry inversion from gravity anomalies.

In this study, the first-ever Arctic bathymetry inverted from DTU17 marine gravity model is presented. Validation with two independent multi-beam ship sounding surveys give an absolute mean difference of 50.8 m and 36.9 m, with 119.5 m and 77.6 m standard deviations, respectively. The use of modified filter yield an improvement of more than 50% compared to the original filter which predicts topography in the 15−160 km band. Predicted bathymetry using modified filter shows good agreement with ship soundings. A problematic $\sim$ 1000 m deep valley in existing bathymetry map is resolved over the Chukchi plateau. Predicted bathymetry from gravity can be used to fill the gaps where there are no ship soundings in the next generation of Arctic bathymetry.

Preface

This thesis is submitted in fulfillment of the requirements for obtaining a PhD degree at DTU Space, National Space Institute, Technical University of Denmark. The research was carried out under supervision of Ole B. Andersen, Per Knudsen and Lars Stenseng.

The PhD project was partly funded by the National Geospatial-Intelligence Agency (NGA), USA. The project is partly, a contribution to DTU Space long term commitment to prepare altimetric gravity to develop the Earth Gravitational Model EGM2020. This model is scheduled for release in 2020.

Started in December 2015, I was a freshmen in the field of marine gravity modelling. I am thankful to to my supervisors for guiding me into the field. The two case studies on coastal marine gravity modelling presented in this thesis, are several of the many conducted during the PhD study. The work completed during the PhD study was presented in two publications that are under revision. The Arctic bathymetry prediction results are promising and I hope it can supplement the development of the next generation Arctic Ocean bathymetry.

Adili Abulaitijiang
Lyngby, March 2019.

Acknowledgment

First of all, I would like to express my deepest gratitude to my supervisor Prof. Ole Baltazar Andersen, for his continuous support, patience and immense knowledge. His guidance and experience was of constant help during my research. His constant encouragement has given me confidence and power to accomplish the work. I am deeply grateful for his reviews and comments during publication writing. I really enjoyed working with him during the past 3 years and appreciate his always-on availability for questions and discussions.

A special thanks my other supervisors Prof. Per Knudsen for his support and discussions on the least square collocation and applications and Associate Prof. Lars Stenseng for valuable discussions and support on processed altimetry data and maintenance of the in-house database so valuable to this study.

During the PhD study, I had the opportunity to visit the distinguished professors in different institutes abroad. I would like to thank Prof. Riccardo Barzaghi at POLIMI for his guidance and discussion on covariance model fitting during my visit and involvement in the GEOMED2 project. I would like to thank Prof. Will Featherstone at Curtin University for the discussions on RTM and topographic potential models during my visit to him. Spatial thanks to Prof. David Sandwell at UCSD, for hosting me for a period and for sharing all his experience on the bathymetry prediction.

I would also like to extend my thanks to all my present and former colleagues at Geodesy department and staff at DTU Space for creating a pleasant working atmosphere. I am thankful to Hu Xiao for his advice on robust linear regression techniques. Spatial thanks to Dr. Tim E. Jensen for manuscript proofreading.

Finally, I would like to express my sincere gratitude to my wife, Ayimunishagu Abulimiti, friends, and most importantly, my beloved parents' support, encouragements and care throughout the PhD study. Life would have been hard without their persistent support.

The research project was partly funded by the National Geospatial-Intelligence Agency (NGA), USA. Also the ESA project CryoSat Plus for Ocean (CP4O) partly supported an initial part of this research. I am thankful to Otto Mønsteds Fond and Idella Fond for supporting my external stays and partially covering travel expenses. All financial support are gratefully acknowledged.

Acronyms

AltiKa	Ka band altimeter (on board the SARAL mission)
CNES	Centre National d'Etudes Spatiales
DEM	Digital Elevation Model
DORIS	Doppler Orbitography and Radiopositioning Integrated by Satellite
ECS	Extended Continental Shelf
EGM	Earth Gravitational Model
ERS	European Remote Sensing
ESA	European Space Agency
FFT	Fast Fourier Transform
GEBCO	General Bathymetric Chart of the Oceans
GMT	Generic Mapping Tool
GPOD	Grid Processing On Demand
GPS	Global Positioning System
IBCAO	International Bathymetric Chart of the Arctic Ocean
LARS	Lars Altimetry Retracking System
LRM	Low Resolution Mode
LSC	Least Square Collocation
LSF	Least Square Fitting
MAD	Median Absolute Deviation
MDT	Mean Dynamic Topography
NPP	Narrow Primary Peak (retracker)
OCOG	Offset Centre of Gravity
PRF	Pulse Repetition Frequency
RADS	Radar Altimeter Database System
RANSAC	Random Sample Consensus
RMS	Root Mean Square
RTM	Residual Terrain Modelling
SAMOSA	SAR Altimetry MOde Studies and Applications
SAR	Synthetic Aperture Radar
SARin	Synthetic Aperture Radar interferometer
SARAL	Satellite with ARgos and ALtiKa
SID	Source IDentification (grid)
SIRAL	Synthetic Aperture Interferometric Radar Altimeter
SRTM	Shuttle Radar Topography Mission
SSH	Sea Surface Height

Contents

List of Figures

List of Tables

Chapter 1

Introduction

1.1 Motivation

Regional gravity field modelling is of great importance for refining the Earth Gravitational Model (EGM). Radar altimetry waveforms near the coastal regions are frequently contaminated by reflections from land due to the large footprints of conventional satellites (e.g., TOPEX, EnviSat, ERS-1/2 and Jason series). This resulted in less reliable sea surface height measurements and data gaps near the coast. The recent altimetry missions CryoSat-2 (*Wingham et al.*, 2006) and SARAL/Altika (*Verron et al.*, 2015) have higher along track resolution and precision, which provides valuable observations close to the coast. In combination with Jason-1 geodetic mission data, coastal marine gravity can be improved.

Current global bathymetry maps predicted from gravity anomalies only go up to latitude 80°N (*Becker et al.*, 2009). At higher latitudes, bathymetry has not been predicted from gravity, due to the accuracy of marine gravity. With improved gravity field of the Arctic Ocean, the first-ever Arctic bathymetry predicted from gravity

can be developed using the correlation between gravity and topography.

1.2 Previous studies

1.2.1 Marine gravity modelling

Satellite altimetry measurements has been the main source in deriving the marine gravity field for more than two decades. Before 2010, Geosat and ER-1 geodetic mission data were the main source of the marine gravity models developed by *Andersen and Knudsen* (1998); *Andersen et al.* (2010); *Hwang et al.* (1998); *Sandwell and Smith* (2009); *Smith and Sandwell* (1997).

Andersen and Knudsen (2000) highlighted the role of satellite alimetry for gravity field modelling using the Geosat and ERS-1 geodetic missions in coastal regions characterized by narrow continental shelf and shallow sea water regions and found that its ability degraded within roughly 10 km of the shore.

The development of marine gravity field depends on altimetric range precision and data coverage. The improved range precision can be achieved by optimal retracking methods. *Hwang et al.* (2006) highlighted the importance of retracking in coastal marine gravity field modelling around Taiwan. *Sandwell and Smith* (2005) developed a retracking algorithm optimal for gravity field recovery and resulted in a factor of 1.5 improvement on ERS-1 range precision. *Garcia et al.* (2014) extended the retracking algorithm to other satellites and also resulted in a factor of 1.5 improvement. Since 2010, CryoSat-2 has been on a 369-day repeat orbit with the novel Synthetic Aperture Radar (SAR) mode operated on most of the coastal regions. The SAR mode acquisitions have higher along track resolution and better range precision than the conventional altimetry data. This makes CryoSat-2 optimal for gravity

field modelling. In addition, Jason-1 geodetic mission completed a 406-day repeat cycle in 2013. *Sandwell et al.* (2013, 2014) showed that the marine gravity derived by incorporating CryoSat-2 and Jason-1 resulted in a factor of 2 to 4 improvement compared to the gravity model derived from Geosat and ERS-1. Since July 2016, SARAL/Altika has been on the drifting phase orbit. The Ka-band radar altimeter range precision is better than that of Ku-band altimeters (*Smith*, 2015). All improvements in the range precisions will map into the improvement in the accuracy of predicted gravity field.

Studies have shown great improvement in coastal altimetric products by optimized data processing strategy (*Bouffard et al.*, 2008; *Gommenginger et al.*, 2011; *Vignudelli et al.*, 2005). *Passaro et al.* (2014, 2018) developed adapted waveform retrackers that performs well both for the oceans and coastal waveforms. These retrackers are dedicated for coastal altimetry applications, but the altimetry products can also be used for marine gravity modelling, particularly near the coastal zone.

State-of-the-art marine global gravity models from *Andersen et al.* (2010) and *Sandwell et al.* (2014) were developed by the Fast Fourier Transform (FFT) method (*Schwarz et al.*, 1990), which is fast and efficient for handling large amount of data. However, the data has to be gridded before applying FFT method, and the accuracy of the predicted gravity field can only be assessed by external datasets obtained from ship or airborne gravimetry. The Least Square Collocation (LSC) (*Moritz*, 1978) is a powerful technique in assimilating different data sources and predicting gravity field from observed quantities. LSC can handle data without gridding and give error estimates of predicted signal. The limitation of LSC is that the algorithm requires intensive computation power and is time consuming. LSC has been widely used for predicting gravity anomalies and geoid determination by combining different types of observations (*Hwang and Parsons*, 1995; *Rapp*, 1979; *Tscherning*, 1994;

Yildiz et al., 2012).

Residual terrain modelling (RTM) has been successfully used for signal reductions (*Forsberg*, 1984; *Forsberg and Tscherning*, 1981). However, RTM is rarely considered over the ocean or near the coastal zone. *Hirt* (2010, 2013) investigated the role of topography/bathymetry model in gravity field determination in coastal zones, and showed that the bathymetry data were beneficial for filling the gap between terrestrial and shipborne gravity data. *Tocho et al.* (2012) investigated the contribution of bathymetry models to the reduction of gravity anomalies in the southern ocean and concluded that it might be questionable to use a bathymetry model as a reference elevation model for RTM. The resolution of bathymetry models may play an important role but it may vary from region to region, depending on the availability of ship soundings.

The fundamental software programs to be used for gravity field modelling in this thesis are included in the GRAVSOFT package (*Forsberg et al.*, 2008). It includes modules for determining empirical covariances (EMPCOV), analytical covariance modelling (COVFIT) and LSC program (GEOCOL) that can be used to evaluate spherical harmonic series and derive gravity functionals (e.g., geoid, gravity anomaly and deflection of the verticals). In addition, GRAVSOFT package also has modules dedicated for computing terrain effects and RTM contributions.

1.2.2 Bathymetry prediction

More than 70% of the earth is covered by oceans and still huge fraction of the oceans are uncharted, leaving large data gaps between the survey lines. Sea floor depth can be mapped by echo sounding sonar devices mounted under the ships. However, it would take more than 200 years to map the global ocean with ship sounding (*Carron*

et al., 2001).

Dixon et al. (1983) demonstrated that seafloor topography can be predicted from marine gravity anomalies. *Smith and Sandwell* (1994) estimated the seafloor topography from marine gravity anomalies derived from Seasat, ERS-1 and Geosat geodetic mission data in the southern ocean and validated with ship soundings. The prediction is limited in the 15−160 km wavelength band. Due to isostatic compensation, at longer wavelengths(>160 km), topography is isostatically compensated (*Watts*, 1978). Shorter wavelength features(<15 km) of topography cannot be predicted from satellite derived gravity anomalies due to the gravity signal attenuation from sea floor to the sea surface. In geophysics, gravity inversion has been applied for the large-scale sub-crust geometry estimation and sediment thickness mapping, in combination with seismic soundings (*Alvey et al.*, 2008; *Engen et al.*, 2006; *Glebovsky et al.*, 2013).

The global bathymetry model was created by combining satellite-derived gravity anomalies and publicly accessible ship soundings (*Becker et al.*, 2009; *Smith and Sandwell*, 1997). General Bathymetric Chart of the Oceans (GEBCO) is a compilation of global and regional bathymetric models with land topography from digital elevation models. Bathymetry predicted from gravity anomalies has been used to supplement the development of global models by filling up the data gaps where there is no ship sounding (*Weatherall et al.*, 2015).

The Arctic Ocean bathymetry is not well surveyed due to the presence of sea ice and harsh climate. Campaigns to map the sea floor topography through ship sounding have been operated, but it only covers the very small fraction of the entire Arctic, and meanwhile it is very costly to operate. The International Bathymetric Chart of the Arctic Ocean (IBCAO)(*Jakobsson et al.*, 2000, 2008, 2012) is a compilation of sparse ship soundings in the Arctic Ocean and digitized depth charts. At high

latitudes, bathymetry was not predicted from gravity anomalies due to the accuracy of gravity models (*Becker et al.*, 2009). Improved marine gravity of the Arctic Ocean can be used to predict bathymetry of the Arctic Ocean using the algorithms developed by *Smith and Sandwell* (1994).

There is high demand for developing a high resolution bathymetry map of the oceans. The Seabed 2030, a joint project with GEBCO, is launched in June 2017. It is a joint effort from many countries and institutions around the world, industry and academic research organisations. The aim of the project is to produce a complete, high resolution bathymetry map of the oceans by the year 2030 (*Mayer et al.*, 2018).

1.3 Research objectives

This thesis aims to improve marine gravity field from recent satellite altimetry, particularly over the coastal areas by revising the altimetric gravity prediction methods. To apply the FFT method for gravity modelling, data has to be gridded into a regular grid. This is not optimal near the coastal regions where data gaps exist. Moreover, FFT method doesn't provide error estimates of the predicted gravity field. Although, the practical application of LSC is limited by its theoretical assumptions (isotropy and homogeneity) and intensive computational time, it is reasonable to use LSC on the irregularly placed observations without gridding, which is necessary for FFT methods. More importantly, LSC gives the error estimates of the predicted gravity anomalies, which verify the quality of the predicted gravity field. RTM has been successfully used over land in many studies, but has not been considered over the ocean for global gravity field modelling. In this study, RTM effects near the coastal zone will be considered in the modelling process. CyoSat-2 SAR waveforms retracked from different retrackers will be used to investigate the effect

of retrackers in marine gravity modelling.

Gravity field is expected to be improved by revising altimetry data processing methods. More detailed topographic features may be resolved by sea floor topography predicted from improved marine gravity. The secondary goal of this thesis is to develop methods to predict bathymetry from gravity. The methods will be used for Arctic bathymetry prediction.

1.4 Thesis outline

The thesis is divided into two parts. The first part is about improving marine gravity from satellite altimetry with main focus on the coastal zones. Introductions to the gravity potential, satellite altimetry, remove-compute-restore technique, residual terrain modelling and LSC algorithm are described in Chapter 2. A brief introduction to the satellites, data archives distributing retracked altimetry products, various datasets to be used in the marine gravity modelling process are described in Chapter 3. Two case studies of coastal marine gravity modelling are presented in Chapter 4.

The second part is about bathymetry prediction from marine gravity anomalies focusing on the Arctic Ocean. An introduction to bathymetry mapping along with gravity and topography relationship is given in Chapter 5. Data sources to be used for the Arctic Ocean bathymetry prediction are introduced in Chapter 6. Arctic bathymetry prediction results and validations are presented in Chapter 7. Finally, Chapter 8 provides a summary on the results, as well as an outlook on the future work.

Part I

Marine gravity modelling

Chapter 2

Background theory in marine gravity modelling

This chapter includes brief introductions to the concepts in gravity, geoid heights, satellite altimetry and observations, the methodology of marine gravity modelling.

2.1 Definitions

This section includes the definition of the gravity potential of the Earth, the geoid and height systems, along with gravity and height anomalies.

2.1.1 The gravity potential and geoid

The gravitational potential V_P at a point P outside the earth can be expressed as the integral over the earth's mass distribution, following Newton's law of gravitation

(*Heiskanen and Moritz*, 1967; *Moritz*, 1980; *Sansò and Sideris*, 2013)

$$V_P = G \iiint_{earth} \frac{\rho_Q}{r_{PQ}} d_{V_Q}, \tag{2.1}$$

where point Q is a point variable within the Earth's body, ρ_Q is the density of the infinitely small volume element d_{V_Q}, r_{PQ} being the distance between point P and Q. In a spherical coordinate system, the coordinates are defined by geocentric distance r, longitude λ, and co-latitude θ ($\theta = 90^\circ - \phi$, ϕ is the geocentric latitude), then $d_{V_Q} = r_Q^2 \sin\theta dr d\theta d\lambda$, G is the Newtonian gravitational constant

$$G = 6.672 \times 10^{-11}\ \mathrm{m^3 s^{-2} kg^{-1}}. \tag{2.2}$$

The integral excludes the effect of atmosphere and temporal variations of potential, which are very small and have corrections with a relative order of 10^{-6} and 10^{-7} (*Moritz*, 1980). Therefore, the density term only corresponds to the solid and liquid parts of the Earth's body.

In an earth-fixed rotating coordinate system, the gravity potential W on a point P with coordinates (x,y,z) is the sum of the gravitational potential V and the potential of the centrifugal force V_c

$$\begin{aligned} W(x,y,z) &= V(x,y,z) + V_c(x,y) \\ V_c(x,y) &= \frac{1}{2}\omega^2(x^2+y^2), \end{aligned} \tag{2.3}$$

where ω is the angular velocity of Earth.

The gradient (i.e., first order derivatives) of the potential W is defined as the

gravity vector and its magnitude is called the *gravity*

$$\begin{aligned} \vec{g} &= \nabla W = \left[W_x,\ W_y,\ W_z \right]^T \\ g &= |\nabla W|, \end{aligned} \tag{2.4}$$

where the ∇ is the first order derivative operator.

The surfaces, on which the gravity potential $W(x,y,z)$ is constant are called equipotential surfaces. The gravity vector $\vec{g}$ on a point $Q(x,y,z)$ is orthogonal to the equipotential surface passing through point Q (*Hofmann-Wellenhof and Moritz*, 2006). The particular equipotential surface (denoted as W_0 in Figure 2.1) that approximately fits with an average surface of the oceans is called the *geoid*. Further, the gravity field of the (reference) ellipsoid is defined as the normal gravity potential $U(x,y,z)$ which exactly corresponds to the geoid (W_0). Thus, the ellipsoid is an equipotential surface that can be mathematically formulated. For the detailed form of mathematical expressions, see *Hofmann-Wellenhof and Moritz* (2006). In general, the normal gravity potential $U(x,y,z)$ can be written as,

$$U(x,y,z) = V^{ell}(x,y,z) \ + \ \frac{1}{2}\omega^2(x^2+y^2), \tag{2.5}$$

where V^{ell} is the gravitational potential of the ellipsoid. The potential function (2.5) is completely determined by the shape of the ellipsoid (semiaxes a and b), total mass M and the angular velocity ω. Meanwhile, by the definition of the reference ellipsoid, the geocenter of the ellipsoid coincides with the center of mass of the Earth. The gradient of normal potential gives normal gravity γ

$$\begin{aligned} \vec{\gamma} &= \nabla U = \left[U_x,\ U_y,\ U_z \right]^T, \\ \gamma &= |\nabla U|. \end{aligned} \tag{2.6}$$

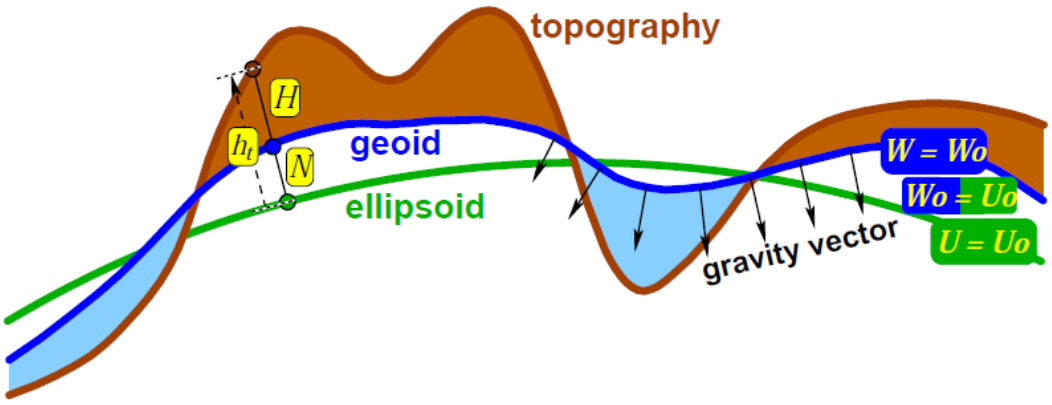

Figure 2.1: The illustration of surface topography, geoid and reference ellipsoid (*Barthelmes*, 2013)

In spherical approximation, the normal gravity is

$$\gamma_o = \frac{GM}{R^2}, \tag{2.7}$$

where $R(=6371\ \text{km})$ is the mean radius of Earth. The approximated spherical Earth has the same volume and total mass M as the Earth ellipsoid.

As for the second order derivatives of the gravitational potential V, the trace of matrix $\nabla(\nabla V)$ is the Laplacian of V

$$\triangle V = V_{xx} + V_{yy} + V_{zz} = \frac{\partial^2 V}{\partial x^2} + \frac{\partial^2 V}{\partial y^2} + \frac{\partial^2 V}{\partial z^2}. \tag{2.8}$$

The symbol $\triangle$ denotes the *Laplacian operator*, and outside the attracting masses (e.g., above the Earth surface), V satisfies the *Laplace's equation*

$$\triangle V = 0. \tag{2.9}$$

The *Laplace's equation* is very important in physical geodesy. The solution of the Laplace's equation (2.9) gives the potential of gravitation and called *harmonic*

functions (*Hofmann-Wellenhof and Moritz*, 2006; *Moritz*, 1980). In other words, the potential outside the Earth surface can be expressed in the form of harmonic functions.

2.1.2 The anomalous potential

The advantage of defining the normal gravity potential $U(x,y,z)$ is that the true potential W can now be split into two parts, one well formulated normal potential U and one remaining potential, denoted as anomalous potential T,

$$W(x,y,z) = U(x,y,z) + T(x,y,z). \tag{2.10}$$

By reformulating and taking in the gravitational potential V of the Earth and the gravitational potential V^{ell} of the reference ellipsoid,

$$T(x,y,z) = V(x,y,z) - V^{ell}(x,y,z). \tag{2.11}$$

Since the gravitational potentials are harmonic and satisfies the Laplace's equation, the anomalous potential T also satisfies the Laplace's equation (2.9).

The anomalous potential is a very important functional in physical geodesy and is a bridge connecting the "measured" quantities, like the gravity anomaly and height anomalies to be described in the following sections.

2.1.3 Height anomaly and gravity anomaly

2.1.3.1 Height anomaly

The *geoidal height* or *geoid undulation* (N) is the height of the geoid above the reference ellipsoid. It is the vertical distance between a point on the geoid and the reference ellipsoid. The ellipsoid height (h_t) is the vertical distance between a point on the surface topography and ellipsoid. The orthometric height (H^{orth}) is the height of a point above the geoid, which is measured along the plumb line (i.e., the direction of gravity vector Eq.(2.4)). Since the equipotential surfaces are not parallel, the plumb line segments are slightly curved. However, with sufficient approximations, these quantities (also see Figure 2.1 and 2.2a) are related by

$$h_t = H^{orth} + N. \tag{2.12}$$

To compute the orthometric heights H^{orth} from levelling, the mean gravity $\bar{g}$ along the plumb line is needed. However, the gravity inside the earth can not be measured. For the computation of mean gravity, the density of the masses above the geoid should be well known. To avoid the assumptions of mass densities and mass distribution outside geoid, Molodensky proposed an approach that replaces the geoidal heights.

The ellipsoidal height h_t is now determined by the normal height H^* and height anomaly ζ,

$$h_t = H^* + \zeta. \tag{2.13}$$

The height anomaly ζ is the vertical distance between point P on the Earth's surface and *telluroid*, which is defined as a surface passing through a point Q where

the normal potential U_Q equals the actual potential W of corresponding point P, i.e., $W_P = U_Q$.

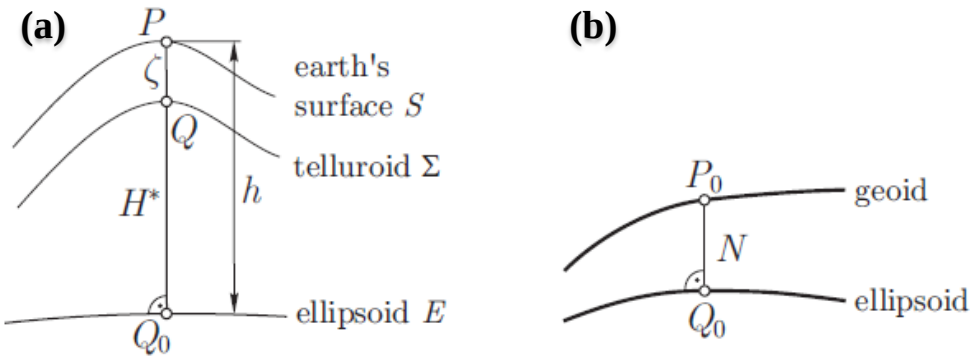

Figure 2.2: (**a**) The illustration of height anomaly ζ and normal height H^* along with the ellipsoidal height h_t, (**b**) geoid height N (*Hofmann-Wellenhof and Moritz*, 2006)

.

By the famous Brun's formula, the geoidal height N and the Molodensky height anomaly ζ is related to the anomalous potential T,

$$N = \frac{T(P_o)}{\gamma}, \tag{2.14}$$

$$\zeta = \frac{T(P)}{\gamma}, \tag{2.15}$$

where $T(*) = W_* - U_*$ is the anomalous potential at different boundary surfaces, P_o is on the geoid and P is on the Earth's surface, γ is normal gravity evaluated at ellipsoidal point Q_o in Figure 2.2.

The geoid height N_{P_o} can be converted to height anomaly ζ_P using spherical approximation and neglecting omission errors. The difference is given by,

$$N_{P_o} - \zeta_P \approx -\frac{2\pi G\rho}{\gamma}(H_P^{ortho})^2, \tag{2.16}$$

where H_P^{ortho} is the orthometric height of point P.

On the sea level, the geoid coincides with the sea surface. The observed sea surface heights (ellipsoidal height) are approximately the heights of the geoid which make the $H_P^{ortho} = 0$. Therefore, on the sea level, $N = \zeta$. In other words, we don't differentiate the height anomaly and geoid undulation when working with marine gravity modelling.

Since the measurements are conducted on the surface of the earth, the height anomaly is a more practical term in geoid determination and gravity field modelling.

2.1.3.2 Gravity anomaly

The *conventional* gravity anomaly δg_c is defined on the geoid, and it is the difference between the norms of the gravity vector $\vec{g}$ at point P_o using Eq.(2.4) and normal gravity vector $\vec{\gamma}$ at point Q_o using Eq.(2.6). The locations of point P_o and Q_o are as in Figure 2.2b. The gravity measurements on the topography have to be reduced to the geoid level before the conventional gravity anomaly is computed.

$$\triangle g_c \;=\; g_{(P_o)} \;-\; \gamma_{(Q_o)}. \tag{2.17}$$

The *free-air* garvity anomaly is defined on the ground level, using direct gravity measurements on the earth's surface at point P and normal gravity at point Q on the telluroid (Figure 2.2a).

$$\triangle g \;=\; g_{(P)} \;-\; \gamma_{(Q)}. \tag{2.18}$$

On the sea level, since the geoid fits with the mean ocean surfaces, the conventional and free-air anomalies are almost identical and we don't differentiate the

terms.

Further, the free-air gravity anomaly is related to the anomalous potential T,

$$\triangle g = -\frac{\partial T}{\partial r} + \frac{1}{\gamma}\frac{\partial \gamma}{\partial r}T. \tag{2.19}$$

The Eq.(2.19) is also called the *fundamental equation of physical geodesy*. The anomalous potential T can be solved when the gravity anomalies $\triangle g$ are given. In the spherical approximation (where the mean Earth radius is $R = 6371$ km), the equation will be further reduced to

$$\triangle g = -\frac{\partial T}{\partial r} - \frac{2}{R}T. \tag{2.20}$$

Since the development of Global Positioning System (GPS), the ellipsoidal heights can be directly measured, thus the normal gravity at the ground level can be directly computed. The gradient of anomalous potential T yields the gravity disturbance vector δg and it is the difference in the norms of gravity vector $\vec{g}$ and normal gravity vector $\vec{\gamma}$ at the same point P on the Earth's surface

$$\delta g = g_P - \gamma_P = -\frac{\partial T}{\partial r}. \tag{2.21}$$

The gravity disturbance δg is becoming practically more important than the gravity anomalies as the GPS measurements/levelling are replacing the traditional levelling.

2.1.4 Spherical harmonics

The gravitational potential V at a point P, with coordinates (r,θ,λ) defined in the spherical coordinate system, outside the Earth's surface can be expressed in the form of spherical harmonics as below:

$$V(r,\theta,\lambda) = \frac{GM}{R}\sum_{n=0}^{\infty}\left(\frac{R}{r}\right)^{n+1}\sum_{m=0}^{n}\bar{P}_{nm}(\cos\theta)\left(\bar{C}_{nm}\cos m\lambda + \bar{S}_{nm}\sin m\lambda\right), \quad (2.22)$$

where G is the Newtonian gravitational constant, M is the total mass of the Earth, R is the mean radius of the earth ($R = 6371$ km in the spherical approximation), the subscript n is called *degree*, which has integer values from $0,1,\ldots,\infty$, m is called *order*, which takes integers from 0 to n, $\bar{C}_{nm}, \bar{S}_{nm}$ are the fully normalized spherical harmonic coefficients, $\bar{P}_{nm}$ are the fully normalized Legendre functions.

Since the first term $\bar{C}_{00}$ is close to 1, the degree $n = 1$ spherical harmonic coefficients $\bar{C}_{10}, \bar{S}_{10}, \bar{C}_{11}, \bar{S}_{11}$ are zero when the coordinate systems' origin is defined at the geocenter (center of mass), the formulation (2.22) can be further simplified as

$$V(r,\theta,\lambda) = \frac{GM}{r}\left[1 + \sum_{n=2}^{\infty}\left(\frac{R}{r}\right)^{n}\sum_{m=0}^{n}\bar{P}_{nm}(\cos\theta)(\bar{C}_{nm}\cos m\lambda + \bar{S}_{nm}\sin m\lambda)\right]. \quad (2.23)$$

The gravitational potential of the ellipsoid V^{ell} can also be expanded into spherical harmonics with coefficients $(\bar{C}^{ell}_{nm}, \bar{S}^{ell}_{nm})$. Due to the rotational and equatorial symmetric properties of ellipsoid, the coefficients only contain the zero order terms and even-degree terms. This implies $\bar{S}^{ell}_{nm} = 0$.

Recall the definition of anomalous potential T (2.11). Since the gravitational potentials are expanded into spherical harmonics as in Eq.(2.22), the anomalous

potential T can also be represented in the form of spherical harmonics

$$T(r,\theta,\lambda) = \frac{GM}{R}\sum_{n=0}^{\infty}\left(\frac{R}{r}\right)^{n+1}\sum_{m=0}^{n}\bar{P}_{nm}(\cos\theta)(\bar{C}^{T}_{nm}\cos m\lambda + \bar{S}^{T}_{nm}\sin m\lambda), \quad (2.24)$$

where $\bar{C}^{T}_{nm}$ and $\bar{S}^{T}_{nm}$ are the spherical harmonic coefficients specific for the anomalous potential T. In practice, the coefficients $\bar{S}^{T}_{nm} = \bar{S}_{nm}$, while the $\bar{C}^{T}_{nm}$ are achieved by subtracting the low-degree zero order coefficients $(\bar{C}^{ell}_{20}, \bar{C}^{ell}_{40}, \bar{C}^{ell}_{60}, \bar{C}^{ell}_{80})$ of the ellipsoidal normal potential, i.e.,

$$\begin{aligned} \bar{C}^{T}_{nm} &= \bar{C}_{nm} - \bar{C}^{ell}_{nm} \\ \bar{S}^{T}_{nm} &= \bar{S}_{nm}. \end{aligned} \quad (2.25)$$

Legendre's functions: The general formulation of Legendre function $P_{nm}(t)$, where $t = \cos\theta$ is

$$P_{nm}(t) = \frac{1}{2^n n!}\left(1-t^2\right)^{m/2}\frac{d^{n+m}}{dt^{n+m}}(t^2-1)^n. \quad (2.26)$$

Particularly, when the order $m = 0$, the Legendre functions are called the *Legendre polynomials*.

$$P_n(t) = P_{n0}(t) = \frac{1}{2^n n!}\frac{d^n}{dt^n}(t^2-1)^n. \quad (2.27)$$

In practice, the polynomials may be obtained by the recursion formula as following, which will be computationally efficient

$$P_n(t) = -\frac{n-1}{n}P_{n-2}(t) + \frac{2n-1}{n}tP_{n-1}(t). \quad (2.28)$$

The non-zero order terms of the Legendre functions are called the *associated Legendre functions* and the general Legendre functions (2.26) can be further simplified

by the Legendre polynomials to

$$P_{nm}(t) = \left(1 - t^2\right)^{m/2} \frac{d^m}{dt^m} P_n(t). \tag{2.29}$$

Finally, the fully normalized Legendre polynomials are given by

$$\begin{aligned} \bar{P}_{nm}(t) &= \sqrt{k(2n+1)\frac{(n-m)!}{(n+m)!}} P_{nm}(t), \\ \text{with } k &= \begin{cases} 1 & \text{for} \quad m = 0 \\ 2 & \text{for} \quad m \neq 0. \end{cases} \end{aligned} \tag{2.30}$$

Gravity field functionals expanded in spherical harmonics: As seen in the definition of height anomaly (2.15), gravity anomaly (2.20) and gravity disturbance (2.21), the three quantities can also be expanded into spherical harmonics by using (2.24):

$$N(r,\theta,\lambda) = \frac{GM}{R} \sum_{n=0}^{\infty} \frac{1}{\gamma} \left(\frac{R}{r}\right)^{n+1} \sum_{m=0}^{n} \bar{P}_{nm}(\cos\theta)(\bar{C}^T_{nm} \cos m\lambda + \bar{S}^T_{nm} \sin m\lambda), \tag{2.31}$$

$$\triangle g(r,\theta,\lambda) = \frac{GM}{R} \sum_{n=0}^{\infty} \frac{n-1}{r} \left(\frac{R}{r}\right)^{n+1} \sum_{m=0}^{n} \bar{P}_{nm}(\cos\theta)(\bar{C}^T_{nm} \cos m\lambda + \bar{S}^T_{nm} \sin m\lambda), \tag{2.32}$$

$$\delta g(r,\theta,\lambda) = \frac{GM}{R} \sum_{n=0}^{\infty} \frac{n+1}{r} \left(\frac{R}{r}\right)^{n+1} \sum_{m=0}^{n} \bar{P}_{nm}(\cos\theta)(\bar{C}^T_{nm} \cos m\lambda + \bar{S}^T_{nm} \sin m\lambda). \tag{2.33}$$

Last but not least, the process of achieving the gravity functionals from the available spherical harmonic coefficients is called *spherical harmonic synthesis*, whereas deriving the spherical harmonic coefficients from global observations by solving large system equations is called *spherical harmonic analysis*.

2.2 Satellite altimetry

Satellite altimetry has been a key technique in modelling earth's gravity, studying ocean dynamics and sea level monitoring. Moreover, the satellite altimetry missions have proven to be efficient in monitoring lakes, continental ice and sea ice, rivers and so on. In this section, we will briefly introduce the principles of radar altimetry and how the sea surface heights (SSH) are derived.

2.2.1 Radar altimeter principles

The on-board radar altimeter is the key instrument in a radar altimetry satellite. In the case of nadir-looking altimeters, the radar altimeter transmits pulsed echoes from a satellite to the earth's surface with a high Pulse Repetition Frequency (PRF) and later receives the return echoes. By precisely recording the travel time between the transmitted and received echoes, the distance between the satellite and the satellite nadir surface, also called the *range*, can be estimated. The *altitude* of the satellite (H^{Sat}) can be precisely determined by GPS and/or Doppler Orbitography and Radiopositioning Integrated by Satellite (DORIS). Then the surface heights above the reference ellipsoid can be determined as follows:

$$SSH = H^{Sat} - range - r_{RRC} - r_{geo}, \tag{2.34}$$

where the term r_{geo} refers to all the *geophysical corrections* (see Table 2.1) and r_{RRC} refers to *retracking range correction* to be introduced later.

The SSH comprises the *geoid*, which is described in Section 2.1.1, *the dynamic topography*, which represents the permanent stationary components (permanent ocean circulation linked to Earth's rotation, permanent winds, etc.) and *a highly*

Table 2.1: List of geophysical corrections included in the range correction term r_{corr}.

Geophysical corrections		Amplitude
Atmospheric corrections	Dry troposphere	1.7 to 2.5 m
	Wet troposphere	0 to 50 cm
	Ionosphere	6 to 12 cm
	Dynamic atmosphere	-15 to 15 cm
Tidal corrections	Ocean loading tide	-2 to +2 cm
	Solid earth tide	-30 to +30 cm
	Geocentric polar tide	-2 to 2 cm
	Ocean tide	-50 to 50 cm
	Long period tide	-2 to 2 cm

variable component (due to wind, eddies, seasonal variations, etc.).

2.2.2 Retrieving precise sea surface heights

It is necessary to apply various geophysical corrections and retracker range correction to achieve precise sea surface heights. In the following, we will briefly address the sources of the corrections in Table 2.1.

2.2.2.1 Atmospheric corrections

The *dry tropospheric correction* accounts for the pulse delay caused by the non-polar gases such as nitrogen and oxygen. The dry tropospheric correction is the largest correction among the geophysical corrections and obtained from meteorological observations (atmospheric pressure and temperature).

The *wet tropospheric correction* compensates for the delay caused mainly by the water vapour content in the earth's atmosphere along the pulse propagation. It is determined by the on-board radiometer at the time of measurements.

The *ionospheric correction* accounts for the delay caused by the free electron con-

tent in the atmosphere. The ionospheric correction can be modelled by the GPS dual frequency measurements.

The dynamic atmospheric correction compensates for the variations in sea surface heights due to the atmospheric pressure and winds and is taken from MOG2D model[1] distributed by Aviso+.

2.2.2.2 Tidal corrections

The *ocean tide correction* removes the effects of the local tides caused by the moon and sun, while the *long period tide correction* removes the tidal effects due to the sun. The *ocean loading tide correction* removes the deformation of the earth's crust caused by the load of ocean tides. The ocean tide, the ocean loading tide and the long period tide corrections are taken from FES2014 model[2] in the recent processing of the altimeter data used in this thesis.

The *solid earth tide correction* removes the deformation of the earth due to the tidal forcing caused by the moon and the sun. It is taken from Cartwright model (*Cartwright and Edden*, 1973; *Cartwright and Tayler*, 1971)

The *geocentric polar tide correction* removes a long-period distortion of the Earth's crust caused by the variation in the Earth's rotation axis, i.e., the change of polar geographic location. It is determined by the polar location files.

[1] Dynamic atmospheric Corrections are produced by CLS using the Mog2D model from LEGOS and distributed by Aviso+, with support from CNES (https://www.aviso.altimetry.fr/)

[2] FES2014 was produced by Noveltis, LEGOS and CLS and distributed by Aviso+, with support from CNES (https://www.aviso.altimetry.fr/)

2.2.2.3 Retracking range correction

The return echo received by the altimeters is recorded in a *range window*, which is typically equivalent to around 60 m range for the conventional pulse-limited altimeters. The window delay parameter refers to the two-way time between pulse emission and the reference point at the center bin of the range window. From the window delay parameter, the *range* in Eq.(2.34) can be estimated. A specific point referring to the measurement of range to the surface is known as retracking point. Retracking range correction r_{RRC} is the offset from the retracking point to the center bin of the range window, see Figure 2.3.

Retracking is performed to find the retracking point on waveform. Several retracking algorithms have been proposed to determine the location of retracking point. Physical retrackers are based on assumptions about the surface type below the satellite and analytical formulation of return echo. The Brown retracker (*Brown*, 1977) and SAMOSA[3] retracker (*Martin-Puig et al.*, 2008; *Ray et al.*, 2015) are the well known physical retrackers developed for the conventional altimeter waveforms and for the novel Synthetic Aperture Radar (SAR) waveforms of CryoSat-2. Empirical retrackers are developed without any assumption of the surface type below the satellite. Offset-center of gravity (OCOG) retracker (*Wingham et al.*, 1986), threshold retracker (*Davis*, 1995, 1997), improved threshold retracker (*Bao et al.*, 2009) and Narrow Primary Peak (NPP) retracker (*Jain et al.*, 2015) are several of the many empirical retrackers. The improved threshold retracker and NPP retracker make use of subwaveforms (Figure 2.3) around the waveform peak value to determine the retracking point.

Physical retrackers likely fail to fit the analytical models to the waveforms especially when the waveforms are contaminated. In addition, fitting analytical models

[3]Synthetic Aperture Radar (SAR) Altimetry Mode studies and Applications

to waveforms is a time-consuming process. Nevertheless, sea surface heights derived from physical retrackers are more accurate and precise than heights derived from empirical retrackers.

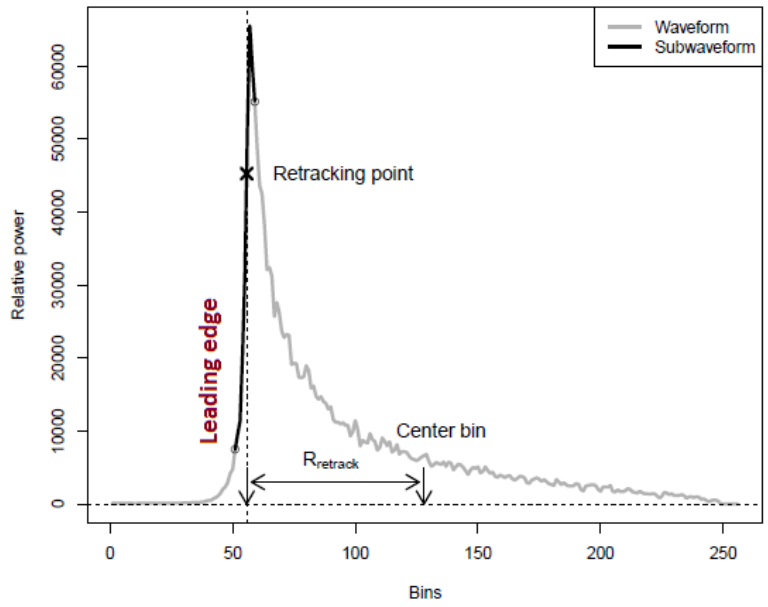

Figure 2.3: CryoSat-2 SAR waveform (in grey) and subwaveform (in black) around the primary peak. The center bin in the range window, retracking point and retracking range correction are illustrated. Adapted from (*Nielsen et al.*, 2017)

2.3 Remove-Compute-Restore technique

As shown by the definitions of gravity functionals in Section 2.1, after the linearisation, the relationship between the gravity anomalies, geoid heights or height anomalies are linear with acceptable omission errors. Hence, one can achieve the other quantity from the measured observations.

The anomalous potential T can also be constructed by the sum of a model T_M

and residual T_r

$$T = T_M + T_r \tag{2.35}$$

where the term T_M can be directly computed by the spherical harmonic synthesis Eq.(2.24) for a maximal degree n_{max}. The model corresponds to the (global) long-wavelength part of the signal, while the residual term refers to the (local) short-wavelength signals.

For marine gravity modelling, the sea surface heights can be written as the sum of model and residual terms,

$$SSH = N^{EGM} + \text{MDT}^{EGM} + N^{RTM} + N_r + \epsilon(t) + e\,, \tag{2.36}$$

where the term N^{EGM} is computed from an Earth Gravitational Model (EGM) evaluated with Eq.(2.31), MDT^{EGM} is the mean dynamic topography associated with the EGM, N^{RTM} is the contribution from topography (see Section 2.4), N_r is the geoid residual (identical to the height anomaly over the ocean), $\epsilon(t)$ is the time dependent components, e is the error term remaining in the data.

After removing as much of we know from the SSHs, the magnitude of the remaining signal N_r (approx. 1 m) is much smaller than the magnitude of geoid (or SSH; approx. 100 m). With such residual field, we obtain a more homogeneous and smooth field than before, which will allow the application of the spherical approximations (*Sansò and Sideris*, 2013).

In physical geodesy, the Remove-Compute-Restore (RCR) technique is widely used in geoid modelling (*Barzaghi et al.*, 2018; *Forsberg*, 1991; *Tscherning and Forsberg*, 1986). In this thesis, we also model the gravity field within the framework of remove-compute-restore methodology. The RCR technique is further discussed by *Omang and Forsberg* (2000); *Schwarz et al.* (1990); *Sjöberg* (2005). In the following, we

describe the gravity modelling from altimetry in the frame of RCR technique.

2.3.1 Remove - SSH signal reduction

In the remove step, the SSH is reduced by removing as much as we know from existing global models. In Eq.(2.36), the EGM geoid height N^{EGM}, dynamic topography MDT^{EGM} can be directly achieved from existing release of EGM, i.e., EGM08 (*Pavlis et al.*, 2012). The spherical harmonic coefficients of the EGM08 is complete up to degree and order 2159, with additional coefficients extending to degree 2190 and order 2159. One can compute the geoid heights up to desired degree and order (d/o), for instance $n = 1080$, using the spherical harmonic synthesis as in Eq.(2.31). The term N^{RTM} accounts for the local features that have the shorter wavelengths than that of N^{EGM} removed earlier. It can be modelled by the Residual Terrain Modelling (RTM) technique to be described later in section 2.4.

The $\epsilon(t)$ in Eq.(2.36) is the time dependent component of sea surface heights, which is mainly caused by wind, waves and dynamic pressure. This term is also denoted as dynamic sea surface topography in other literature (*Sansò and Sideris* (2013), Section 9.4.3). It is crucial to remove/diminish the effect of such dynamic topography as it will result in large along track gravity field errors. The effect of $\epsilon(t)$ can be minimized by performing the cross-over adjustment (*Knudsen and Brovelli*, 1993) as described below.

2.3.1.1 Cross-over adjustment

In satellite altimetry, the intersection point of an ascending track and a descending track is called *the cross-over point*. The geoid is assumed to be stationary and static. Hence, the geoid residuals N_r at a cross-over location should be identical on both

ascending and descending tracks despite the fact that the sea surface is measured at different epochs. The cross-over adjustment is performed to minimise the track related errors by mutually adjusting the tracks.

The detailed algorithm on the cross-over adjustment can be found in *Knudsen and Brovelli* (1993) and in the book Geoid Determination by *Sansò and Sideris* (2013). In this study, the Fortran program CRSADJ included in the GRAVSOFT package is used to diminish the error related to $\epsilon(t)$.

The cross-over adjustment is performed after removing N^{EGM}, MDT^{EGM} and N^{RTM}.

2.3.2 Compute - height anomaly to gravity anomaly

After the signal reduction and cross-over adjustment procedures, we have the "clean" residual height anomalies N_r. In the computation step, the residual gravity field $\triangle g_r$ is modelled from the residual height anomalies N_r. Two techniques can be used to convert the height anomalies to gravity, which are the Fast Fourier Transform (FFT) method (*Forsberg and Sideris*, 1993; *Schwarz et al.*, 1990) and Least Square Collocation (LSC) method (*Bašić and Rapp*, 1992; *Forsberg and Tscherning*, 1981; *Moritz*, 1978).

The advantage of LSC is that it can handle heterogeneous observations and the observations do not have to be gridded as in the case of FFT. Moreover, LSC provides the error estimates of the predicted signal quantity. The disadvantage of LSC is that it requires intensive computational power, as the size of the normal equation increases with the number of observations.

When we focus on the coastal zone, the altimetry tracks terminates near the coastline. Hence, it is an advantage to avoid the gridding of the altimetry data and

proceed with the more sophisticated LSC algorithm in this work (more details in section 2.5).

2.3.3 Restore - full gravity field

In the restore step, we need to add back what we have removed. Specifically, the long wavelength components of gravity anomalies from EGM08 and RTM gravity anomalies ($\triangle g^{EGM}$ and $\triangle g^{RTM}$ in Eq.(2.37)) are added to the predicted gravity anomalies $\triangle g_r$. Thus, the full wavelength marine gravity is obtained by the RCR technique.

$$\triangle g = \triangle g^{EGM} + \triangle g^{RTM} + \triangle g_r. \tag{2.37}$$

Alternative to the evaluation of spherical harmonics, the EGM08 geoid height (N^{EGM}), which is removed in RCR and corresponding EGM08 gravity anomaly ($\triangle g^{EGM}$) restored in RCR can be obtained from ICGEM service (http://icgem.gfz-potsdam.de/home).

2.4 Residual terrain modelling

Th Residual Terrain Modelling (RTM) is a technique to compute the Earth's short-scale gravitational potential from topographic mass models. It is one of the most common mass reduction methods in physical geodesy. In the RTM approach, the topographic masses above the reference surface are removed and fill up the deficits below the reference surface (see Figure 2.4). The RTM method is based on the (constant) mass-density assumptions of the topographic masses. Using a high resolution Digital Elevation Model (DEM), the RTM effects can be computed by numerical integration of mass prisms (alternatively with tesseroids or point-mass approxima-

tion, see *Heck and Seitz* (2007)) within a circular cap of the computation point. The masses outside the integration radius are assumed not to make significant contributions to the computation point due to the fact that the gravitational attraction from the outside masses attenuates as the distance to the computational point increases. Moreover, the residual terrain elevations, namely RTM elevations H^{RTM}, are the result of subtracting a reference elevation surface H^S from original fine resolution DEMs (ellipsoidal heights denoted by h_t) as in Eq.(2.38).

$$H^{RTM} = h_t - H^S \tag{2.38}$$

The RTM elevations are measured with respect to the reference surface, thus, producing a residual terrain model fluctuating around zero. Numerical integration of such a residual field beyond the integration radius mostly cancels out or insignificantly contributes to the gravitational potential at the computation point.

The RTM technique was initially proposed as an alternative to the isostatic reduction of the gravity observations by *Forsberg and Tscherning* (1981). A detailed description of the RTM reductions can be found in *Forsberg* (1984). The RTM technique can be used to retrieve the uncompensated topographic potential as well as its functionals, e.g., geoid height N, gravity anomalies $\triangle g$, gravity disturbances δg and deflection of the verticals, see *Forsberg* (1984); *Forsberg and Tscherning* (1981); *Nagy et al.* (2000, 2002).

In the case of rectangular prisms, *Nagy et al.* (2000) derived the gravitational potential at the calculation point P in the flat earth approximation as

$$V(P) = G\rho \int_v \frac{1}{r} dxdydz = \int_{x_1}^{x_2} \int_{y_1}^{y_2} \int_{z_1}^{z_2} \frac{1}{r} dxdydz, \tag{2.39}$$

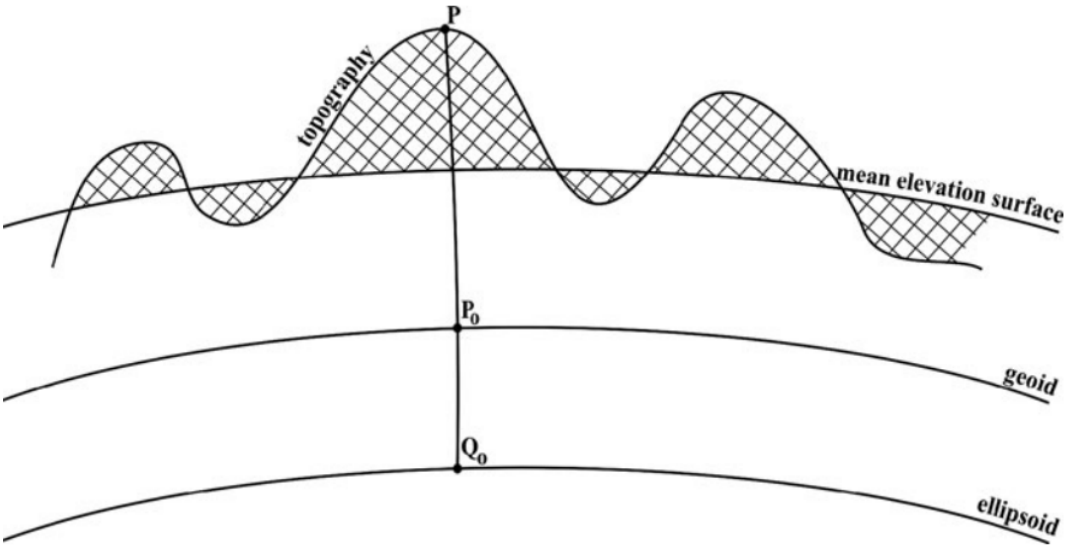

Figure 2.4: The geometry of RTM reduction (*Sansò and Sideris*, 2013)

with r being the distance from the mass element (prisms) to the calculation point P, the limits $(x_1, x_2, y_1, y_2, z_1, z_2)$ indicate the boundaries of the prisms relative to the computation point P. Recall the definition of the gravitational potential in Eq.(2.1). The Eq.(2.39) is the discretization in a local coordinate system centered at the calculation point P. Further, the result of integration is given as,

$$\begin{aligned} V(P) =& G\rho \Big|\Big|\Big| xy \ln(z+r) + yz \ln(x+r) + zx \ln(y+r) \\ & - \frac{x^2}{2}\tan^{-1}\left(\frac{yz}{xr}\right) - \frac{y^2}{2}\tan^{-1}\left(\frac{zx}{yr}\right) - \frac{z^2}{2}\tan^{-1}\left(\frac{xy}{zr}\right)\Big|_{x_1}^{x_2}\Big|_{y_1}^{y_2}\Big|_{z_1}^{z_2}. \end{aligned} \tag{2.40}$$

In practice, the z-axis is assumed to represent the RTM elevations. Therefore, Eq.(2.40) is evaluated with $z_1 = 0$ and $z_2 = H^{RTM}$ (*Hirt*, 2010). Note that this is the gravitational potential generated by a single prism with boundaries $(x_1, x_2, y_1, y_2, z_1, z_2)$. Eq.(2.40) will be evaluated every time with new boundary limits of the next mass prism, until all the mass prisms within the integration radius are assessed. Eventually, the total RTM contribution at the computation point P is

obtained by the summation of the contributions from all prisms.

Heck and Seitz (2007) made a comparison on the calculation speed of the numerical integration with tesseroids, prisms and point-mass approaches and results suggest that the computation time is reduced by a factor of 10 by using the tesseroids instead of prisms, and meanwhile producing more precise potential estimates on the calculation points. Moreover, the tesseroids automatically take into account the earth's curvature while one has to consider the effect of Earth's curvature in the prism approach by a vertical shift of prisms (see *Forsberg* (1984), p.111) or coordinate system transformation (see *Heck and Seitz* (2007), p.125). The point-mass approach is the fastest, but can only be employed when the distance to the calculation point P is large.

The TC program, included in the GRAVSOFT package, is used for the computation of RTM effects throughout the thesis. The numerical prism integration approach was implemented in the program. In practice, the integration radius is set to 200 km at the maximum and planer approximation is assumed. With modern computers, the computation speed is acceptable.

The reference elevation surface in the RTM technique is crucial and represents the mean elevations of the area. Importantly, the resolution of the reference field should match the resolution of the geopotential model, e.g., EGM08, that was removed from the observations. For instance, if the EGM08 geoid height up to d/o 1080, which corresponds to a half-wavelength of 20 km (10 arc minute resolution), is removed from the sea surface heights, the cut-off wavelength of the reference DEM should also be 20 km.

The reference DEM is achieved by spatial moving average filtering or spectral low-pass filtering of the detailed DEMs (*Tocho et al.*, 2012; *Tziavos et al.*, 2009). The TCGRID program included in the GRAVSOFT package is dedicated to produce the

mean elevation grid via spatial moving everage filtering.

Alternatively, *Hirt* (2013) used spherical harmonic reference surface. To avoid the density differences over land and ocean, the rock-equivalent topography (RET, *Balmino et al.* (1973); *Rummel et al.* (1988)) concept was employed. In the RET concept, the ocean water masses are "compressed" into equivalent rock masses. Then, a set of spherical harmonic coefficients of the topography is achieved via *spherical harmonic analysis* of the fine resolution DEM. Subsequent *spherical harmonic synthesis* to the desired degree and order (e.g., $n_{max} = 1080$) will produce the spherical harmonic reference surface, which can be used as the mean elevation surface in the RTM approach.

2.5 Least Square Collocation

In geodesy, Least Square Collocation (LSC) is a technique for determining gravity functionals from the measured quantities. For instance, the gravimetric geoid determination is a problem of deriving geoid heights N from the measured gravity anomalies $\triangle g$, whereas, the other way around, marine gravity modelling is a process of deriving marine gravity anomalies $\triangle g$ from the measured sea surface heights. As shown in Section 2.1.3, the gravity field functionals $(N, \zeta, \triangle g)$ can be expressed as linear functionals of the anomalous potential T. Therefore, the covariance function of the anomalous potential is essential.

In the LSC algorithm, the residual field is assumed to homogeneous and isotropic. The homogeneity assumption refers to the field to be stationary with zero mean. Isotropy refers to the spatial independence of direction.

2.5.1 Gravity field modelling using LSC

As mentioned earlier, the relation between gravity field observables can be expressed through linear functionals L_i as follows,

$$y_i = L_i(T) + e_i \,, \tag{2.41}$$

where y_i is the ith element of the data (gravity anomaly or height anomaly) and e_i is the error in the data.

In the case of modelling gravity anomalies from sea surface height observations, the residual height anomaly N_r is denoted as h for simplicity. Then, the residual gravity anomaly (denoted as Δg for simplicity) can be determined by LSC using the following equation

$$\boldsymbol{\Delta g} = C_{(\Delta g,h)} \left[C_{(h,h)} + D_{(h,h)} \right]^{-1} \boldsymbol{h}, \tag{2.42}$$

where $C_{(\cdot)}$ denotes the covariance function evaluated using equations (2.48), $D_{(\cdot)}$ denotes the noise variance of the "observations" vector $\boldsymbol{h}$, specifically, the residual height anomaly. The advantage of LSC is that the prediction error (variances) can also be estimated via error propagation

$$\sigma^2_{(\Delta g,\Delta g)} = C_{(\Delta g,\Delta g)} - C_{(\Delta g,h)} \left[C_{(h,h)} + D_{(h,h)} \right]^{-1} C^T_{(\Delta g,h)}. \tag{2.43}$$

The size of the variance-covariance matrix $C_{(h,h)}$ dramatically increases with the number of observations taken into the system equation. In the LSC, the process of inverting the variance-covariance matrix $C_{(h,h)}$ is extremely time consuming and require huge computer power.

The covariance function modelling is a crucial step in the LSC. A covariance model is fitted to the empirical covariance estimates (*Knudsen*, 1987) from the observations. There are several covariance models available, e.g., *Duquenne et al.* (2005); *Jordan* (1972); *Kearsley* (1977), but the model proposed by Tscherning and Rapp (*Tscherning and Rapp*, 1974) is sufficient in our modelling. In the following, the empirical covariances estimation procedure and covariance functions to be fitted to empirical covariances will be introduced.

2.5.2 Empirical covariance estimation

Empirical covariances are estimated directly from the residual height anomalies N_r in the study area. Covariances are estimated as a function of spherical distance ψ. Firstly, spherical distance between all data pairs are computed and then, the pairs are grouped according to a predefined interval of $\triangle\psi$. For instance, for a spherical distance of ψ_i, all pairs having spherical distance ψ that satisfy $\psi_i - \triangle\psi/2 \leq \psi \leq \psi_i + \triangle\psi/2$ will be grouped and covariance will be estimated by

$$C(\psi_i) = \frac{1}{M}\sum_{j=1}^{M}[N_r^1 \cdot N_r^2]_j, \tag{2.44}$$

where M denotes the total number of pairs, superscripts 1 and 2 are used to denote the two data points used for computing the spherical distance ψ, the subscript j denote the j'th pair in the group.

The correlation length is defined by the spherical distance where the covariance $C(\psi)$ drops to half of the maximum value obtained at zero spherical distance, $C(0)$. $C(0)$ term also denotes the variance of the dataset.

The empirical covariance estimation procedure described above was implemented in the EMPCOV module.

2.5.3 Covariance functions

For the two points $P(r,\theta,\lambda)$ and $Q(r',\theta',\lambda')$ in the spherical coordinate system, the covariance function $C^{TT}(P,Q)$ is expressed in the form of spherical harmonic expansions

$$\mathrm{Cov}\{T_P,T_Q\} = C^{TT}(P,Q) = \sum_{n=2}^{\infty} k_n \left(\frac{R^2}{rr'}\right)^{n+1} P_n(\cos\psi), \tag{2.45}$$

where $P_n(\cos\psi)$ are Legendre polynomials (2.27), ψ is the spherical distance between the points, which can be computed by

$$\cos\psi = \cos\theta\cos\theta' + \sin\theta\sin\theta'\cos(\lambda-\lambda'). \tag{2.46}$$

The coefficients $k_n = \sigma_n^2$, also called *degree variances*, are achieved from the spherical harmonic coefficients of the anomalous potential $\bar{C}_{nm}^T$ and $\bar{S}_{nm}^T$ (2.24) by sum of squares of order terms as

$$k_n = \sigma_n^2 = \sum_{m=0}^{n} \left[(\bar{C}_{nm}^T)^2 + (\bar{S}_{nm}^T)^2\right]. \tag{2.47}$$

The signal covariances for N and $\triangle g$ can be derived by covariance propagation

$$\mathrm{Cov}\{N_P,N_Q\} = C^{NN}(P,Q) = \sum_{n=2}^{\infty} \left[\frac{1}{\gamma^2}\right] k_n \left(\frac{R^2}{rr'}\right)^{n+1} P_n(\cos\psi) \tag{2.48a}$$

$$\mathrm{Cov}\{\triangle g_P,\triangle g_Q\} = C^{\triangle g\triangle g}(P,Q) = \sum_{n=2}^{\infty} \left[\frac{(n-1)^2}{rr'}\right] k_n \left(\frac{R^2}{rr'}\right)^{n+1} P_n(\cos\psi) \tag{2.48b}$$

$$\mathrm{Cov}\{N_P,\triangle g_Q\} = C^{N\triangle g}(P,Q) = \sum_{n=2}^{\infty} \left[\frac{(n-1)}{\gamma r'}\right] k_n \left(\frac{R^2}{rr'}\right)^{n+1} P_n(\cos\psi) \tag{2.48c}$$

Covariance functions are fitted to the empirical covariance estimated from the (residual) measured quantities in a local region or globally.

In the GRAVSOFT package, the covariance model proposed by *Tscherning and Rapp* (1974) was implemented. The Tscherning&Rapp model is a degree dependent function which has three different forms. The differences stem from how fast the degree-variances goes to zero, like n^{-2},n^{-3}, or n^{-4}. The 2^{nd} type of the degree-variance is of the form

$$\left(\sigma_n^{TR}\right)^2 = \frac{A}{(n-1)(n-2)(n+B)}\left(\frac{R_B^2}{R^2}\right)^{n+1}, n \geq 3 \tag{2.49}$$

where R_B is the radius of Bjerhammer sphere, A is a constant in units of $(\mathrm{m/s})^4$, B is an integer, typically set as 4 for the spherical harmonics of EGM model (*Sansò and Sideris*, 2013).

Then, a complete covariance model as shown in Eq.(2.45) will be given by combination of the degree variances up to n_{max} and Tscherning&Rapp model (for $n > n_{max}$).

$$\begin{aligned}\mathrm{Cov}\{T_P, T_Q\} = \boldsymbol{\alpha} \sum_{n=2}^{n_{max}} \left(\sigma_n^{ERR}\right)^2 \left(\frac{R^2}{rr'}\right)^{n+1} P_n(\cos\psi) \\ + \sum_{n=n_{max}+1}^{\infty} \left(\sigma_n^{TR}\right)^2 \left(\frac{R^2}{rr'}\right)^{n+1} P_n(\cos\psi),\end{aligned} \tag{2.50}$$

where the $\boldsymbol{\alpha}$ is the scaling factor to adjust the analytical covariance model to fit the empirical covariances at low degrees. The *error degree variances* $\left(\sigma_n^{ERR}\right)^2$ are of the form

$$\left(\sigma_n^{ERR}\right)^2 = \left(\frac{GM}{R}\right)^2 \sum_{m=0}^{n} \left[\sigma(\bar{C}_{nm}^T)^2 + \sigma(\bar{S}_{nm}^T)^2\right] \left(\frac{a^2}{R^2}\right)^m, \; 2 \leq n \leq n_{max} \tag{2.51}$$

where $\sigma(\cdot)$ denotes the errors of spherical harmonic coefficients, which are always available upon the official release of the EGM.

In summary, the COVFIT module fits the analytical covariance functions to the empirical covariance estimations from EMPCOV and returns the estimated values

of $(\boldsymbol{\alpha}, R_B, A)$. These parameters will be used in the GEOCOL program to produce variance and co-variance matrix of the gravity functional.

The earlier version of GEOCOL program, e.g., GEOCOL17, was used at the earlier stage of the phd study. The source code can only be compiled by the Intel Fortran compiler (*ifort*[4]), which limited the flexibility of modifying the program. In the latest release of GEOCOL program, the parallel processing option is available in GEOCOL19 (*Kaas et al.*, 2013). In the case study of marine gravity modelling, the GEOCOL19 program is used to speed up the computation.

[4]Visit https://software.intel.com/en-us/fortran-compilers for details.

Chapter 3

Datasets

This chapter includes descriptions of various datasets to be used in case studies in Chapter 4. Specifically, the recent satellite missions that are suitable for marine gravity modelling, are described in Section 3.1. Data archives where the processed altimetry data can be retrived, are introduced in Section 3.2. Digital elevation models that can be used for residual terrain modelling, are briefly described in Section 3.3. Validation datasets that will be used for the case studies are presented in Section 3.4.

3.1 Altimetry data

Various satellite altimetry missions have been operating and planned for the future launches. However, not all the missions are suitable for marine gravity field modelling. In fact, there is not a specific altimetry mission that was designed and launched for the application of modelling marine gravity. For instance, the Topex/-Poseidon, Jason series, ERS-1/2, Envisat, SARAL/Altika and ongoing Sentinal-3 series are initially designed to monitor the oceans, tides or currents and producing

a continuous sea level record overtime. These satellites have short (35 days or less) exact repeat cycles and hence, the across track distance is large. The CryoSat-2, on the other hand, designed to monitor variations in the cryosphere with a repeat cycle of 369 days, which resulted in dense ground tracks of 8 km spacing at equator. This makes the CtyoSat-2 altimetry optimal for marine gravity modelling.

Due to the ageing hardware on-board, fuel economy or mission operations, some of the altimetry missions are operated in the *geodetic mission phase*. For example, Geosat operated in a non-repeat drifting orbit for 18 months (from April 1985 til September 1986), while the ERS-1 operated in a 168-day repeat cycle for 11 months (from April 1994 til March 1995). Envisat operated in a new partly drifting-phase orbit with approx. 30-day repeat cycle since October 2010 til the end of mission in April 2012. In May 2012, after 11 years in orbit, Jason-1 was manoeuvred to a lower orbit with a repeat cycle of 406 days to avoid a potential collision with Topex satellite. Jason-1 failed right after finishing a complete 406-day geodetic phase, which enabled valuable dense across track sampling of the ocean surface. Last but not least, since July 2016, the SARAL/Altika is operating in the SARAL-DP (drifting phase) where no satellite manoeuvres will be conducted unless there is a potential collision. All the *geodetic phase* data from different satellites, in combination with CryoSat-2, are valuable for gravity field modelling (*Andersen et al.*, 2010; *Sandwell et al.*, 2013). In the following, we will briefly introduce the satellite missions (CryoSat-2, Jason-1 and SARAL/Altika) that are used in the thesis for marine gravity modelling.

3.1.1 CryoSat-2

CryoSat-2 was launched by the European Space Agency (ESA) to monitor variations in the cryosphere. Monitoring sea ice thinning in the Arctic and determin-

ing the contributions of continental ice sheets to global sea level rise are the prime objectives of the mission. The satellite orbit is designed to be near-polar with an inclination of 92° so that the cryosphere zone at high latitudes can be covered. The satellite has a 369-day repeat cycle with underlying subcycles of 30 days.

CryoSat-2 is the first radar altimetry satellite with Synthetic Aperture Radar (SAR) and SAR interferometric (SARin) capability with two receiving antennas onboard. The primary payload is the novel Synthetic Aperture Interferometric Radar Altimeter (SIRAL) which is capable of operating in three modes based on a predefined geographical mask (*Wingham et al.*, 2006). In the following, we briefly describe the operating modes of the SIRAL. More information on the CryoSat-2 can be found in the *CryoSat-2 Product Handbook (2014)*.

LRM: the Low Resolution Mode is identical to the conventional pulse-limited altimetry missions like Topex, ERS-1, Envisat, etc. In fact, all the radar altimetry missions launched before Cryosat-2 are in the category of conventional pulse-limited altimetry with large footprints. The LRM mode is operated over the (open) ocean, interior of the ice sheets and most of the land area.

SAR: in the SAR mode, the SIRAL emits bursts of pulses with a much higher PRF than in the LRM. Making use of the delay/Doppler algorithm (*Raney*, 1998) and signal processing techniques on ground, the waveforms retrieved represent a surface area with much smaller along-track width. The transmitted bursts are still pulse-limited. Hence, the SAR altimeter footprints are pulse-limited in the across-track direction, while it is Doppler-limited (beam-limited) in the along-track direction with a resolution of ~ 300 m. The SAR mode is operated over sea ice and coastal areas.

SARin: in the SAR interferometric mode, the other antenna is also activated to receive the return echoes from the surface. When the return echoes are from off-

nadir location, the differences in the travel distance can be measured by the two antennas which translates into interferometric phase, and such the exact arrival angle and location can be determined. The SARin mode is operated at the margins of the ice sheets, e.g., Canadian glaciers, Greenland and Antarctic, as well as several mountainous regions, e.g., the Himalayas, the Alps, the coast of Chile, etc.

3.1.2 Jason-1

Launched in December 2001, Jason-1 is jointly conducted by the French Space Agency (Centre National d'Études Spatiales, CNES) and the United States' National Aeronautics and Space Administration (NASA) for studying the global circulation. Jason-1 was a follow-on mission to the Topex/Poseidon mission. The main goal of the mission is to provide extended continuous time series of highly accurate sea level measurements from which the ocean circulation and its impact on climate change is studied. Jason-1 initially launched to the same orbit as Topex/Poseidon (10-day repeat cycle) with an orbit inclination of 66.04°. From May 2012, Jason-1 is placed on the geodetic orbit with 406-day repeat cycle until the end of life in June 2013. More details about the mission can be found in *Jason-1 Products Handbook (2016)*.

3.1.3 SARAL/Altika

SARAL/Altika (Satellite for ARgos and ALtika) is jointly developed by the French Space Agency (Centre National d'Études Spatiales, CNES) and Indian Space Research Organization (ISRO). SARAL/Altika is designed to use the same orbit as Envisat with an inclination of 98.55° and has a 35-day repeat cycle. The satellite is equipped with the first radar altimeter operating in the Ka-band (35.75 GHz). The

footprints of the Ka-band radar altimeter (5.7 km radius) is much smaller than that of the conventional Ku-band radar altimeters, e.g., 7.7 km radius for CryoSat-2 and 9.6 km for Jason-1.

Since July, 2016, SARAL/Altika is manoeuvred to its drifting phase (SARAL-DP) due to gyro failure and no longer maintain the initial repeat cyle until the end of mission. More details about the mission and configurations can be found in the *SARAL/Altika Product Handbook (2016)*.

Remarks

The key specifications of the above three missions are summarized in Table 3.1.

Table 3.1: Several key mission specifications for the CryoSat-2, Jason-1 and SARAL/Altika. The mission operating period is listed in year and month (YYYY.MM) form. The operating frequency for Ku-band and Ka-band is 13.575 GHz and 35.75 GHz, respectively.

	CryoSat-2	**Jason-1**	**SARAL/Altika**
Mission period	2010.04 -	2001.12 - 2013.06	2013.02 -
Frequency band	Ku-band	Ku-band	Ka-band
Footprint radius	7.7 km	9.6 km	5.7 km
Altitude	717 km	1336 km	800 km
Orbit Inclination	92°	66.04°	98.55°
Initial repeat cycle	369-day	10-day	35-day
Geodetic Mission (GM) specifications			
GM repeat cycle	369-day	406-day	-
Operating period	2010.04 -	2012.05 - 2013.06	2016.07 -

3.2 Data archives

The sea surface height observations can be obtained from several sources. The geophysical corrections (see Table 2.1) are applied by default. In this section, the data archives used to retrieve altimetry data are introduced.

3.2.1 Radar Altimeter Database System

The Radar Altimeter Database System (RADS, http://rads.tudelft.nl/) is a database aimed for harmonised, validated and cross-validated sea level products (*Scharroo et al.*, 2013). The database contains all types of altimetry missions dating from the Geosat mission til the recent Sentinel series. All missions are referenced to the Topex frame by applying the reference frame corrections. For the CryoSat-2 mission, only LRM and SAR mode data is processed. The CryoSat-2 SAR mode acquisitions are processed by a technique called Reduced-SAR (RDSAR) (*Scharroo*, 2016) in the RADS database to achieve seamless transition at the edges of the geographic operations masks[1]. The altimetry waveforms are retracked using the modified Brown retracker (*Brown*, 1977). RADS only provide 1-Hz observations and can be directly used for gravity modelling.

3.2.2 Lars Altimetry Retracking System

The Lars Altimetry Retracking System (LARS[2]) database is developed at DTU Space, where CryoSat-2 waveforms are retracked with 10 different empirical retrackers. The LARS database is specifically developed for CryoSat-2 and has data for all the three operating modes. We choose the the narrow primary peak retracker (*Jain et al.*, 2015) that produces SSHs with the least along track noise (meaning better range precision). LARS database contains 20-Hz data with ground resolution of ∼300 m, which is beneficial for examining leads and sea ice freeboard measurements. For gravity prediction, we use 1-Hz observations which are achieved by simple along track averaging of 20-Hz observations.

[1]The latest CryoSat geographical mask is in place since 30 January 2017 (https://earth.esa.int/web/guest/-/geographical-mode-mask-7107).

[2]Principle manager : Associate professor Lars Stenseng, DTU Space

3.2.3 Grid Processing On Demand

We also retrieve data from ESA's Grid Processing On Demand service (GPOD, https://gpod.eo.esa.int/). The altimetry waveforms are retracked with a physical retracker dedicated for the coastal areas, i.e., SAMOSA+ (*Ray et al.*, 2015) in the GPOD service, whereas the waveforms are retracked with an empirical retracker in LARS database. The GPOD data, therefore, has better height precision (less than 2 cm) than the other two datasets. The GPOD service only provide CryoSat-2 SAR and SARin processing on demand. The sea level products from GPOD provide both 1-Hz and 20-Hz observations. For gravity prediction, we only use 1-Hz observations.

Remarks

Different types of retrackers are used for CryoSat-2 SAR waveforms to apply the retracker range correction in the three data archives. Therefore, the results from gravity modelling may also be different. Nevertheless, the Jason-1 and SARAL/Altika data is only available from RADS and combined with CryoSat-2 data to perform the gravity modelling in the thesis.

So far we have 8 years of CryoSat-2 data available, but using all the altimetry observations yields large covariance matrix, which is hard to invert in the LSC algorithm. Data down-sampling (or thinning through block median averages) is an option, but the behaviour of empirical covariances also changes before and after down-sampling. The precision of observations from different satellite missions are slightly different. For instance, Jason-1 has a large footprint and 6∼7 cm range precision (*Garcia et al.*, 2014), while the Ka-band SARAL/Altika has 3∼4 cm range precision (*Zhang and Sandwell*, 2017), which is equally good as the CryoSat-2 SAR

mode observations. Jason-1 has a 66° orbit inclination while the other two satellite have near polar orbits. The inclusion of Jason-1 data is important as it provides more inter-satellite cross-over points in a small region, which is beneficial for the cross-over adjustment.

3.3 Digital elevation models

3.3.1 SRTM30_PLUS DEM

The Shuttle Radar Topography Mission (SRTM) collected data within latitudes 60°N and 56°S, thus covering approximately 80% of the total land area of the Earth with elevation data of high and fairly uniform accuracy between February 11 and 22 (approximately 11 days) in 2000 (*Farr et al.*, 2007; *Werner*, 2001).

The SRTM30_PLUS global topography grid (version 5.0) is developed by *Becker et al.* (2009). This 30 arc-second grid is basically equivalent to a 1-minute resolution grid (version 11.1) that was produced using the same new soundings and gravity field (version 16) (*Sandwell and Smith*, 2009).

Land data are based on 1-km averages of topography derived from the SRTM version 2.0 released by NASA. GTOPO30 data are used for high latitudes where SRTM data are not available. For the Antarctic, ICESat derived topography is used.

Ocean data are based on the Smith and Sandwell global 1-minute grid between latitudes ±80.5°. Higher resolution grids have been added from the LDEO Ridge Multibeam Synthesis Project[3], the JAMSTEC Data Site for Research Cruises[4], etc. See *Becker et al.* (2009) Table 1 for more details. Arctic bathymetry is from the In-

[3] https://www.ldeo.columbia.edu/research/marine-geology-geophysics/ridge-multibeam-bathymetry-synthesis

[4] http://www.godac.jamstec.go.jp/darwin/e/

ternational Bathymetric Chart of the Oceans (IBCAO, Version 2.0, *Jakobsson et al.* (2008)).

In November 2014, the SRTM30_PLUS topography version 11.0 is released. On the ocean, the bathymetry is inverted from Sandwell global gravity anomalies version 23 (V23.1; *Sandwell et al.* (2014)). In addition, more multi beam and single beam ship soundings are included in the recent release.

3.3.2 GEBCO_2014

General Bathymetric Chart of the Oceans (GEBCO) is a compilation of global and regional bathymetric models with land topography from digital elevation models. In December 2014, the 30 arc-second GEBCO_2014 grid is released. GEBCO_2014 uses the SRTM30_PLUS version 5.0 grid as its base grid. The source of ship soundings and other regional data sets are listed in Table 1 of *Weatherall et al.* (2015).

3.3.3 EMODnet DTM

The European Marine Observation and Data network (EMODnet) is aimed to provide a harmonised digital terrain model for the European sea regions. The EMODnet bathymetry (`http://www.emodnet-bathymetry.eu`) portal is operated and developed by European partnership. The EMODnet DTM is generated from selected bathymetric surveys, satellite derived bathymetry products (*Sandwell and Smith*, 2009; *Sandwell et al.*, 2014) and the data gaps are filled by GEBCO digital bathymetry. In October 2016, the 1/8 arc-minute resolution grids were released. The latest version was released in September 2018 with 1/16 arc-minute resolution and available to users upon request.

3.4 Shipborne and airborne gravity measurements

The marine gravity signal that can be resolved by the altimetry is limited to 12 to 40 km wavelength band (*Garcia et al.*, 2014; *Sandwell et al.*, 2014). By incorporating more altimetry data through the years and optimizing retracker strategy, the shorter wavelength features may also be resolved by altimetric gravity anomalies. Shipborne and airborne gravimetry, in principle, captures the short to medium wavelength features of the gravity and is a valuable source to cross (external) validate the predicted gravity from altimetry. In this section, we briefly introduce the shipborne marine gravity data and airborne data to be used in the case studies in the next chapter.

3.4.1 Shipborne gravimetry

A compilation of cleaned-up gravity database of the Mediterranean was made available for the development of high resolution gravimetric geoid of the Mediterranean (GEOMED2, *Barzaghi et al.* (2018)). The marine data was validated and preprocessed by *Lequentrec-Lalancette et al.* (2016). Two main marine gravity data sets were used in the GEOMED2 project. One of the datasets was obtained from the Bureau Gravimétrique International (BGI) and Service Hydrographique et Océanographique de la Marine (SHOM) data database. The other one was from the Morelli cruises (*Allan and Morelli*, 1971), and the University of Cambridge cruises in the eastern basin. The more recent data available at BGI (SHOM survey data) have a mean error of 2 mGal, determined through cross over adjustment, whereas the "old" Morelli data have a mean error of 3.6 mGal. The marine cruises covering the Mediterranean are shown in Figure 3.1.

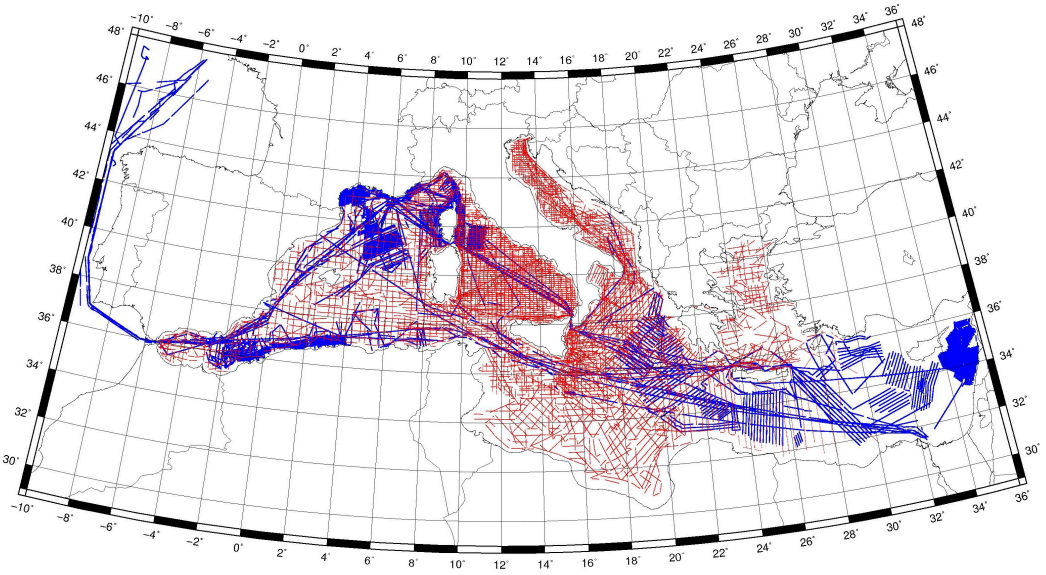

Figure 3.1: The shipborne marine gravity survey from the Morelli data (red) and BGI database (blue). Courtesy of GEOMED2 team.

3.4.2 Airborne gravity survey

Airborne gravimetry is an efficient technique in modelling seamless gravimetric geoid near the coastal zones. DTU has conducted several airborne gravity campaigns in the Southeast Asian countries (Malaysia, Indonesia and Philippines as shown in Figure 3.2), upon request, aiming to establish a unified height reference system. The gravimeter is carried on a fixed-wing aircraft and has an accuracy better than 2 mGal at 5 km resolution (*Olesen and Forsberg*, 2007). The surveys date back to 2002 in East Malaysia (*Jamil et al.*, 2017). Between 2008 and 2011, the Sulawesi, the Borneo and the Papua islands of the Indonesia are mapped respectively. In 2014, an airborne survey was conducted around the Philippines to achieve the geoid model of Philippines (PGM2014) (*Gatchalian et al.*, 2016).

The airborne gravity measurements have high accuracy and resolution. The campaigns in Philippines are also funded by National Geospatial-Intelligence

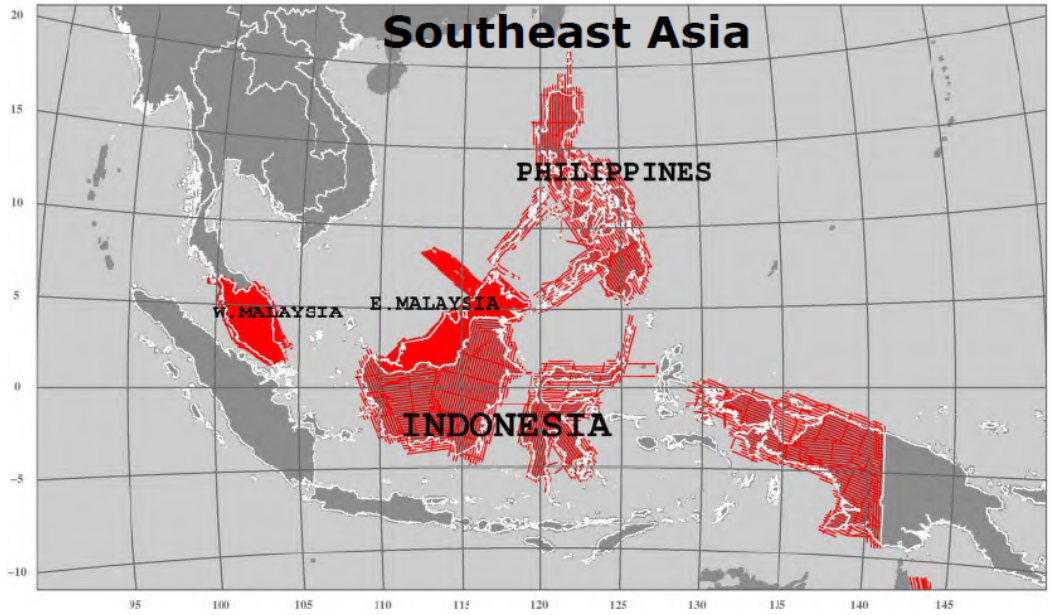

Figure 3.2: The airborne surveys conducted in the Southeast Asia. Courtesy of Rene Forsberg and Arne Olesen

Agency (NGA) of the United States, hence, the data is classified. Data collected after 2008 may be incorporated to the next generation of EGM (EGM2020). We do not have access to all the airborne survey data. In the thesis, only several airborne surveys in the Sulawesi campaign will be used to validate the gravity anomalies predicted from altimetry.

Chapter 4

Coastal marine gravity from altimetry

In the development of DTU gravity models, the altimetry data is processed in small patches of dimensions around 130×300 km ($\triangle\varphi = 1.2^\circ$ in the latitude direction with adaptive $\triangle\lambda$ in the longitude direction). The patches have overlapping boundaries so to have seamless tuning to achieve the final model. The DTU gravity anomalies are predicted from height anomalies using the FFT method which is fast and efficient tool to complete the gravity model of the earth in less than one day. The data in the patches has to be gridded before applying the FFT approach. In the open oceans, the results from FFT approach are nearly identical to the results from the LSC.

We focus on the coastal zones for several reasons. Firstly, the land topography near the coastal zone could contaminate the return waveforms, which decreases altimetry precision. Secondly, if the land/islands are present in the small patches, the gridding procedure used in the FFT approach artificially fills up the data gaps.

Particularly, the gaps between the altimetry points and the coast are also filled, which will degrade gravity prediction near the shore lines. The LSC approach is an alternative to avoid the gridding. Moreover, the LSC algorithm gives the error estimates of the predicted signal quantity. Last but not least, the RTM effects over the ocean were not considered in the global gravity modelling. In the development of EGM08, the RTM effects are computed mainly on land with only 10 km extension towards the sea (*Pavlis et al.*, 2012).

The high frequency contribution of the topographic and bathymetric effects to gravity-field related quantities (e.g., gravity anomalies, geoid heights and deflection of the verticals) is primarily due to the strong correlation of the short-wavelength gravity features with topography and bathymetry. The RTM contributions can also be computed over the oceans to reduce the height anomalies, but it may depend on the resolution of the bathymetry model used in the computation. On land, 3 arc-second ($\sim$ 1 km) resolution SRTM topography is available. However, over the ocean, the resolution of the bathymetry depends on how much of the good quality ship sounding data is integrated to the development of the bathymetry models. The density of sounding surveys varies from region to region. In the case of SRTM30_PLUS global topography, only 6.5% of the grid nodes (between latitude $\pm 80^{\circ}$) are constrained by the soundings (*Becker et al.*, 2009).

This chapter includes two case studies on the coastal marine gravity modelling 1) in the Mediterranean sea north of Sicily island, and 2) in the Gulf of Tomini near the Sulawesi island of Indonesia. The study areas are selected empirically by visual inspection of the global bathymetry maps where significant topography (bathymetry) variations are observed. Most importantly, we have either shipborne or airborne gravity measurements available for external validation in the study regions. The altimetry processing strategy is the same as the production of DTU mod-

els, whereas the RTM effects are taken into account and the LSC algorithm is used instead of the FFT approach.

4.1 Case study: Mediterranean sea

4.1.1 Introduction

In the first year of the phd. study, the author contributed to the GEOMED2 project (*Barzaghi et al.*, 2018). The tasks include the independent validation of the shipborne marine gravity measurements distributed for the project using altimetry. For this study, we choose a region which has a good coverage of ship tracks in the coastal zone and significant bathymetry bathymetry (topography) variations.

We selected the area north of Sicily with geodetic boundaries $13.5^\circ < \lambda < 16.2^\circ$ and $38^\circ < \varphi < 40.2^\circ$. The Aeolian Islands in the Tyrrhenian Sea are located in the center of test area which is bounded by the Italian Peninsula on the east. Various seamounts are observed (from GoogleEarth) in the study area, among which the Pliny seamount, marked by orange filled circle in Figure 4.1b, is the tallest ($\sim$ 2.4 km). The CryoSat-2 operates in the SAR mode in the study area. The area spans more than 200 km in both latitude and longitude direction, which is sufficiently larger than the maximum half-wavelength (approx. 10 km) the EGM08 (d/o 2190).

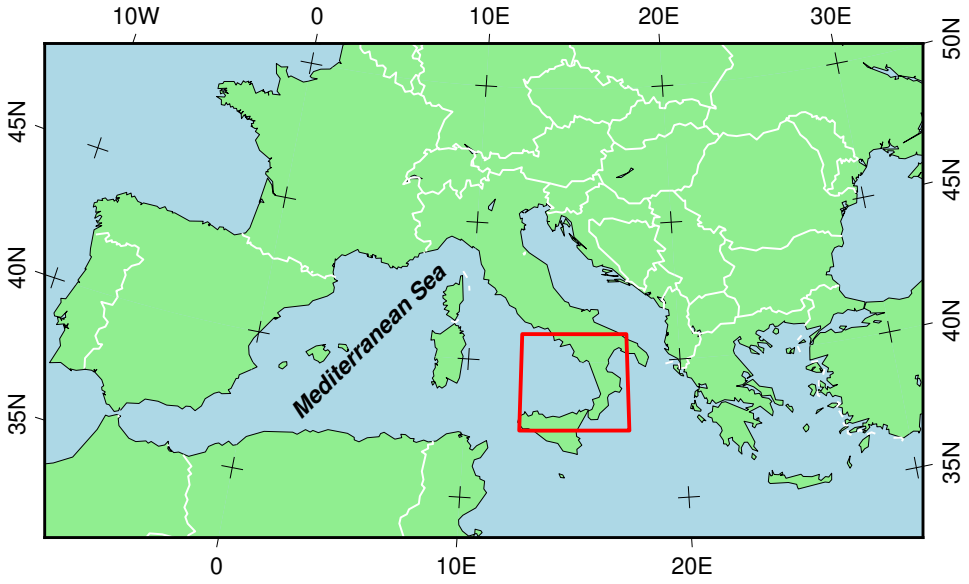

(a)

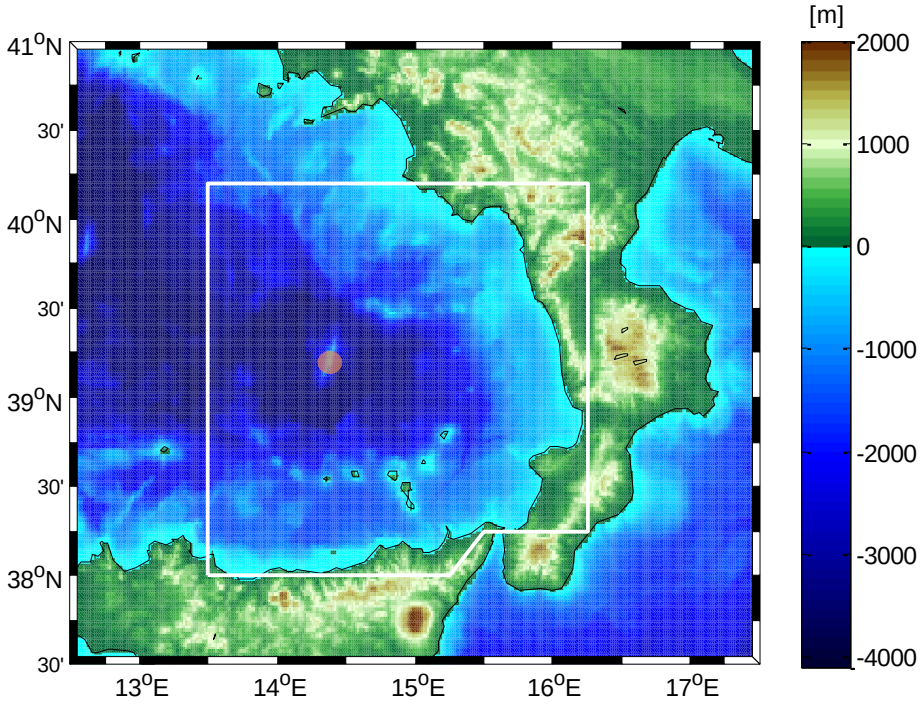

(b)

Figure 4.1: (a) Study area in the Mediterranean sea is located on the north of the Sicily island; **(b)** Digital topographic map of study area (red box in subfigure **(a)**) including the Tyrrhenian Sea. The Pliny seamount is marked by the orange circle. The altimetry data within the white polygon is used for this study.

4.1.2 Altimetry data processing

As we addressed in Chapter 3, only few satellite missions are favoured for the marine gravity modelling. In section 3.2, we introduced the data archives holding the altimetry data. In this study, we make use of CryoSat-2, Jason-1 and SARAL/Altika geodetic mission data only. Jason-1 and SARAL/Altika geodetic phase products are only available from RADS. CryoSat-2 SAR mode data is extracted for the year 2014 and 2015 (cycle 149 til 174) from RADS, LARS and GPOD archives, respectively. Then the CryoSat-2 data is merged with Jason-1 and Altika data to construct 3 different datasets that will be identified by the names of the archives later.

We use the 1-Hz altimetry observations (6∼7 km along track spacing) for the marine gravity modelling. In the RADS data, the 1-Hz observations that have range precision larger than 15 cm are discarded in the subsequent processing. From the LARS data, we produced the 1-Hz observations by averaging the 20-Hz echoes. Each 1-Hz observation is computed with at least ten 20-Hz echoes. The standard deviation (std.) of the averaged 20-Hz echoes is used as the range precision. If the standard deviation is larger than 15 cm, the 1-Hz observation is also discarded. In the GPOD database, the CryoSat-2 1-Hz observations with range precision better than 2 cm can be directly extracted. As a common criteria for data editing, 1-Hz observations with range precision better than 15 cm are used only.

In the framework of remove-compute-restore (RCR) technique, we initially tested the altimetry data (SSHs) from RADS and removed the EGM08 geoid heights up to d/o 2190 and MDT associated with EGM08. The residual height anomalies after cross-over adjustment are shown in Figure 4.2 along with the empirical covariance estimates. The residual signal remaining after removing the EGM08 (d/o 2190) is so small with a std. of 0.038 m. The residual signal along the coast show consistency which imply the consistency of altimetric observations. One can also

observe from the plot of empirical covariances that the correlation length of the residual signal is around 30 km ($\sim 0.3^\circ$ spherical distance).

In the processing of the altimetry data, we did not employ any data smoothing or averaging to reduce the noise in the measurements. The cross-over adjustment technique employed here applies to the tracks to remove the trend and biases among the tracks only. Therefore, when removing the full resolution EGM08 model, the signal-to-noise ratio (SNR) in the residual field is so small and it will be hard to fit a proper covariance model as shown in Figure 4.2b.

In this study, we intentionally preserve some signal from the EGM08 model to increase the SNR in the residual height anomalies. Hence, we reduce the maximum spherical harmonic degree of the EGM08 model to 1080, which will result in the shortest half-wavelength of the reference EGM08 is around 20 km (10 arc-minute resolution). The wavelength is still smaller than the extent of the region (~200 km).

To conclude, the 1-Hz SSHs are retrieved from the RADS, LARS and GPOD archives and EGM08 (d/o 1080) and MDT are removed at the very first step. The

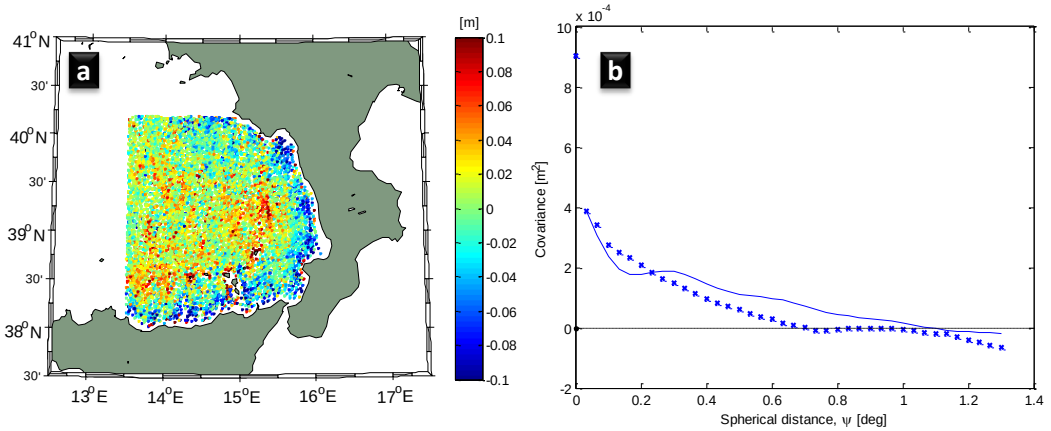

Figure 4.2: (a) Residual height anomaly after cross-over adjustment for only removing the EGM08 model (d/o 2190). (b) empirical covariance (* symbols) and Tscherning&Rapp covariance model fitting (curved lines).

height anomalies after cross-over adjustment for RADS, LARS and GPOD data are shown in Figure 4.3. The features remaining in the residual signal are quite similar. We can observe that the LARS and GPOD data are closer to the coastal lines than the RADS data and have slightly more observations (see Appendix B). The statistics of the height anomalies are shown in Table 4.1.

Table 4.1: Statistics of residual height anomalies after cross-over adjustment, unit: m

Database	# obs.	mean	std.	min	max
RADS	9471	0.003	0.059	-0.460	0.265
LARS	10304	0.003	0.061	-0.282	0.343
GPOD	9896	0.003	0.059	-0.289	0.304

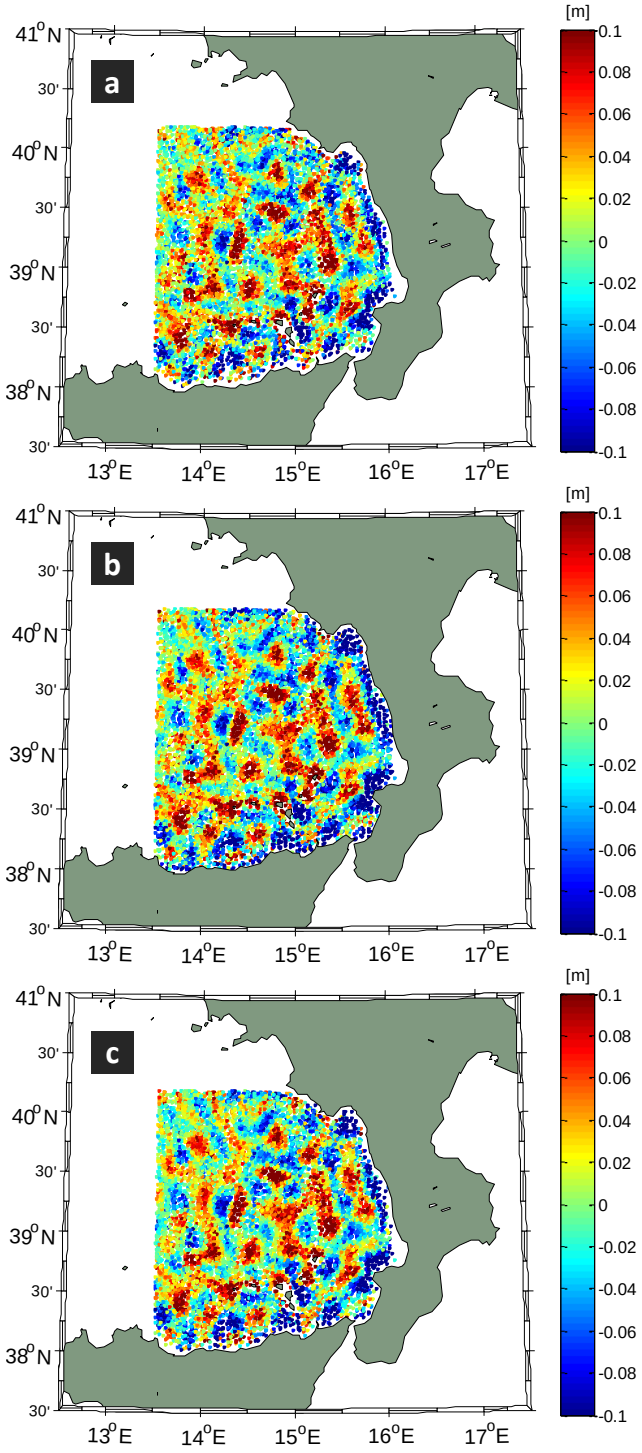

Figure 4.3: Residual height anomaly after the cross-over adjustment (a) RADS (b) LARS (c) GPOD.

4.1.3 Computation of RTM effects

To compute the RTM effects, we need to choose the digital elevation models of this region. The SRTM30_PLUS topography and GEBCO_2014 are the 30 arc-second topography grids publicly available. The EMODnet bathymetry is available with 7.5 arc-second grid spacing. Although the EMODnet bathymetry is available with 4 times denser grid spacing, the sea floor resolved by the two 30 arc-second models is almost the same. The EMODnet ship soundings are integrated to the other two models. After analysing the source identification grids as in Appendix A, we proceed with the GEBCO_2014 as the fine resolution topography and construct the reference surface to be used in the RTM computation. The TCGRID program included in the GRAVSOFT package is used to achieve the low pass filtered reference surface whose resolution is 10 arc-minutes.

We computed the RTM effecs N^{RTM} (see Eq.(2.36)) with an integration radius of 200 km, a constant rock density of 2670 kg/m^3, and sea water density of 1030 kg/m^3. The RTM effects are firstly computed on a one arc-minute grids and subsequently used to reduce the altimetry data.

The RADS residual height anomalies after removing EGM08 (d/o 1080) and MDT with and without RTM effects are shown in Figure 4.4. The statistics in Table 4.2 suggest the reduction in signal variance is negligible. The RTM effects are supposed to reduce the residual signal, but the residual signal is partly "enhanced" by subtracting the RTM contributions. Outside the ellipse in Figure 4.4b, the residual height anomalies are indeed reduced by removing RTM effects. Inside the ellipse, the signal is stronger and longer wavelength features can be observed. The bathymetry is mostly deep ($\sim$ 3500 m) and flat in the area bounded by the ellipse. The additional signal also distorts the empirical covariance estimates. In Figure 4.4c, the correlation length of height anomalies with N^{RTM} removed (red curve) is

apparently longer than that without removing N^{RTM} (blue curve). The long wavelength features introduced by removing N^{RTM} make it hard to fit a proper covariance model as well. Hence, we proceed without removing (or restoring) the RTM contributions.

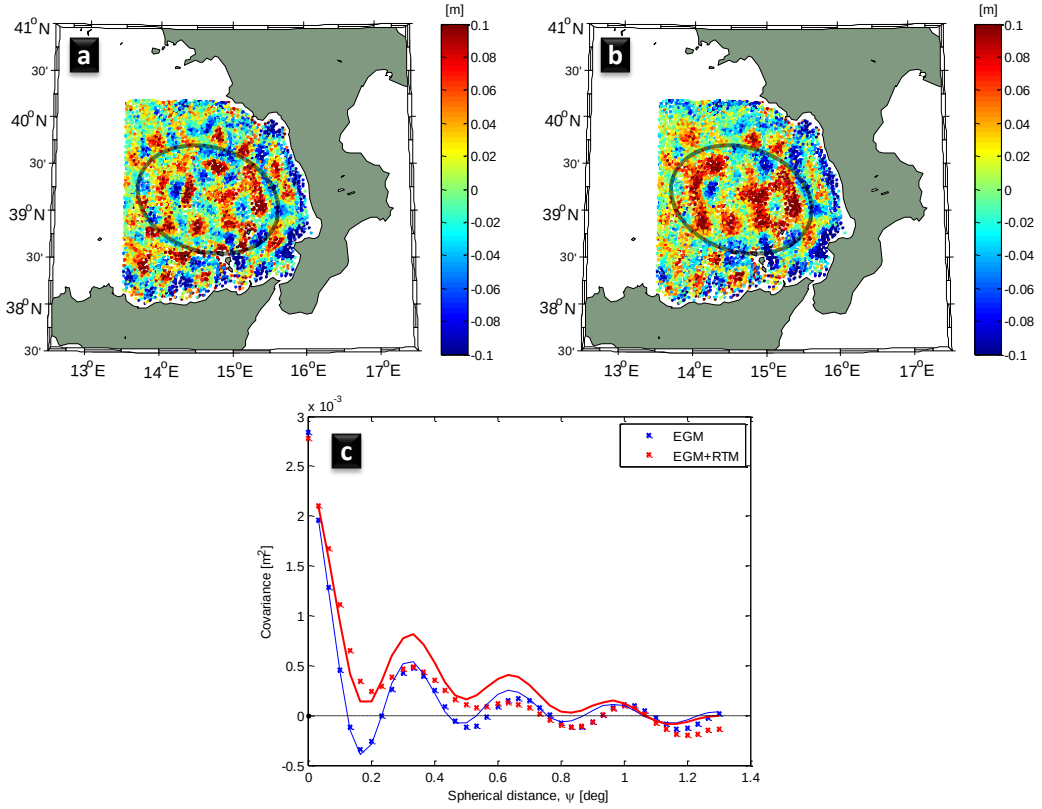

Figure 4.4: Residual height anomaly from RADS dataset after cross-over adjustment (a) for only removing the EGM08 (d/o 1080) (b) for removing the EGM08 (d/o 1080) and also RTM effects (c) empirical covariance (* symbols) and Tscherning&Rapp covariance model fitting (curved lines). The blue curves refers to (a) while the red curves refers to (b). The area bounded by ellipse has deep and flat bathymetry.

Table 4.2: Statistics of residual height anomalies for removing EGM08 model only (Figure 4.4a) and removing both EGM08 and RTM effects (Figure 4.4b), unit: m

Signal reduction	mean	std.	min	max
EGM08	0.003	0.059	-0.460	0.265
EGM08+RTM	0.005	0.058	-0.451	0.217

4.1.4 Covariance modelling

For the covariance modelling, the variance term estimated by EMPCOV is excluded, due to the fact that it contains the both the signal and noise, and sometimes the signal is insignificant (or very low signal-to-noise ratio). The Tscherning&Rapp model described in section 2.5.3 is used with the error degree variances $\left(\sigma_n^{ERR}\right)^2$ in Eq.(2.51) computed from EGM08 model up to d/o 1080. The covariance model fitted to the empirical covariances are shown in Figure 4.5. In general, the covariance model fits well with the discrete empirical covariances at the short wavelengths. We can also observe the correlation length of altimetry data, which is around 0.1° spherical distance (approx. 10 km).

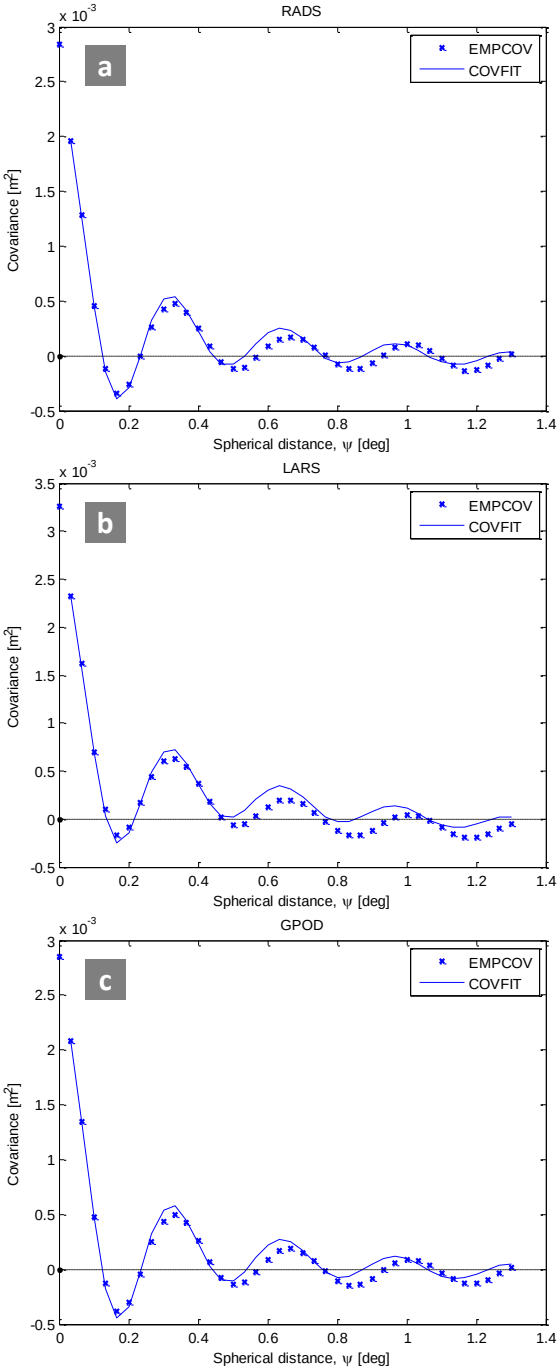

Figure 4.5: Empirical covariance (* symbols) and covariance model fits (blue continuous curves) for residual height anomalies shown in Figure 4.3 (a) RADS (b) LARS (c) GPOD.

4.1.5 Gravity anomalies from LSC

The GEOCOL19 program with parallel processing option (*Kaas et al.*, 2013) is used to derive the marine gravity anomalies along the shipborne gravity measurements from Morelli cruises (*Allan and Morelli*, 1971) and BGI data (Figure 4.6). The extent of shipborne survey is clipped to be 0.1° smaller than that of altimetry data on the west and north boundaries. The shipborne measurements are downsampled to a 7.5 arc-second grid cells for the purpose of Mediterranean gravimetric geoid modelling (see GEOMED2 project for details (*Barzaghi et al.*, 2018)). To have sufficient degrees of freedom in the system equation and save the computation time, we further downsampled by a factor of four to get 2264 samples in the study area.

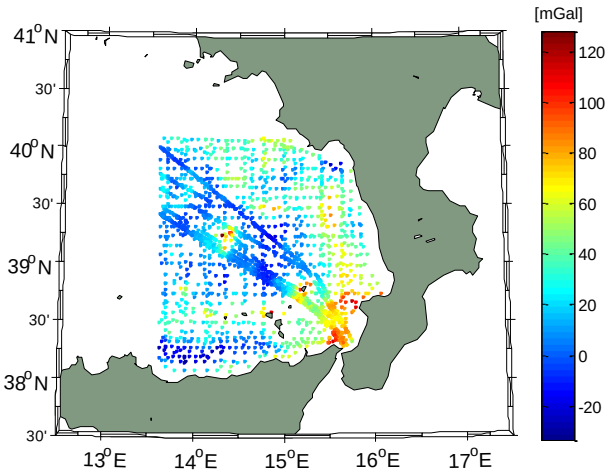

Figure 4.6: Ship gravity measurements in the study area. The gravity measurements are initially prepared for the GEOMED2 project.

The output from LSC is the residual gravity anomalies $\triangle g_r$ in Eq.(2.37). The residual gravity anomalies from RADS height anomalies are shown in Figure 4.7. Similar figures for LARS and GPOD data are omitted. The error estimates of the predictions have a median value of 2.38, 2.35 and 2.28 mGal for RADS, LARS and GPOD data, respectively. The location of predictions with larger (>3 mGal) differ-

ences are shown in Appendix B. The prediction error near the coastal lines tends to be higher due to the sparse altimetry observations. On almost all prediction points, the prediction error is smaller than 4 mGal for LARS and GPOD data, which is significantly better than Sandwell gravity field V23.1 (*Sandwell et al.*, 2014) errors in the same region (see Figure B.3).

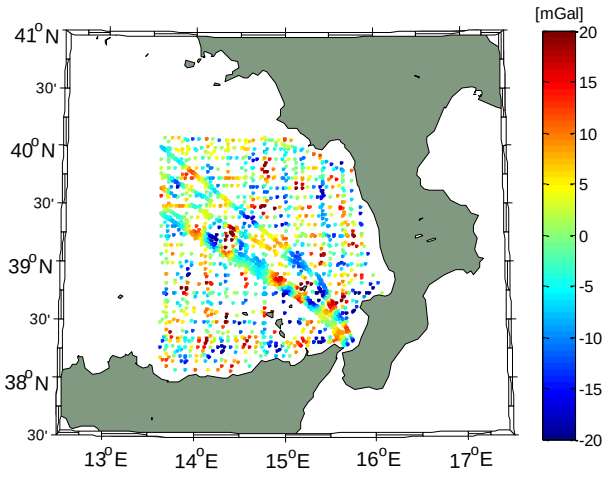

Figure 4.7: Residual gravity anomalies estimated using LSC from RADS height anomalies in Figure 4.3a.

4.1.6 Validation

We restore the full gravity signal by adding the EGM08 gravity anomalies (d/o 1080) to the residual gravity anomalies predicted from LSC. Then, a direct comparison with shipborne measurements can be conducted. The difference of predicted gravity anomalies and EGM08 are shown in Figure 4.8. The statistics comparing with EGM08 and shipborne measurements are shown in Table 4.3. Note that the EGM08 and ship gravity are not error-free. The standard deviations of the differences reflects the relative precision of the predicted gravity anomalies. The altimetric gravity anomalies agree with ship measurements with a std. of 5.05, 4.86 and 5.03 mGal, respectively. The difference of ship measurements and EGM08 has a

std. of 5.13 mGal. By using altimetry for marine gravity modelling, we get minor improvement. The relative precision of altimetric gravity anomalies compared to EGM08 is 3.50, 3.36 and 3.48 mGal, respectively. In both cross-comparisons, the gravity anomalies predicted from LARS altimetry database have the best relative precision.

Assuming the error sources are independent between EGM08, shipborne gravity and predicted gravity anomalies, we can estimate the precision of the individual dataset through error propagation. Take the gravity anomalies estimated from LARS database as an example. The standard deviation of the predicted gravity anomalies is $\sigma^{LARS} = 2.07$ mGal. The error in the EGM08 and ship measurements are $\sigma^{EGM} = 2.64$ mGal and $\sigma^{Ship} = 4.39$ mGal, respectively. The estimates suggest that the shipborne measurements are not optimal for assessing the accuracy of the predicted gravity anomalies. Nevertheless, in this region, 2.07 mGal of error in the altimetric gravity anomalies is quite encouraging.

Table 4.3: Statistic of the difference between predicted gravity anomalies from 3 different datasets, shipborne gravimetry $\triangle g^{Ship}$ and EGM08, in total 2264 samples, unit: mGal

	mean	std.	min	max
$\triangle g^{RADS} - \triangle g^{EGM}$	0.21	3.50	-15.64	14.52
$\triangle g^{LARS} - \triangle g^{EGM}$	0.41	3.36	-16.82	20.10
$\triangle g^{GPOD} - \triangle g^{EGM}$	0.26	3.48	-20.83	14.98
$\triangle g^{Ship} - \triangle g^{EGM}$	0.50	5.13	-18.51	78.93
$\triangle g^{RADS} - \triangle g^{Ship}$	-0.38	5.05	-79.72	24.81
$\triangle g^{LARS} - \triangle g^{Ship}$	-0.18	4.86	-78.70	18.69
$\triangle g^{GPOD} - \triangle g^{Ship}$	-0.33	5.03	-79.56	19.55

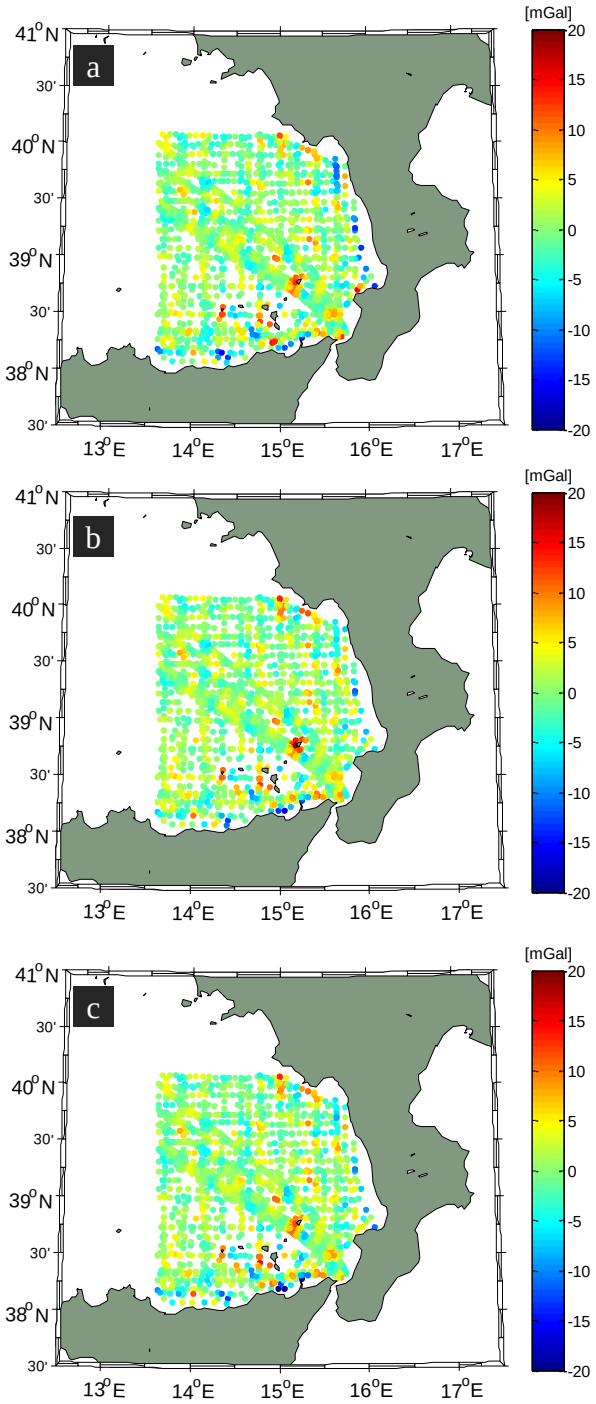

Figure 4.8: Difference of (a) RADS (b) LARS (c) GPOD altimetric gravity anomalies and EGM08 over the shipborne survey locations.

4.2 Case study: Indonesian coastal zone

Indonesia is the world's largest island country. There has been several airborne gravity campaigns since 2009 for mapping the gravity field and height system unification of Indonesia. The Sulawesi island is the fourth largest island among the thousands of islands. In the case study we will derive the gravity anomalies along the airborne survey lines in the *Gulf of Tomini* surrounded by the central and north Sulawesi island (see Figure 4.9). The Gulf of Tomini extends 400 km in longitude direction, and as wide as 200 km in the latitude direction in the west. The Togian islands are right in the center of the gulf. The traditional altimetry satellites have very few valid observations in the past and with the dense CryoSat-2 observations, we aim to improve the coastal marine gravity.

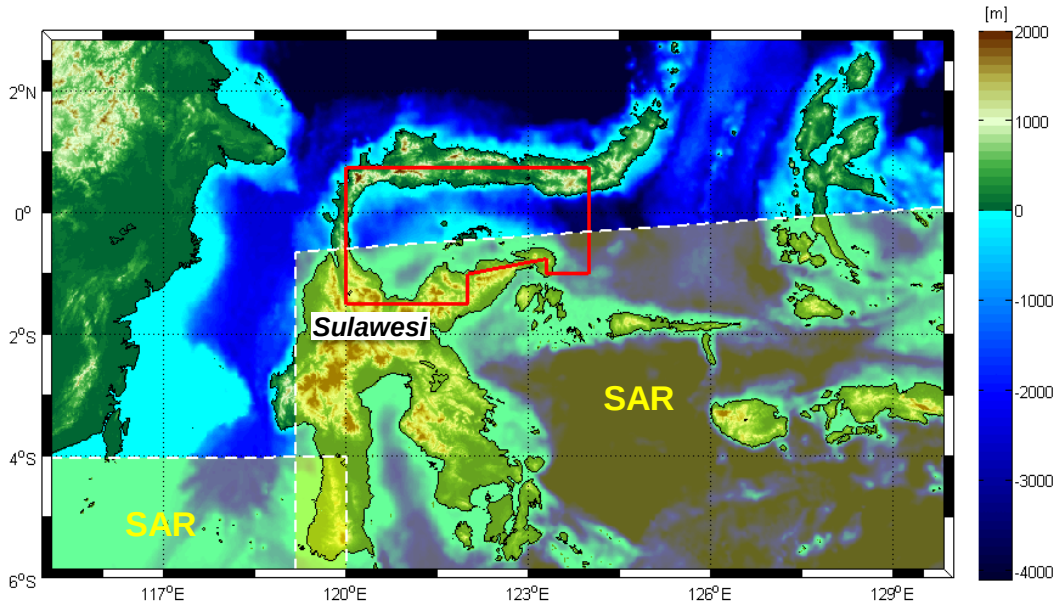

Figure 4.9: Digital topography around the Sulawesi island. The red polygon refers to the Gulf of Tomini and the Togian islands are right in the center of the gulf. The half-transparent yellow polygons with white dashed lines show the margins of the CryoSat-2 SAR mask.

In the *Gulf of Tomini*, we found significant long wavelength features from the geoid in the remove step of RCR approach. In addition, the presence of islands in the study area could degrade the performance of cross-over adjustment since the altimetry measurements are less reliable and sparse near the islands. Hence, the study area is divided into two patches, namely the *west patch* and *east patch*, with approx. 100 km overlap including the Togian islands in both patches.

4.2.1 Residual height anomalies

In Figure 4.9, the geographic mask of CryoSat-2 is also displayed. The CryoSat-2 SAR mode mask only partially covers the *Gulf of Tomini*, and the SIRAL instrument operates in the LRM mode elsewhere. Therefore, the altimetry data is a mix of LRM and SAR mode acquisitions. To be consistent and to avoid the data gap or biases at the margins of the operation mask, we only retrieve altimetry data from the RADS database.

Jason-1 and SARAL/Altika data are extracted from RADS. CryoSat-2 data is extracted for 4 years from 2014 to 2017 (cycle 149 til 200). Since the track spacing at the equator is as much as 8 km for CryoSat-2, it is reasonable to have two more years of CryoSat-2 data to have more cross-over points and conduct robust cross-over adjustment. Similar to the Mediterranean case, the 1-Hz observations with poor range precision (>15 cm) are discarded.

First of all, the EGM08 model up to d/o 1080 is removed. The RTM effects are computed from the SRTM30_PLUS global topography grids (see Appendix A) using the same procedure as in the Mediterranean study. Then, the RTM height anomalies N^{RTM} are also removed to further reduce the signal.

In contrast to the Mediterranean study, when removing the RTM effects, the

residual field is further reduced. It is because the SRTM30_PLUS V11.0 bathymetry was inverted from the altimetric gravity anomalies which incorporated four years CryoSat-2, 1.5 years of Envisat and 13 months of Jason-1 by the time it was released in Nov. 2014. There are no bathymetric surveys available in the region. This is examined through the source identification grids of SRTM30_PLUS. Hence, the wavelength band of the topography is still limited by the shortest wavelength of the altimetric gravity model which is around 20 km (*Sandwell et al.*, 2013).

The residual height anomalies after cross-over adjustment are shown in Figure 4.10 and 4.11. The remaining signal is significant (see Table 4.4) which implies that the existing EGM08 model is problematic in Gulf of Tomini. The source marine gravity integrated in the EGM08 was DNSC07 which is a predecessor version of DNSC08GRA (*Andersen et al.*, 2010). The DNSC07 model was produced using the altimetry data from the Geosat and ERS-1 geodetic missions along with the repeat track missions (Topex, Envisat, etc.). Apparently, the study area is not well modelled by the conventional altimetry missions before the launch of CryoSat-2.

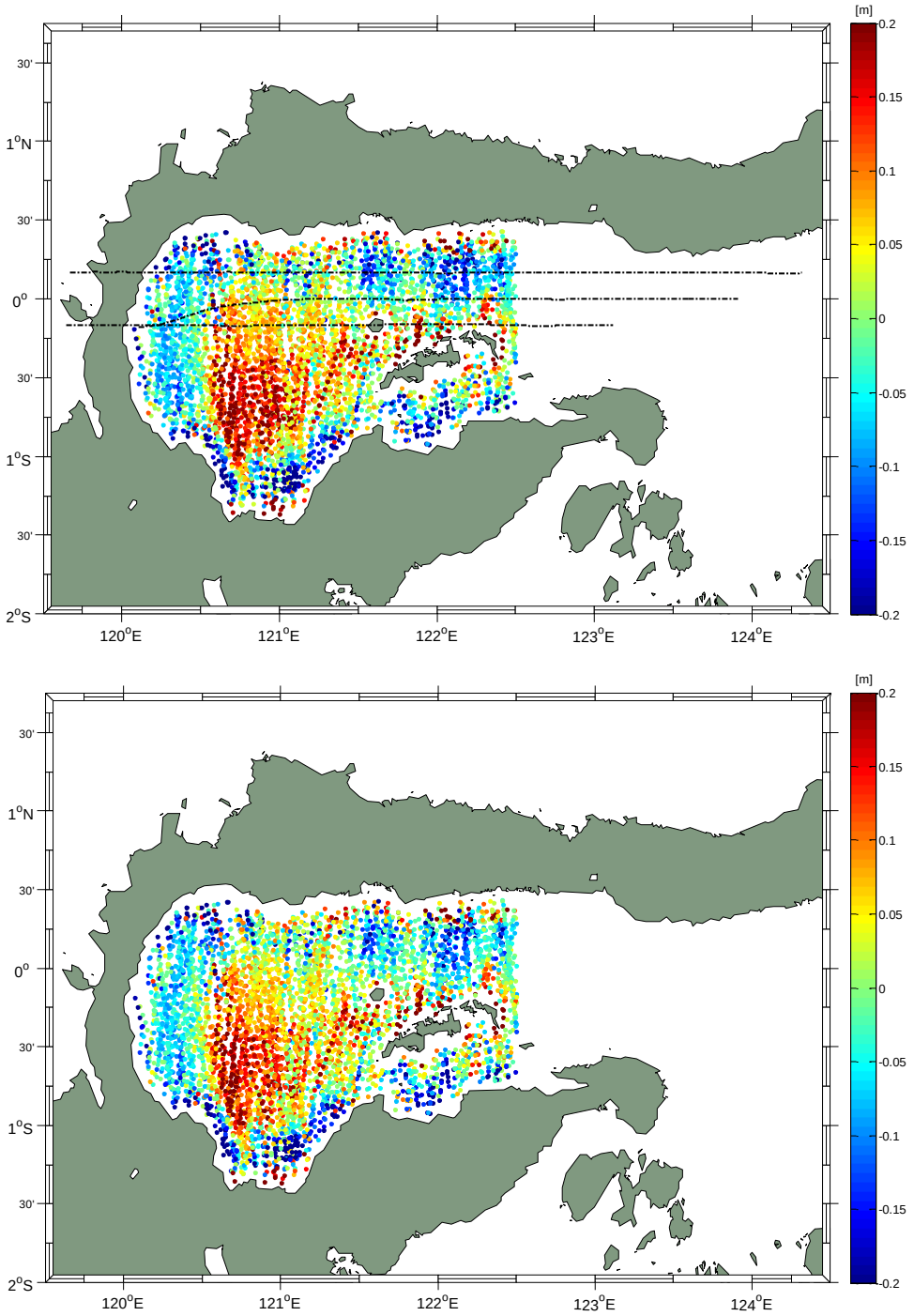

Figure 4.10: Residual height anomalies in the west half of the gulf. The top panel shows the height anomalies after removing the EGM08 only; the bottom panel shows the height anomalies after removing EGM08 and RTM effects. The dashed lines in the top panel indicate the airborne survey trajectory.

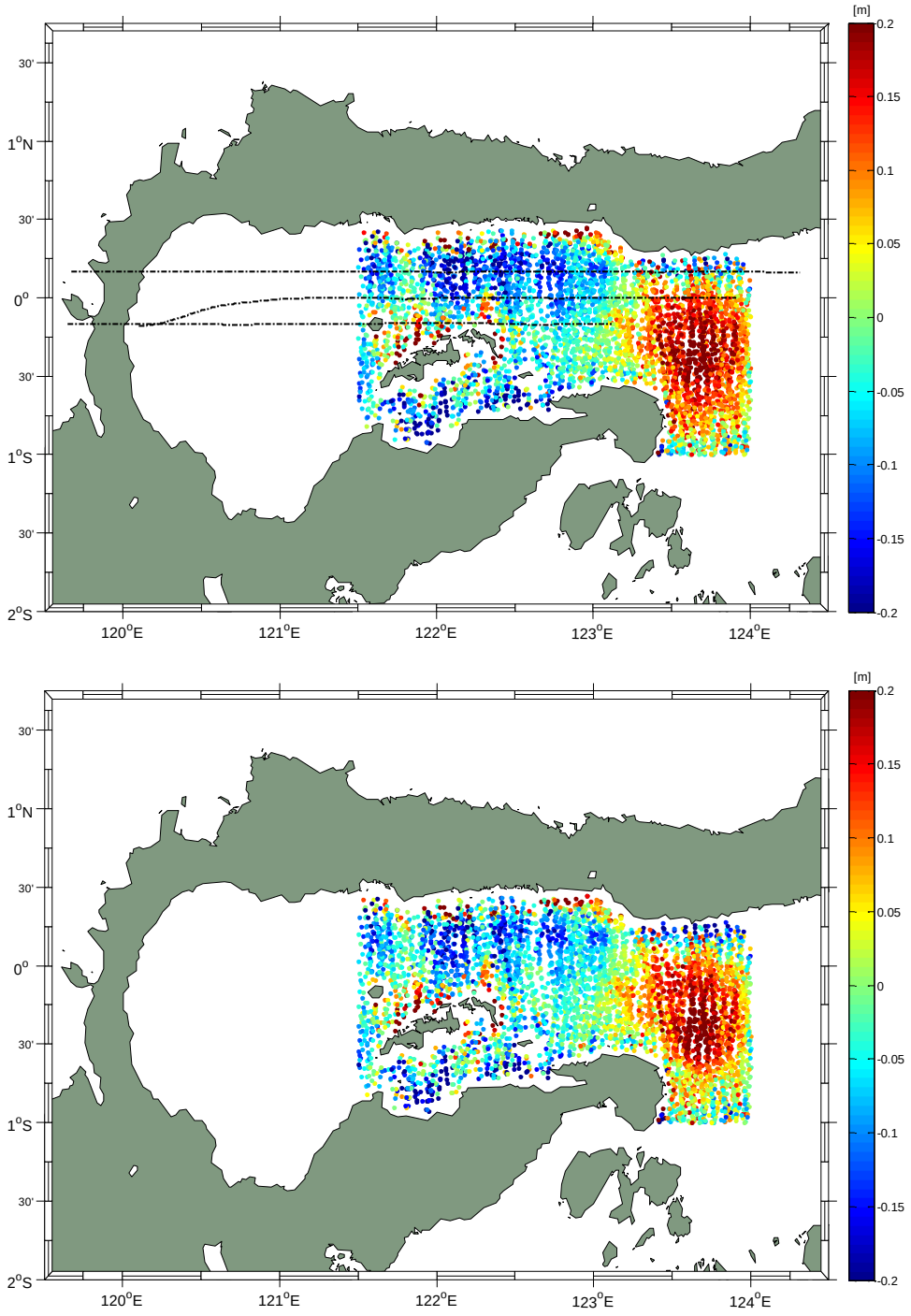

Figure 4.11: Residual height anomalies in the east half of the gulf. The top panel shows the height anomalies after removing the EGM08 only; the bottom panel shows the height anomalies after removing EGM08 and RTM effects. The dashed lines in the top panel indicate the airborne survey trajectory.

Table 4.4: Statistic of residual height anomalies after the cross-over adjustment, unit: m

	signal reduction	# obs.	mean	std.	min	max
west patch	EGM08	5009	0.0083	0.120	-0.586	0.648
	EGM08+RTM	5009	0.0076	0.113	-0.564	0.629
east patch	EGM08	4944	0.0100	0.121	-0.622	0.668
	EGM08+RTM	4944	0.0076	0.110	-0.575	0.584

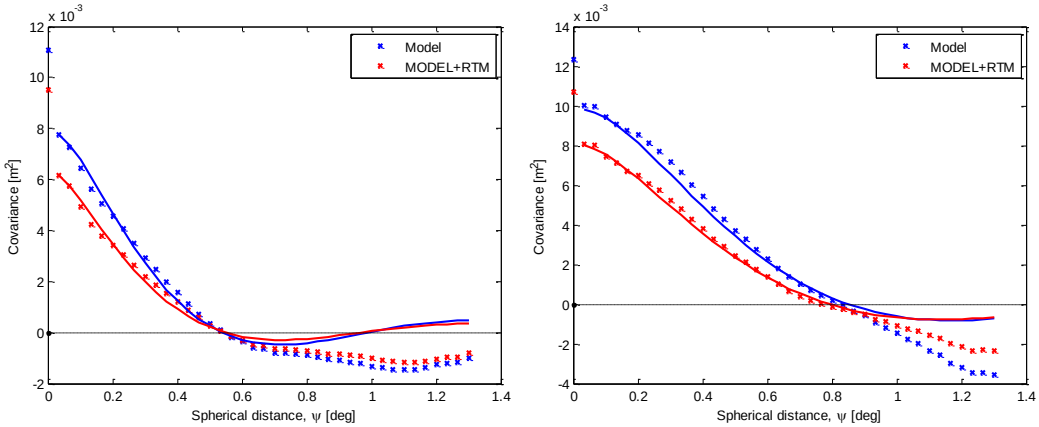

Figure 4.12: Empirical covariance (* symbols) and covariance model fits (continuous curves) for residual height anomalies *left:* for the west patch (Figure 4.10) *right:* for the east patch (Figure 4.11). The blue color refers to removing EGM08 model only while the red refers to removing both the EGM08 and RTM effects

4.2.2 Gravity prediction and validation

The empirical covariance and covariance model fitting (see Figure 4.12) can be conducted from the residual height anomalies shown in Figure 4.10 and 4.11. The process of finding the right parameters for covariance fitting models are by trial and error, since the empirical covariances imply long correlation length (as much as 45 km). Also, note that the residual field is not homogeneous and anisotropic. It is not quite optimal to use LSC in such cases as the LSC algorithm requires the residual field to be isotropic and homogeneous (*Moritz*, 1980).

Nevertheless, the residual gravity anomalies are estimated using LSC along the airborne survey lines. The full gravity anomalies are obtained by adding back the EGM08 gravity anomalies computed up to d/o 1080 $\triangle g^{EGM}$ and RTM gravity anomalies $\triangle g^{RTM}$. The statistics of the differences between the airborne gravity and predicted gravity anomalies are shown in Table 4.5. We can hardly conclude that the predicted gravity anomalies from altimetry improved the gravity field in the region as the mean and std. of the differences with airborne gravity surveys are 0.70 ± 10.83 mGal and -7.55 ± 12.03 mGal in the two patches. The large mean difference suggest the gravity prediction results on the east path are biased. The comparison between the airborne surveys and EGM08 also gives std. of 10 to 12 mGal. We trust the quality of airborne gravity surveys and most probably, the reference field EGM08 have long wavelength problems in this region.

Table 4.5: Statistic of the differences between predicted gravity anomalies from altimetry $\triangle g^{alt}$, airborne gravimetry $\triangle g^{AG}$ and EGM08 $\triangle g^{EGM08}$, in total 938 and 834 samples for west and east patch, respectively. unit: mGal

		mean	std.	min	max
west patch	$\triangle g^{alt} - \triangle g^{EGM08}$	-1.00	7.83	-21.65	28.72
	$\triangle g^{AG} - \triangle g^{EGM08}$	-1.70	10.28	-26.18	29.13
	$\triangle g^{alt} - \triangle g^{AG}$	0.70	10.83	-35.20	30.63
east patch	$\triangle g^{alt} - \triangle g^{EGM08}$	-2.08	7.94	-23.94	25.15
	$\triangle g^{AG} - \triangle g^{EGM08}$	5.47	12.25	-26.36	31.02
	$\triangle g^{alt} - \triangle g^{AG}$	-7.55	12.03	-29.28	21.55

4.3 Summary

In this chapter, we made two case studies for the gravity modelling from altimetry near the coastal zones. The coastal zones are selected based on the presence of external marine or airborne gravity surveys as well as the underlying topography to test the RTM effects over the oceans.

Coastal zone altimetry has been challenging since the altimetry waveforms could be contaminated by land near the shorelines. In the coastal zones, the range precision of the altimetry is poorer than that in the open ocean. This will require more data editing (screening) and quality check before the data is used for the gravity modelling. We manually define the polygons (white polygon in Figure 4.1b and red polygon in Figure 4.9) to filter out the altimetry points that are on the other side of the larger islands. This simple process guarantees that the altimetry tracks in the study area are continuous (with minor data gaps across the very tiny islands) and most importantly the sea state (wind and currents) are identical along the altimetry footprints.

We take the processed CryoSat-2 altimetry data from three different data sources, namely RADS, LARS and GPOD, respectively. CryoSat-2 data is merged with Jason-1 and SARAL/Altika data to construct three different datasets in the Mediterranean case. The general features remaining in the residual height anomalies are quite similar. We have more altimetry observations and near coastal coverage from the LARS data. Also, predicted gravity anomalies from LARS dataset show the best precision compared to the other two datasets.

The RTM effects are computed for both regions and the signal reduction on sea surface heights are analysed. The expectation is that RTM effects account for the short wavelength beyond the resolution of EGM08 models and hence re-

duce the residual field. In the Mediterranean study, signal variance is reduced slightly, but more long wavelength features are observed by removing the RTM height anomalies (N^{RTM}). However, in the Indonesian case, by removing the RTM height anomalies (N^{RTM}), we managed to reduce the residual height anomalies as expected. The resolution of the topographic model used for the RTM may explain the performances of RTM. In areas with no or few bathymetric ship soundings, the bathymetry was inverted from altimetric gravity anomalies (*Sandwell et al.*, 2013; *Sandwell and Smith*, 2009). The resolution SRTM30_PLUS (GEBCO_2014) is limited by the resolution of altimetric gravity anomalies. In addition, the presence of sediments can also lead to problematic (unexpected) RTM results. Specifically, in the Mediterranean case, the GEBCO_2014 bathymetry has fairly good coverage of dense ship soundings. Only the coastal gaps are filled by SRTM30_PLUS bathymetry. The RTM signal reduction is effective near the coastal relief but not in the deep bathymetric part in the center of study area. In particular, we observed long wavelength features in the relatively flat deepest segment of the study area. The areas likely have sediments that buried the subseafloor structures associated with gravity. Meanwhile, the constant rock density assumption could also be the source of the problem. These cause the RTM to be problematic. Whereas, in the Indonesian case, the SRTM30_PLUS is the main source for digital elevation models. Very few ship soundings are available near the Gulf of Tomini. The EGM08 model is so poor and the recent version of SRTM30_PLUS bathymetry is effective in reducing the sea surface heights. Therefore, we proceeded without including RTM effects in Mediterranean case, while including RTM effects in the Indonesian case.

The empirical covariances are estimated directly from residual height anomalies and covariance models are fitted afterwards. Meanwhile, the performance of the RTM effects can also be assessed via the covariance plots. The signal variance and correlation length (favourably) should decrease if the RTM effects are correct.

The residual gravity field w.r.t. EGM08 is an enhancement to the EGM08 in the Mediterranean case. In the Indonesian case, the gravity prediction is not quite satisfactory as we do not attain dramatic improvement through the validation against the airborne gravity survey in the region. Moreover, we observed remaining long wavelength features in the residual height anomalies. In the next generation of EGM (EGM2020), such long wavelength signals may be well modelled by including the GOCE satellite measurements.

Part II

Bathymetry prediction

Chapter 5

Bathymetry mapping

This chapter includes short introductions to the conventional bathymetry mapping techniques and bathymetry mapping from space in Section 5.1. Gravity and topography relationship and the transfer function of topography and gravity is described in Section 5.2.

5.1 Introduction

5.1.1 Conventional bathymetry mapping

Bathymetry is the measurement of water depth from the water surface to the sea floor. Bathymetry mapping is important for safe navigation of ships, water volume computation, mineral mining and fishing industry, harbor construction and underwater engineering construction. The depth of water can be determined by transmitting sound waves into water, and subsequently receiving the return signal from the sea floor. Thus, the time interval between emission and return of a pulse is recorded and by multiplying with speed of sound in water, the water depth can

be computed. Such technique is called *echo-sounding*.

Echo-sounding gives the direct measurement of the water depth. The echo-sounding devices are usually mounted at the bottom of the ships and conduct the measurements along the sailing trajectories. The early generations of echo-sounding instruments transmit and receive single pulse at a time and hence, called *single-beam sounder*. Modern echo-sounder, such as side-scan sonar and *multi-beam sounder*, emits a sound wave in the transverse direction of the sailing direction with an opening angle of as much as 120°. The multi-beam sounders can map 10-20 kilometre wide swaths of the sea floor at a resolution of 100 to 200 m, depending on the operating frequency.

However, the efficiency of echo-sounding is limited by the speed of the ship, thus, constrains how fast the ocean may be mapped (*Smith and Sandwell*, 2004). It is estimated that a complete swath survey of the deep ocean could take about 200 years with a cost of billions of US dollars (*Carron et al.*, 2001). Including shallow coastal areas could take even longer time.

By now, only a small proportion of the ocean area has been surveyed by the echo-sounding. However, not all of this data is publicly available. Some data is classified, for instance sonar soundings from submarines are collected for military purposes, while some commercial surveys are held by their collectors. The publicly available ship sounding data can be accessed via NOAA National Center of Environmental Information (NCEI)[1]. In general, the sounding data is dense at the ports and along the ocean ridges (as it has been prime interest for geophysics), while it is sparse in the deep ocean. Also, it is denser in the northern hemisphere than in the southern hemisphere. Before the birth of GPS, the ship sounding measurements are geo-located by the celestial navigation (*Smith*, 1993), and may contain gross errors.

[1] https://maps.ngdc.noaa.gov/viewers/bathymetry/

5.1.2 Bathymetry prediction from gravity anomalies

Given the fact that it is inefficient and costly to operate echo-sounding surveys, the indirect measurements of the bathymetry may be considered. The gravity anomalies caused by the topography can be the clue to compute the bathymetry from marine gravity anomalies. The sea surface gravity and sea floor topography relationship is described by *Parker* (1973) and *McKenzie and Bowin* (1976) . On a limited bandwidth, the linear correlation between bandpass filtered gravity and bathymetry is estimated by statistical Pearson's correlation coefficient and the gravity-to-topography ratio (or scaling factor) can be determined by robust linear regression. *Smith and Sandwell* (1994) developed the algorithm to predict the bathymetry from gravity in the 1990s.

The gravity associated with the sea floor topography are measured at the sea level. The gravity anomalies observed at the sea level has different signatures depending on the mean ocean depth as shown Figure 5.1. The weakening of gravity signal is caused by upward continuation of gravity anomalies from the sea floor to the sea level. This is inevitable in the prediction of bathymetry from gravity anomalies.

5.2 Gravity and topography relationship

5.2.1 Parker's formula

Given the topography elevations, gravity forward modelling can be conducted in the spatial domain by Newtonian integration as shown in Eq.(2.39). This is commonly done by numerical integration of topographic mass elements (e.g., prisms, tesseroids and polyhedra) with varing density. Assuming constant density contrast,

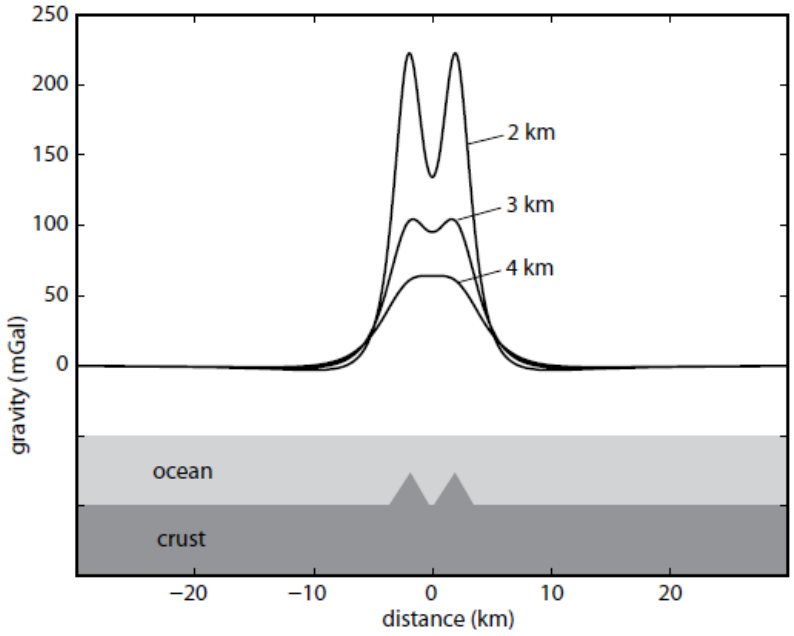

Figure 5.1: Illustration of gravity anomalies observed at the sea level generated by two seamounts, each 1 km tall, separated by 4 km on the the sea floor with varying ocean depth. Gravity signatures are strong and evident when the mean ocean depth is 2 km or less. However, the gravity signatures become weak and combine as if one wide seamount when the ocean depth is 4 km (*Wessel et al.*, 2010).

Parker (1973) presented a frequency domain approach for the rapid computation of potential anomalies. Compared to the spatial domain integration, the spectral domain computation is fast and efficient.

A cross section of a seamount with height h located at the mean ocean depth d is shown in Figure 5.2. Based on Parker's theory, the gravitational acceleration g at the sea level generated by the topographic masses at the water depth d (positive value) is given by

$$\boldsymbol{F}[g] = 2\pi G \cdot (\rho_c - \rho_w) \cdot exp(-2\pi kd) \sum_{n=1}^{\infty} \frac{(2\pi k)^{n-1}}{n!} \cdot \boldsymbol{F}[h^n], \tag{5.1}$$

where $\boldsymbol{F}[\cdot]$ denote the 2-D Fourier transform, G is the gravitational constant Eq.(2.2),

ρ_c is the density of the crust, ρ_w is the density of the sea water, k is the wavenumber being $k = \sqrt{k_x^2 + k_y^2}$ with $k_x = 1/\lambda_x$, $k_y = 1/\lambda_y$, λ_x and λ_y denotes the wavelength in X and Y directions, h is the relative height of topography element w.r.t. the sea floor, e.g., heights of seamounts. Moreover, the exponential term is the upward continuing operator. The Parker's theory assumes constant density and planar ap-

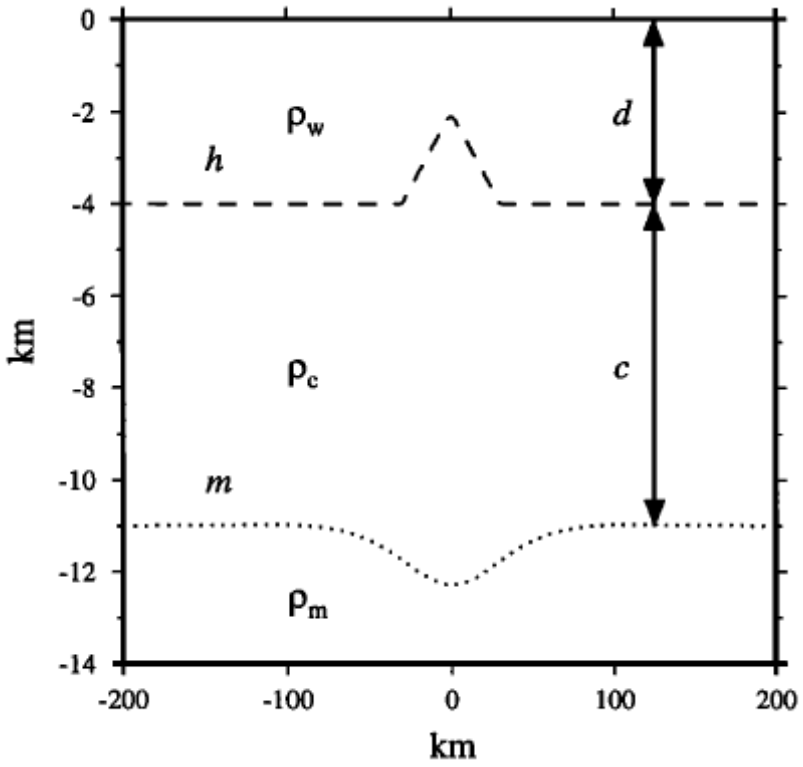

Figure 5.2: Cross section of seamount located at the mean ocean depth d. The moho deflection to be discussed later is indicated by the dotted curve. The crustal thickness c and sea water, crust, and mantle densities $(\rho_w, \rho_c, \rho_m)$are also marked (*Smith and Sandwell*, 1994).

proximation. For a limited region, the first order approximation of Eq.(5.1) gives

$$\boldsymbol{F}[g] \approx 2\pi G \cdot (\rho_c - \rho_w) \cdot exp(-2\pi kd) \cdot \boldsymbol{F}[h]. \tag{5.2}$$

5.2.2 Gravity-to-topography admittance

In fact, the gravity field is the sum of direct topographic effect, which can be computed by the Eq.(5.1) and its isostatic compensation. The admittance (or transfer) function for the *uncompensated* model can be referred from the Eq.(5.2) as

$$\boldsymbol{Z'}(k) = 2\pi G \cdot (\rho_c - \rho_w) \cdot exp(-2\pi kd). \tag{5.3}$$

In particular, the term $2\pi G \cdot (\rho_c - \rho_w)$ is known as the Bouguer constant in the computation of Bouguer correction on the sea level. The density contrast $(\rho_c - \rho_w)$ accounts for the mass deficit.

Lithosphere is the rigid outer layer of the Earth. In the flexural isostatic compensation theory, the compensation model is commonly based on a model of thin, elastic lithosphere. In response to the weight of a topographic or other load, the lithosphere will flex (or bend) (*Watts*, 2001). This flexure is described by a characteristic flexural wavelength λ_0 of the elastic plate. Mechanical stiffness of elastic plate responding to the load is characterized by flexural rigidity D, which is controlled by the effective elastic plate thickness T_e.

For the computation of isostatic compensation, the following assumptions are made: 1) the thickness of the elastic plate T_e is less than the flexural wavelength; 2) the deflection of the elastic plate is much less than the flexural wavelength; 3) the flexural rigidity, D is constant.

When there is a mass load on the elastic plate, the elastic plate deflects under the load. This downwrapping of Mohorovicic discontinuity is called Moho deflection (dotted curve in Figure 5.2). The Moho deflection, M_{moho}, is related to the topogra-

phy load by (*Banks et al.*, 1977):

$$\boldsymbol{F}[M_{moho}] = -\frac{(\rho_c - \rho_w)}{(\rho_m - \rho_c)}\Phi(k)\boldsymbol{F}[h], \tag{5.4}$$

where ρ_m is the density of mantle, $\Phi(k)$ is the isostatic response function given by (*Walcott*, 1970):

$$\Phi(k) = \left[1 + (\lambda_0 k)^4\right]^{-1}, \tag{5.5}$$

in which the flexural wavelength λ_0 is

$$\lambda_0 = 2\pi \left[\frac{D}{g(\rho_m - \rho_c)}\right]^{1/4}, \tag{5.6}$$

with the flexural rigidity D defined by

$$D = \frac{ET_e^3}{12(1-\nu^2)}. \tag{5.7}$$

The parameters involved in the Eq.(5.4) to (5.7) are listed in Table 5.1.

Table 5.1: Parameter used for the calculation of the isostatic response function $\Phi(k)$

Parameters	Value
ρ_w, density of sea water	1030 kg/m^3
ρ_c, density of the crust	2800 kg/m^3
ρ_m, density of the mental	3330 kg/m^3
d, depth of sea water	2 km
T_e, elastic plate thickness	5−30 km
g, acceleration of gravity	9.82 m/s^2
E, Young's modulus	100 GPa
ν, Poisson's ratio	0.25

At topographic wavelengths much larger than the flexural wavelength λ_0, the topography is Airy compensated. While at wavelengths much shorter than the flexural wavelength λ_0 the topography is uncompensated (*Smith and Sandwell*, 1994).

The admittance function for the *compensated* model is then given by *Watts* (2001) is as follows:

$$\boldsymbol{Z}(k) = \boldsymbol{Z'}(k) \cdot [1 - exp(-2\pi kc)\ \Phi(k)]. \tag{5.8}$$

As shown in Figure 5.3, the amplitude of the transfer function $\boldsymbol{Z}(k)$ shifts towards zero at longer wavelength because of the isostatic compensation, whereas at shorter wavelengths shift to zero due to upward continuation. With increasing elastic thickness T_e, the amplitude of $\boldsymbol{Z}(k)$ increases and the peak amplitude shifts towards the long wavelength. For the case of $T_e \to \infty$, with a complete rigid plate, there is no moho deflection and thus, there is no compensation (red curve in Figure 5.3).

The inverse admittance function $[Z(k)]^{-1}$ with unit $m/mGal$ shown in Figure 5.3, is a transfer function of gravity input and topography output system. At wavelength shorter than 100 km, one can safely proceed with uncompensated model without considering the isostatic compensation, provided that elastic plate thickness T_e is known to be greater than 5 km.

The admittance functions with varying water depth and density are demonstrated by *Watts et al.* (2006). The behaviour of transfer function $Z(k)$ changes slightly with varying density and water depths. The overall effect is small compared to the changes in elastic plate thickness as illustrated by *Watts et al.* (2006).

5.2.3 Inverse Nettleton procedure

Nettleton's method (*Nettleton*, 1939) of density determination is a process of linear regression, in which the proper density of the surface material ρ_s yields the Bouguer correction $2\pi\rho_s G h_s$ best fitting the free-air gravity anomalies. Predicting the bathymetry from gravity is a process determining the best fitting scaling factor

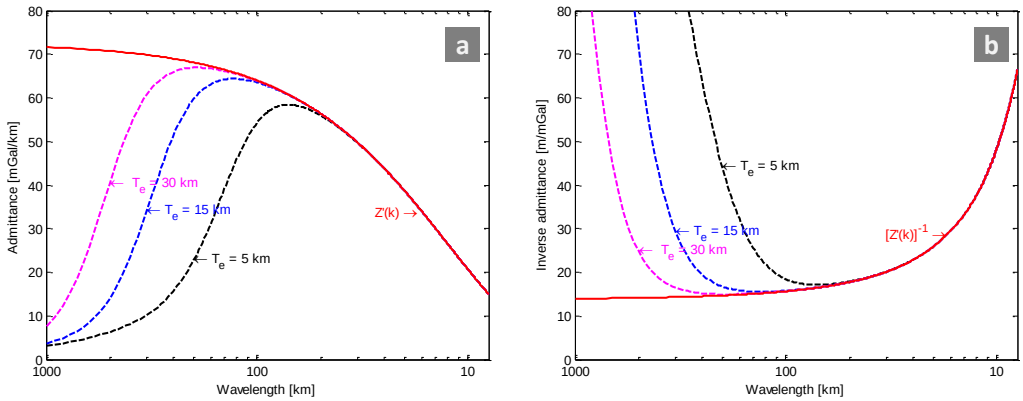

Figure 5.3: (a) The admittance function $Z(k)$ with unit $mGal/km$. (b) Inverse admittance $[Z(k)]^{-1}$ with unit $m/mGal$. The bottom scale is transformed from wavenumber k (km^{-1}) to wavelength. The red curves refer to the *uncompansated* model. Dashed black, blue and magenta curves denote the transfer functions corresponding to elastic plate thickness T_e of 5, 15 and 30 km. Water depth is assumed to be $d = 2\ km$ for this illustration.

$S(x,y)$ to predict sea floor topography from downward continued gravity anomalies. This is the inverse of Nettleton's procedure and denoted as inverse Nettleton procedure (*Smith and Sandwell*, 1994).

Chapter 6

Data sources

Several global bathymetry models of the oceans have been developed, namely the General Bathymetric Chart of the Oceans (GEBCO, latest version GEBCO_2014, *Weatherall et al.* (2015)), Refined Topography data set (RTopo, latest version RTopo-2, *Schaffer et al.* (2016)), the new global topography SRTM30_PLUS (*Becker et al.*, 2009). GEBCO_2014 and SRTM30_PLUS are briefly described in Section 3.3. The global models are combinations of different data sources dedicated for Arctic, Antarctic and general oceans. RTopo-2 includes new regional data sets released recently, e.g., the Greenland continental shelf and fjords (*Arndt et al.*, 2015; *Bamber et al.*, 2013) and the edges of Antarctic ice shelf (*Le Brocq et al.*, 2010). All the global models partially or fully integrate the International Bathymetric Chart of the Arctic Ocean (IBCAO) (*Jakobsson et al.*, 2000, 2008, 2012) to achieve complete coverage in the Arctic regions.

However, the Arctic Ocean bathymetry is not well surveyed due to the presence of sea ice and harsh climate in the polar region. There were campaigns to map the sea floor topography through ship sounding, but it only covers a small fraction of the entire Arctic (*Mayer et al.*, 2012, 2016, 2010).

The global bathymetry models predicted from altimetric gravity only go upto latitude 80.75° (*Becker et al.*, 2009) and bathymetry beyond that latitude has not been tried.

As shown in Section 5.2, the gravity and topography show a linear relationship in a limited band of wavelengths. *Smith and Sandwell* (1994) suggested the wavelengths to be between 15 and 160 km in a study carried out in the southern oceans. In these wavelengths, we may expect a good correlation between gravity and topography. With improved marine gravity of the Arctic Ocean, Arctic bathymetry can be predicted from gravity using the relationship between gravity and topography.

In the following sections, the existing bathymetry map of the Arctic Ocean and DTU17 marine gravity will be introduced.

6.1 Arctic bathymetry

The existing bathymetry map IBCAOv3 is a compilation of multi-beam, single beam, Olex seabed mapping system and digital contour maps with a grid spacing of 500 m (Polar Stereographic projection, with true latitude at 75°) and reveals detailed features on the sea floor. The bathymetry grid nodes are well constrained when the sounding data is available. However, the areas with no soundings are interpolated to fill the gaps, see *Jakobsson et al.* (2012) auxiliary material.

The most recent release of IBCAO (Version 3.0, IBCAOv3; *Jakobsson et al.* (2012)) is shown in Figure 6.1, and its source identification grid is shown in Figure 6.2. Apparently, the number of grid cells filled by old digital contour maps dominates due to the lack of ship soundings.

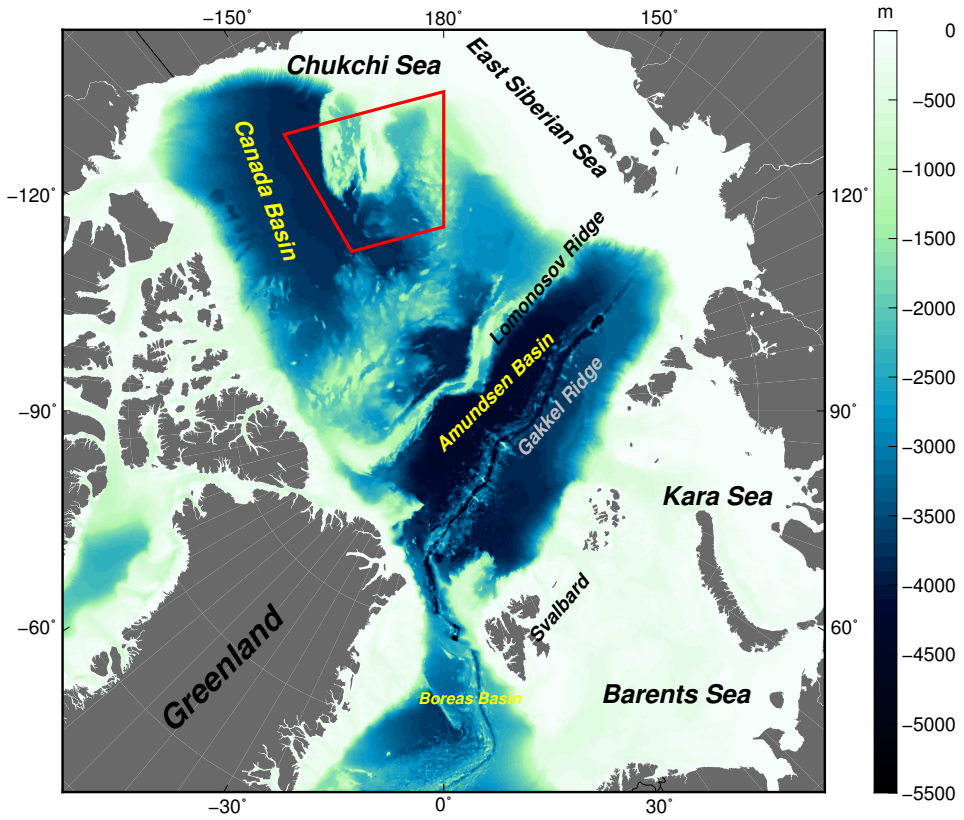

Figure 6.1: The Arctic bathymetry, IBCAOv3. The area bounded by the red box is Chukchi Cap (plateau).

As seen from Figure 6.1, most part of the Arctic Ocean, such as the East Siberian sea, Chukchi sea, Kara sea and Barents sea, are very shallow, with average depth ranging from 50 m to 230 m. Sea floor at these shallow water regions are relatively flat and have steep topographic variations at the margins to the major basins (e.g., Canada basin). The Chukchi Cap extends from the north of Alaska towards the Arctic Ocean and has been the region of interest in understanding the maritime law of Arctic Ocean (*Mayer et al.*, 2012, 2016, 2010). The thickness of sediments (*Døssing et al.*, 2014; *Laske*, 1997) in the deep Amundsen basin is approximately two kilometers, while it is up to 11 km in the Canada basin (*May and Grantz*, 1990). The sedimentary basins appear nearly flat on the bathymetry maps. The IBCAOv3

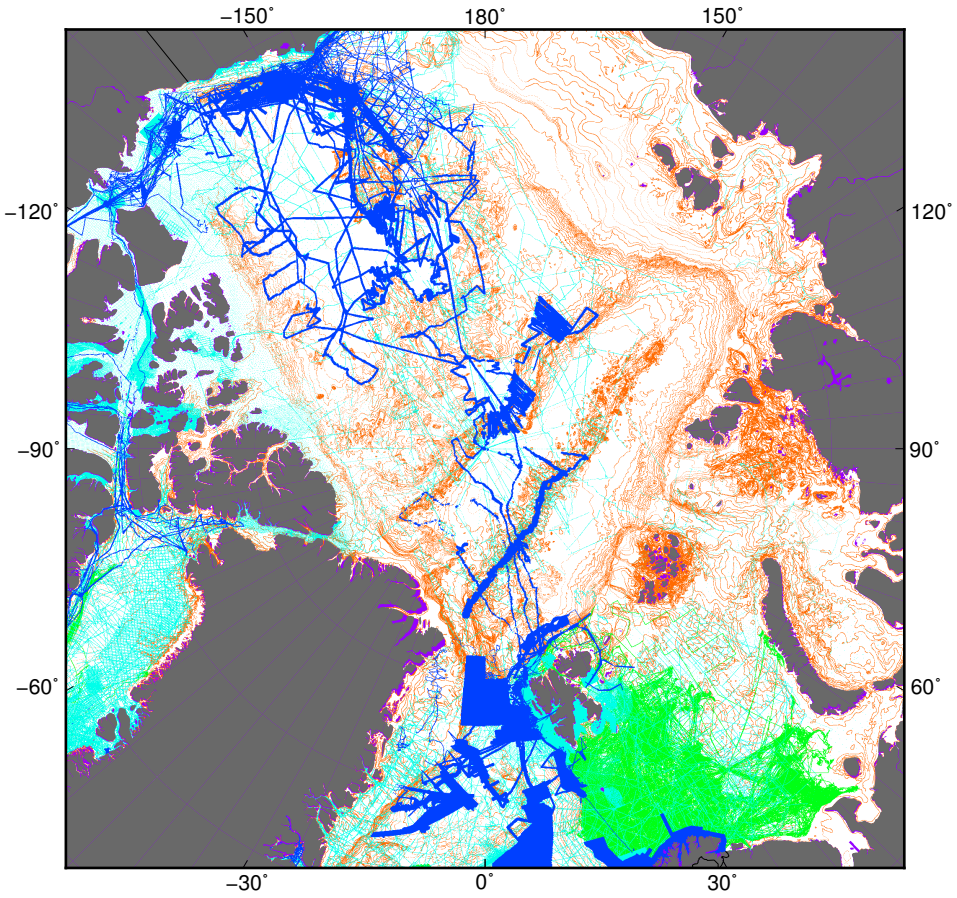

Figure 6.2: Source IDentification (SID) grid of IBCAOv3, implying the type of data source on a grid spacing of 2 km. *Purple* color indicates data from land Digital Elevation model (DEM), *blue* indicates data from multi-beam data, *cyan* indicates single beam data, *green* indicates data from Olex (`www.olex.no`), and *orange* indicates depth contours from digitized charts dating back to 1991, see *Jakobsson et al.* (2012) for details. The non-ocean cells are presented in gray.

serves as the reference bathymetry for our prediction. It is also denoted as "input bathymetry" in the next chapter.

6.2 Arctic gravity anomalies

The altimetric gravity model developed at DTU Space includes the 25 years of satellite altimetry data over the ocean. Between 70°N and 81.5°N, the ERS-1/2, EnviSat,

7 years of CryoSat-2 altimetry data and 1 year of SARAL/AltiKa data from geodetic phase is used; between 81.5°N to 88°N, only CryoSat-2 data is used; the remaining polar gap is filled by the ArcGP gravity compilations (*Kenyon et al.*, 2008). The DTU17 gravity anomalies in the Arctic ocean are shown in Figure 6.3. The accuracy of the DTU models have been improving dramatically in the Arctic ocean since the launch of CryoSat-2 in 2010. When compared to the LOMGRAV-09 aero-geophysical survey north of Greenland between 80°N to 88°N (Figure 6.4), the accuracy is improved from 9.82 mGal (relative to EGM08) to 3.87 mGal as of DTU17 model (see Table 6.1) . The huge improvement in the Arctic motivated us to invert the bathymetry from gravity. The geographic grid of DTU17 is co-registered to IBCAOv3 bathymetry grid using Polar Stereographic projection.

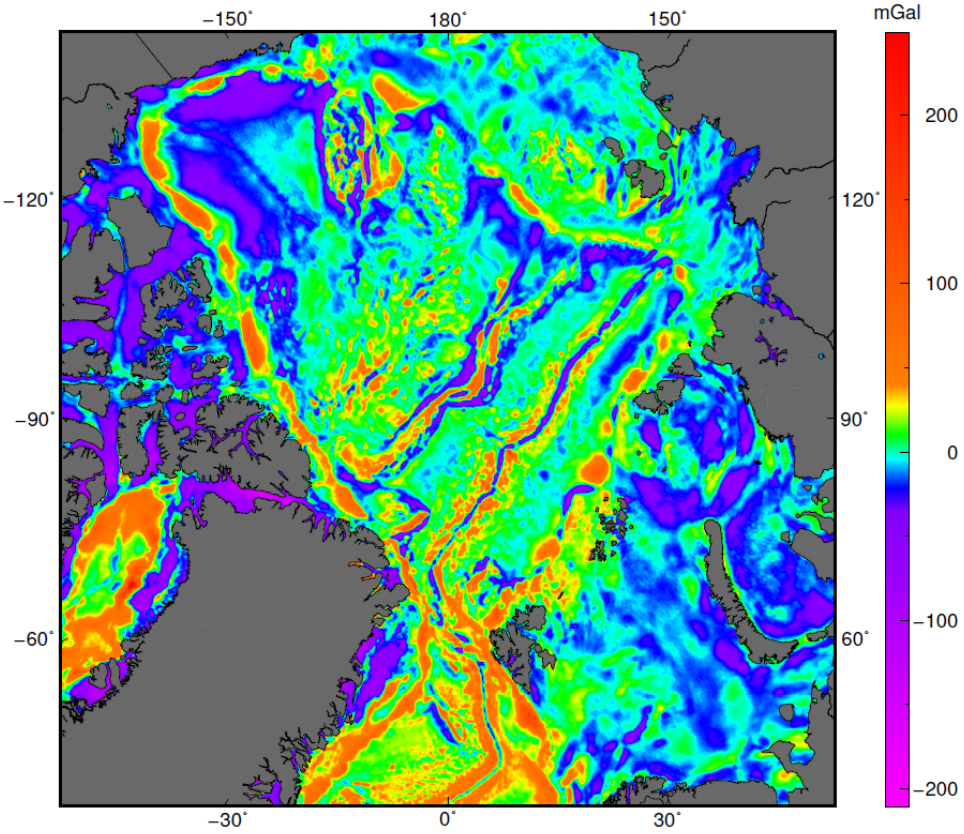

Figure 6.3: DTU17 gravity anomalies in the Arctic ocean.

Table 6.1: The accuracy of gravity anomalies (DTU models and EGM08) in the Arctic when validated with LOMGRAV-09 airborne gravity measurements. Unit: mGal.

Models	EGM08	DTU10	DTU15	DTU17
LOMGRAV-09	**9.82**	8.78	5.56	**3.87**

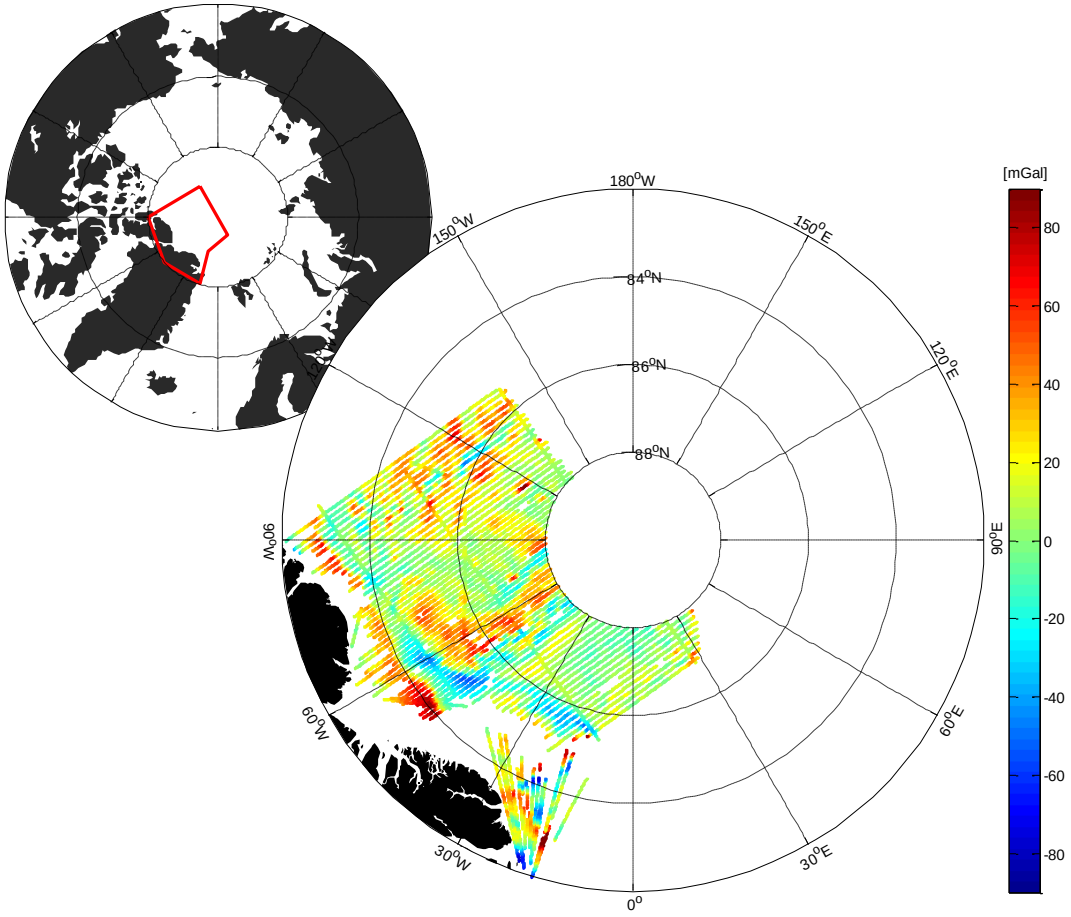

Figure 6.4: LOMGRAV-09 aero-geophysical survey conducted in 2009 at the north of Greenland. The final gravity dataset has 210 crossover points between the survey lines with an RMS of 2.4 mGal, implying 1.7 mGal noise level on the measurements (*Døssing et al.*, 2013; *Olesen and Forsberg*, 2007).

The accuracy of long wavelength (greater than 100 km) gravity field in the Arctic is slightly poorer than that in the mid-latitudes. The long wavelength signal in the DTU gravity model is from the Earth Gravitational Model 2008 (EGM08;

Pavlis et al. (2012)), in which the primary data source in the Arctic is from the Arctic Gravity Project (ArcGP; *Kenyon et al.* (2008)), see Figure 6.5a. As much as 5 mGal difference is observed on the long wavelength gravity field, when the ArcGP gravity anomalies are compared to GOCO05S satellite-only gravity model (*Mayer-Gürr et al.*, 2015). The differences are partly attributed to the patched gravity data from multiple sources in the ArcGP. Moreover, the differences at higher latitudes (>80°) are significant (*Pail et al.*, 2018). If not filtered properly, these could be translated into bathymetry prediction error.

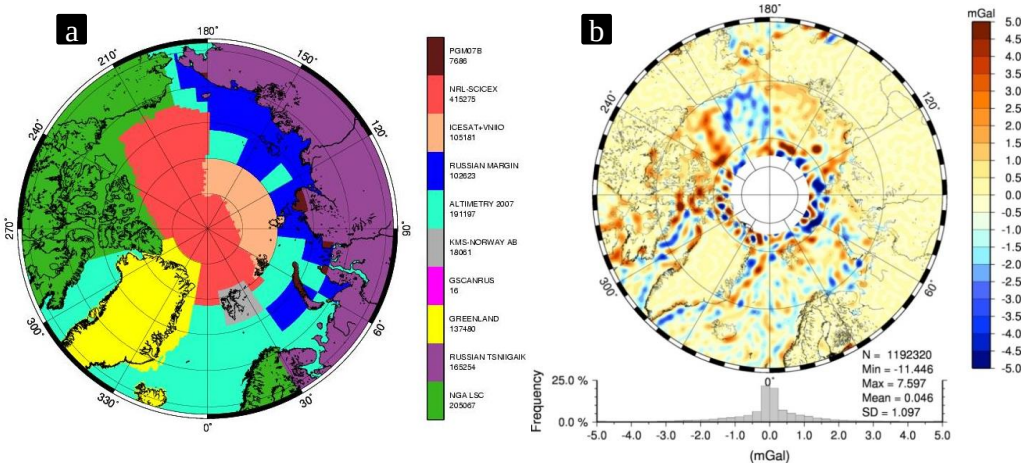

Figure 6.5: (a) the data sources (patches) used in the ArcGP project (*Kenyon et al.*, 2008); **(b)** The difference of ArcGP gravity field (EGM08) and combined satellite-only gravity model GOCO05S up to degree and order 200 (corresponding half-wavelength 100 km). Courtesy of Simon Holmes.

6.3 Land mask

The objective of this study is limited to the ocean bathymetry prediction. Therefore, we need a land mask to constrain the analysis to the grid points over the oceans only. The Global Self-consistent, Hierarchical, High-resolution Geography (GSHHG) Database (*Wessel and Smith*, 1996) coastlines (Version 2.3.4) assembled in the Generic Mapping Tool (GMT; *Wessel and Smith* (1991); *Wessel et al.* (2013)) are imported and co-registered with the bathymetry grid using Polar Stereographic projection.

Chapter 7

Arctic bathymetry prediction from gravity anomalies

This chapter includes the methodology to predict Arctic bathymetry from gravity anomalies and subsequent results and validations. The band-pass filtering functions are described in Section 7.1. The application of filtering functions to the bathymetry and gravity grids are explained in Section 7.2. The scaling factor estimation methods are outlined Section 7.3. The results and validations are presented in detail in Section 7.4 and 7.5. This chapter is concluded with a summary addressing the findings.

7.1 Filtering function

To predict the Arctic bathymetry from gravity, we need to design a band-pass filter to obtain the band-pass filtered version of input bathymetry (IBCAOv3) and gravity anomaly grid. The input bathymetry mainly provides the long and short

wavelength features (resolved by ship soundings) for the predicted bathymetry.

The predicted bathymetry $H_p(x,y)$ can be written as the sum of the long wavelength component of the input bathymetry $B_{long}(x,y)$, inverted topography from band-pass filtered gravity $G_{BP}(x,y)$ and remaining short-wavelength components from the high-pass filter of the input bathymetry $B_{short}(x,y)$, as below

$$H_p(x,y) = B_{long}(x,y) + \boldsymbol{S(x,y)} \cdot G_{BP}(x,y) + B_{short}(x,y), \tag{7.1}$$

where $\boldsymbol{S(x,y)}$ denotes the gravity-to-topography inversion parameter with unit m/mGal, which is referred as the *scaling factor* in the text below.

7.1.1 The Smith&Sandwell filter

The band-pass filtering function proposed by *Smith and Sandwell* (1994), denoted as the S&S filter, is

$$W(k) = W_1(k) \cdot W_2(k) \cdot exp[2\pi kd], \tag{7.2}$$

where $W_1(k)$ is a high-pass filtering function, $W_2(k)$ is a low-pass filtering function, the exponential term is the downward continuation operator, which is a function of depth d, k is the wavenumber $1/\lambda$ with unit km^{-1}, λ is the wavelength in km.

The high pass filtering function $W_1(k)$ is approximated by a Gaussian filter in *Smith and Sandwell* (1994). The original form of $W_1(k)$ is a function of crustal thickness c and the flexural wavelength of the elastic plate λ_0, taking the form

$$W_1(k) = 1 - exp[-2\pi kc] \cdot \left[1 + (\lambda_0 k)^4\right]^{-1}. \tag{7.3}$$

Recall the transfer function of the *compensated* model in Eq.(5.8) and $W_1(k)$ is ex-

actly the term in the brackets. The high-pass filtering function has an effect of suppressing the long wavelength components. In this study, the flexural wavelength was assumed to be $\lambda_0 = 135$ km, corresponding to elastic plate thickness $T_e = 5$ km. With the fixed value of λ_0, $W_1(k)$ changes slightly for different values of crust thickness as shown in Figure 7.1. For crustal thickness of c =8, 16, and 24 km, the admittance $W_1(k) = 0.5$ is observed where the cut-off wavelength is 163.0, 199.7 and 247.7 km, respectively. For the Arctic region, the thickness of crust is assumed to be 7 km, which yields cut-off wavelength of 160 km. The high-pass filtering function parameters mentioned above are identical to *Smith and Sandwell* (1994) and also unchanged in recent bathymetry model development (personal communication with Professor Sandwell).

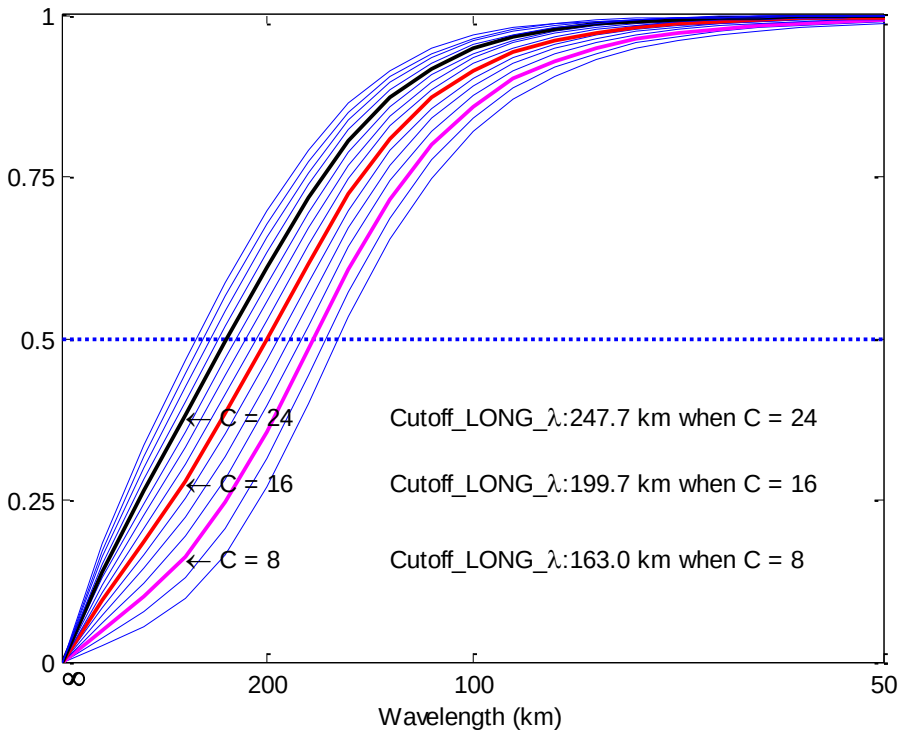

Figure 7.1: The high-pass filtering function $W_1(k)$ as a function of thickness of crust. The wavenumber k is transformed to wavelength at the horizontal axis.

The low-pass filter $W_2(k)$ was designed to suppress the noise at the short wavelengths. The filter depends on the regional water depth d, because the gravity signal decays at a rate depending on depth (*Smith and Sandwell*, 1994). The form of $W_2(k)$ is

$$W_2(k) = \left\{1 + \boldsymbol{A} \cdot k^4 \, exp[4\pi k d]\right\}^{-1}, \tag{7.4}$$

where $\boldsymbol{A}$ is a constant chosen to fit the spectral coherency between gravity and bathymetry. Note that the low-pass filtering function $W_2(k)$ is depth dependent. As shown in Figure 7.2, at a fixed depth $d = 4$ km, the cut-off wavelength shift towards the longer wavelength direction with higher values of $\boldsymbol{A}$, thus, suppressing more of the gravity signal at the short wavelengths. In this study, we use the value $A = 6233$ km^4 (same as in the Sandwell global topography V14.1[1]) which yields 13.5, 18.0 and 20 km admittance wavelength at water depth 2, 4 and 6 km.

7.1.2 Modified Smith&Sandwell filter

We addressed the long wavelength problem in the Arctic gravity anomalies in Section 6.2. If the long wavelengths error (appear as regional biases) is not filtered properly, it may translate into the error in the predicted bathymetry. Therefore, we propose a modified version of S&S filter, which completely suppresses the wavelengths longer than 100 km.

Gaussian filter, cosine-tapered filter, boxcar filter are three well-known filtering functions in signal processing. A Gaussian filter can be designed by setting a specific cut-off wavelength $\lambda_{cut} = 100$ km. However, longer (>100 km) wavelength features still remain after applying Gaussian filter. A boxcar filter can be designed by specifying the cut-off wavelength. In frequency domain, a boxcar filter can be

[1] ftp://topex.ucsd.edu/pub/global_topo_1min/

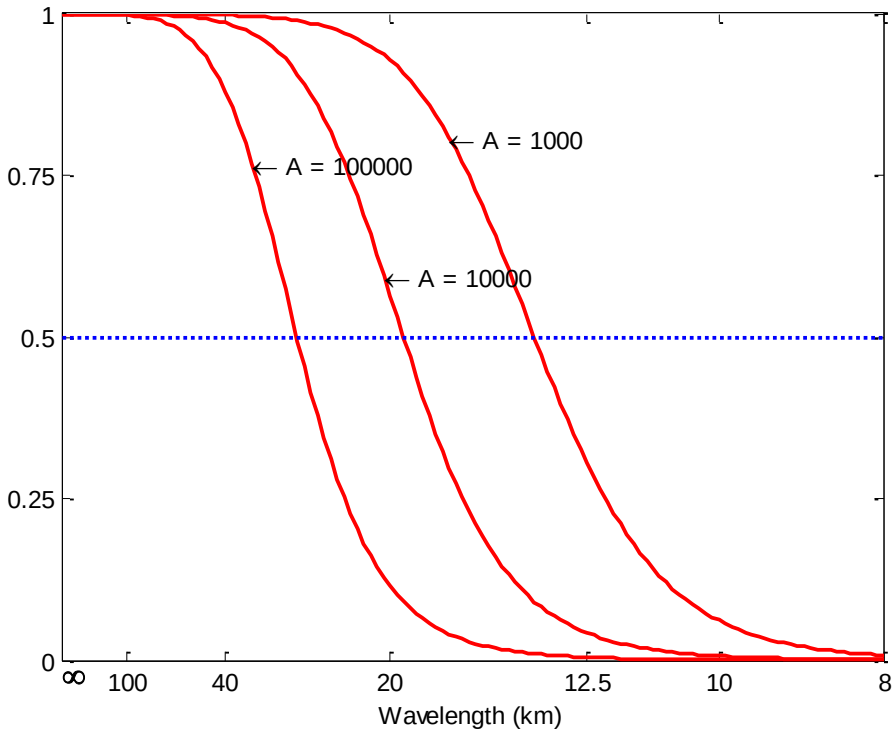

Figure 7.2: The low-pass filtering function $W_2(k)$ in Eq.(7.4) with experimental values of $\boldsymbol{A}$ being 10^3, 10^4 and 10^5 km^4 for a fixed depth $d = 4$ km. The wavenumber k is transformed to wavelength at the horizontal axis.

obtained by setting wavenumbers smaller than $1/\lambda_{cut}$ to 0 and the rest to 1. The problem with boxcar filter is that it introduces unnecessary "jitter" in the spatial structures. A cosine-tapered filter can be designed by specifying the cutting wavelength and passing wavelength. Realizing the problems with Gaussian and boxcar functions, we propose a cosine-tapered high-pass filter that resembles the shape (meaning similar slope) of high-pass filtering function $W_1(k)$, but completely suppressing wavelength longer than 100 km.

In the modified S&S filter, a cosine-tapered function $W_c(k)$ replaces the high-pass filter $W_1(k)$ to cut-off the wavelengths greater than 100 km and pass the wave-

length shorter than 40 km. The form of the cosine-taper function is

$$W_c(k) = \frac{1}{2} \times \left[1 + \cos\left(\pi \cdot \frac{k - k_p}{k_c - k_p}\right)\right], \tag{7.5}$$

where k_c denotes the cutting wavelength in wavenumber ($1/100$ km^{-1}) and k_p denotes the passing wavelength in wavenumber ($1/40$ km^{-1}). Thus, the admittance wavelength for the high-pass filter W_c is 57 km, whereas it is 160 km for the W_1 filter.

In the short form, the modified S&S filter $W_m(k)$ proposed here is given by

$$W_m(k) = W_c(k) \cdot W_2(k) \cdot exp[2\pi kd]. \tag{7.6}$$

The S&S filter $W(k)$ and modified S&S filter $W_m(k)$ without exponential terms are shown in Figure 7.3. Note that the low-pass filtering function $W_2(k)$ remains the same in both Eq.(7.2) and (7.6).

7.2 Filtered bathymetry and gravity

The long wavelength of the bathymetry is obtained by the low-pass filtering as below,

$$\boldsymbol{B}_{long}(k) = B(k)[1 - W_*(k)], \tag{7.7}$$

where $B(k)$ is the 2-D Fourier transform of the input bathymetry (IBCAOv3) $B(x,y)$, $k = \sqrt{k_x^2 + k_y^2}$ with $k_x = 1/\lambda_x$, $k_y = 1/\lambda_y$, λ_x and λ_y denotes the wavelength in X and Y directions. $W_*(k)$ is either $W_1(k)$ in Eq.(7.3) or $W_c(k)$ in Eq.(7.5).

The short wavelength features of the bathymetry mainly come from the ship sounding data that are integrated to the input bathymetry. It can be obtained by

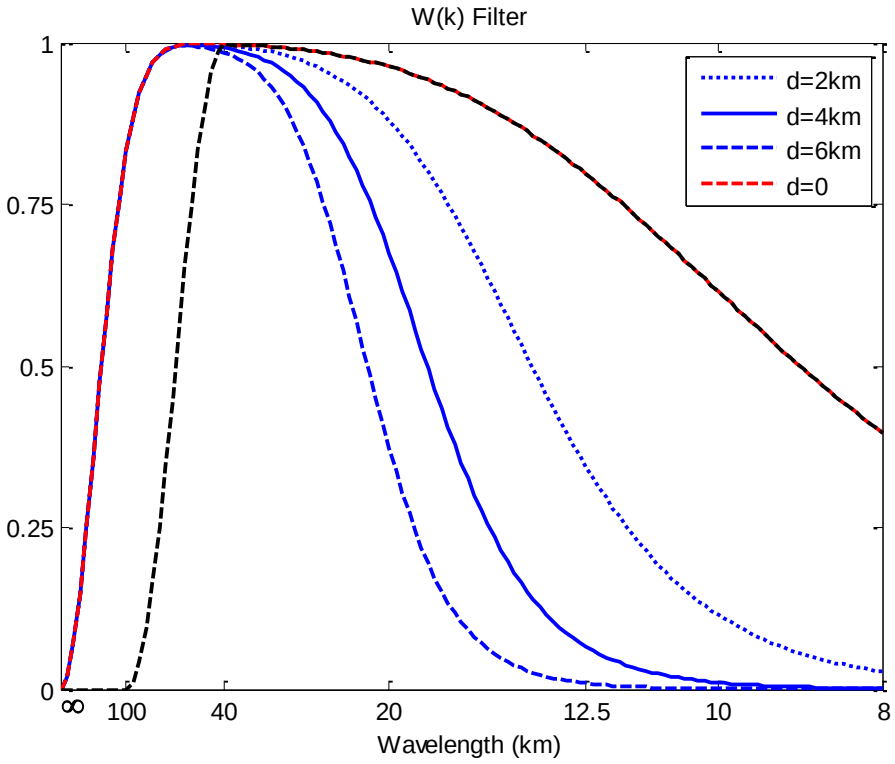

Figure 7.3: The S&S filter $W(k) = W_1(k)W_2(k)$ without exponential term at different depths d are shown in blue color. Modified S&S filter $W_m(k)$ with $d = 0$ is displayed by the black dashed curve. The horizontal axis is converted from wavenumber k to wavelength.

high-pass filtering as below,

$$\boldsymbol{B}_{short}(k) = B(k)[1 - W_2(k)]_{d=0}, \tag{7.8}$$

where the subscript $d = 0$ denotes that the function $W_2(k)$ should be evaluated with $d = 0$, meaning on the sea floor.

Moreover, the band-pass filtered bathymetry $\boldsymbol{B}_{BP}(k)$ is obtained by applying the S&S filter or its modified version with $d = 0$ (refer to the dashed red and black curves in Figure 7.3). After applying the inverse Fourier transform, the sum of the $B_{long}(x,y)$, $B_{bp}(x,y)$ and $B_{short}(x,y)$ yields the exact input bathymetry IBCAOv3. In

this way, we can examine if the filtering function is working properly.

The band-pass filtered gravity $G_{bp}(x,y)$ can be obtained by applying the band-pass filter $W(k)$ or $W_m(k)$ directly to the 2-D Fourier transform of input gravity grid $G(x,y)$. Note that the low-pass filtering function $W_2(k)$ is a function of depth d. In practice, the marine gravity $G(x,y)$ is band-pass filtered and downward continued to constant depths ranging from 0 to 6 km with an increment of 0.5 km. Then, the $G_{bp}(x,y)$ value in each grid cell is obtained by linear interpolation between the "sandwich" grids using the depth from long wavelength bathymetry $B_{long}(x,y)$.

7.3 Scaling factor estimation

Predicting the bathymetry from gravity is a process determining the best fitting scaling factor $S(x,y)$ to predict sea floor topography from downward continued gravity anomalies.

Since the linear relation between gravity and topography is only valid in the uncompensated wavelength band, the scaling factor $S(x,y)$ is determined using band-pass filtered bathymetry $B_{bp}(x,y)$ and band-pass filtered, downward continued gravity anomalies $G_{bp}(x,y)$. In the simple form,

$$B_{bp}(x,y) = S(x,y) \cdot G_{bp}(x,y). \tag{7.9}$$

In the previous section, we obtained the grids of $B_{bp}(x,y)$ and $G_{bp}(x,y)$. It is not feasible to derive a robust estimate of $S(x,y)$ for every grid node. In practice, one local scaling factor is estimated using (bathymetry and gravity) data pairs within certain radius from the estimation point. The grid spacing between the local estimates is chosen to be 30 km which is much larger than the 500 m grid spacing

of input grids. Then, the local estimates are tiled together and gridded to a dense $S(x,y)$ grid (500 m grid spacing) that can be directly multiplied with band-pass filtered gravity $G_{bp}(x,y)$. In the following, we describe the prediction method for the local estimates of scaling factor.

7.3.1 Slope estimator

In the Eq.(7.9), $S(x,y)$ is actually the slope of the line fitting the data pairs. Such slope estimates can be achieved by first order least squares fitting (LSF). However, if there are errors in G_{bp} and B_{bp} pairs, the slope estimates from least square fitting can be biased.

Considering the non-Gaussian distribution of data, *Smith and Sandwell* (1994) suggested to estimate the scaling factor $S(x,y)$ with the Median Absolute Deviation (MAD) of the data pairs as follows,

$$\hat{S} = \pm \frac{b_{MAD}}{g_{MAD}}, \tag{7.10}$$

where the $\pm$ sign is to denote the positive or negative correlation between the gravity and bathymetry. The exact sign is taken from the linear correlation coefficient between B_{bp} and G_{bp} pairs.

The linear correlation coefficient refers to the Pearson correlation coefficient (also known as *Pearson's r*). For the data pairs, the Pearson correlation coefficient, denoted as ϱ, is estimated by the variance (σ_b^2 and σ_g^2) and co-variance $\mathrm{Cov}(b,g)$ of the two data pairs,

$$\varrho = \frac{\mathrm{Cov}(b,g)}{\sqrt{\sigma_b^2} \cdot \sqrt{\sigma_g^2}}. \tag{7.11}$$

The correlation coefficient ϱ has a value between -1 and $+1$. Values greater

than 0.5 mean significant correlation between band-pass filtered bathymetry and gravity. The low (<0.5) values mean insignificant correlation.

7.3.2 Random Sample Consensus

Alternative to the slope estimator using the MAD values of data pairs in Eq.(7.10), the RANdom SAmple Consensus (RANSAC, *Fischler and Bolles* (1981)) can be used as a robust estimator of $\hat{S}$.

The RANSAC algorithm was initially proposed to image analysis applications. The algorithm can also be adapted to fit a line as an alternative to the LSF. In the LSF, all data, despite the few data containing gross errors, is used to achieve the best fitting model. The RANSAC algorithm is also capable of fitting a model (line) to data containing gross errors. In the case of RANSAC, only a proportion of the data that are assumed to be "consensus", are used to fit a model.

The data points are divided into *inliers* and *outliers* by randomly selecting a minimum set of the data and fit the model. For fitting a line, the minimum set is two. By examining the error tolerance, the selected data points are labelled as "inliers" and "outliers". The number of inliers are saved and a best (least square) fit is obtained from these inliers. Then, randomly select a new subset, and examine the number of inliers. After a sufficient number of iterations, all data points are randomly selected and the number of inliers are saved. In the end, the best fitting model is achieved by using the subset producing the maximum number of inliers.

The advantage of RANSAC algorithm is that it will try to maximise the number of inliers in the scattered data, and the outliers will not be considered for the slope estimation.

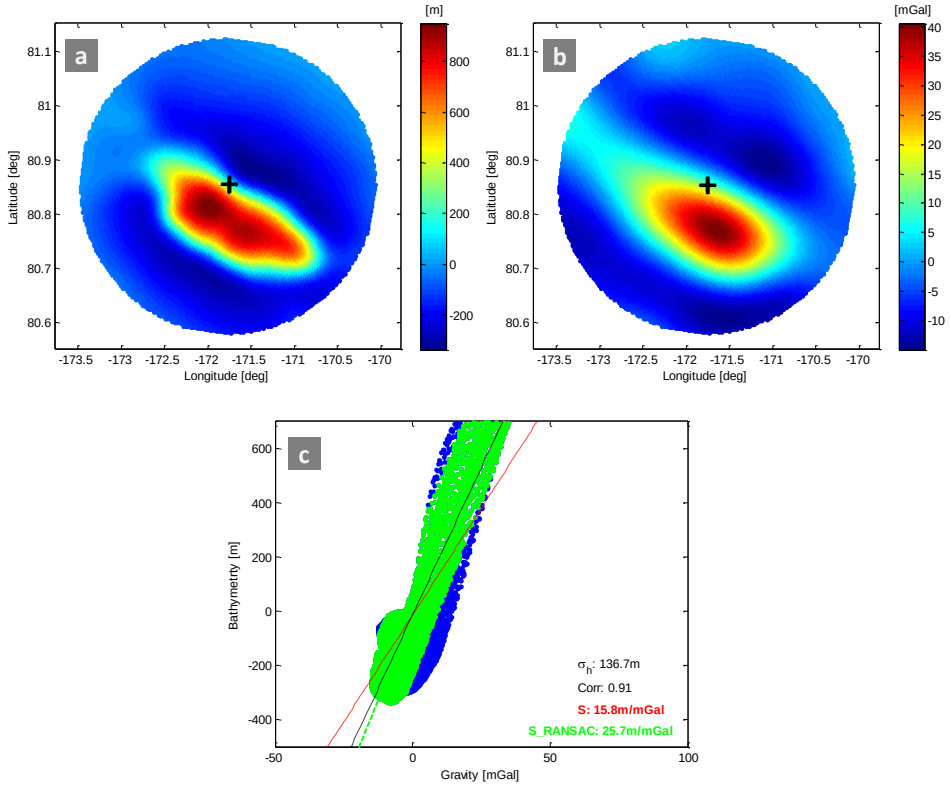

Figure 7.4: Scaling factor estimation in a 30 km radius cap over a *seamount*. Thick black + marker shows the center of the cap and it is the location of local scaling factor $\hat{S}$. (a) band-pass filtered bathymetry, (b) band-pass filtered gravity, (c) bathymetry versus gravity. Slope of the lines ($\hat{S}$) estimated using different algorithms. Red line for the slope estimator (Eq.(7.10)), green for the RANSAC estimator and black for the least square fitting. The scattered points for band-pass filtered bathymetry and gravity pairs are marked in blue, while the green RANSAC inliers are superimposed on them.

Open source code for RANSAC is available online[2] and easy to use. Note that the algorithm requires a large number of iterations and is computationally intensive.

Scaling factor estimation at two different locations are shown in Figure 7.4 and 7.5. At these two locations, bathymetry and gravity are significantly correlated (correlations coefficients 0.91 and 0.71). The radius of the caps is 30 km. One scaling

[2] https://github.com/RANSAC/RANSAC-Toolbox

parameter $\hat{S}$ is estimated at the center of 30 km radius cap which is marked by thick black plus marker in subfigure 7.4a and 7.5a. In subfigure 7.4c and 7.5c, blue dots denote the data pairs (bathymetry vs. gravity), while the green dots denote the RANSAC inliers. The slope of the dashed green line refers to the RANSAC estimate. The slope of the red line is estimated using the b_{MAD} and g_{MAD} of all blue samples. In addition, the best least square fitting (LSF) line is also shown in black. The three types of estimators give different values of $\hat{S}$. The estimated slope from LSF is close to RANSAC, but it could deviate dramatically from the RANSAC estimates when there are a number of outliers (left out by RANSAC algorithm), see subfigure 7.5c. Over the seamount as shown in subfigure 7.4a, a difference of 10 m/mGal in the scaling factor could produce a difference of 400 m. The RANSAC estimator tends to predict higher scaling factor $\hat{S}$ than the slope estimator in Eq.(7.10).

7.4 Results

In this section, we present the bathymetry prediction results using the S&S filter and modified S&S filter in the Arctic ocean.

The band-pass filtered bathymetry and DTU17 gravity anomalies after applying the S&S filter $W(k)$ and modified S&S filter $W_m(k)$ are shown in Figure 7.6 over the Chukchi Cap, which is bounded by the red box in Figure 6.1. It is evident that long wavelength features are remaining in the output from $W(k)$ filter, due to the 160 km cut-off wavelength.

The scaling factor $S(x,y)$ is estimated on a 30 km spacing grid nodes in the Polar stereographic projection system. On each $S(x,y)$ grid node, the band-pass filtered bathymetry and gravity data pairs within 30 km radius from the estimation point are used for the predicting one scale factor, along with the linear correlation

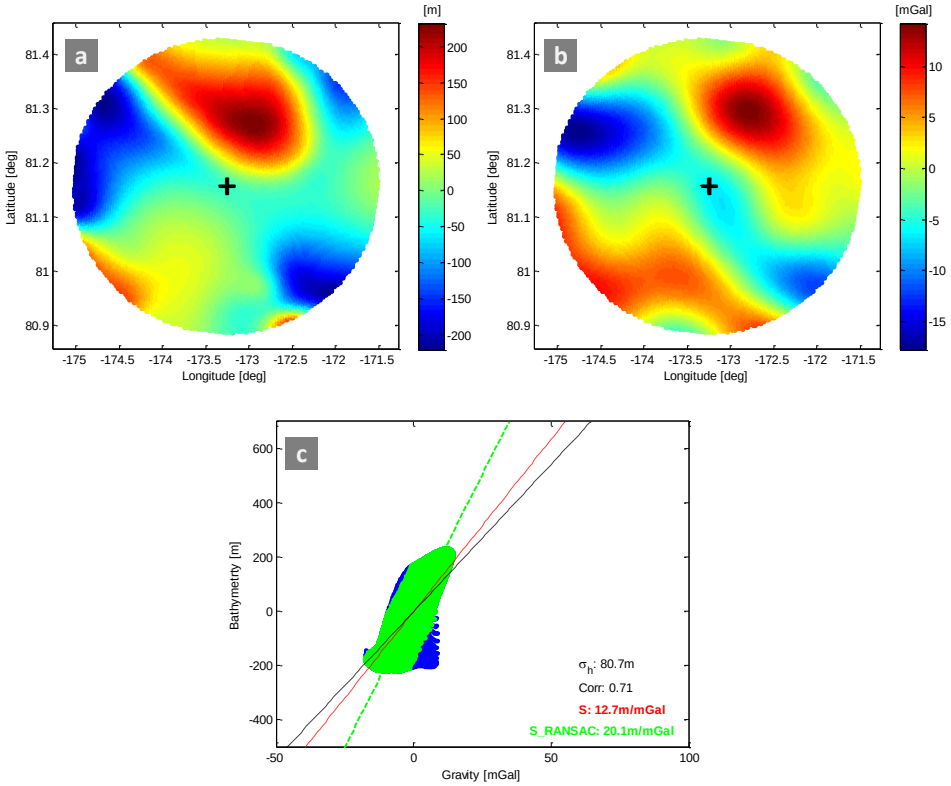

Figure 7.5: Scaling factor estimation in a 30 km radius cap over a region with moderate topographic variations. Thick black + marker shows the center of the cap and it is the location of local scaling factor $\hat{S}$. (a) band-pass filtered bathymetry, (b) band-pass filtered gravity, (c) bathymetry versus gravity. Slope of the lines ($\hat{S}$) estimated using different algorithms. Red line for the slope estimator (Eq.(7.10)), green for the RANSAC estimator and black for the least square fitting. The scattered points for band-pass filtered bathymetry and gravity pairs are marked in blue, while the green RANSAC inliers are superimposed on them.

coefficient. The scaling factor $S(x,y)$ and correlation coefficients for the entire Arctic are shown in Figure 7.7 and 7.8. The estimates are based on the band-pass filtered version of bathymetry and gravity using the modified S&S filter $W_m(k)$.

On most part of the shallow water regions in the Arctic ocean, both the correlation and scaling factor are low (or even negative). In such parts, we simply set $S(x,y) = 0$. Moderate correlation and scaling factor $S(x,y)$ are obtained over the Chukchi Cap, along the Gakkel Ridge, Lomonosov Ridge and as well as the north

Atlantic Boreas basin, see specific names on Figure 6.1. The topography is inverted from gravity in these regions.

We use a threshold of 0.5 on the correlation coefficients to filter out the grid nodes where the bathymetry and gravity are insignificantly correlated. The $S(x,y)$ grid nodes where the correlation coefficients are greater than 0.5, are shown in Figure 7.9. The ocean ridges and continental shelf margins are visible after screening out nodes with low correlation. Grid nodes at the sedimentary Canadian basin

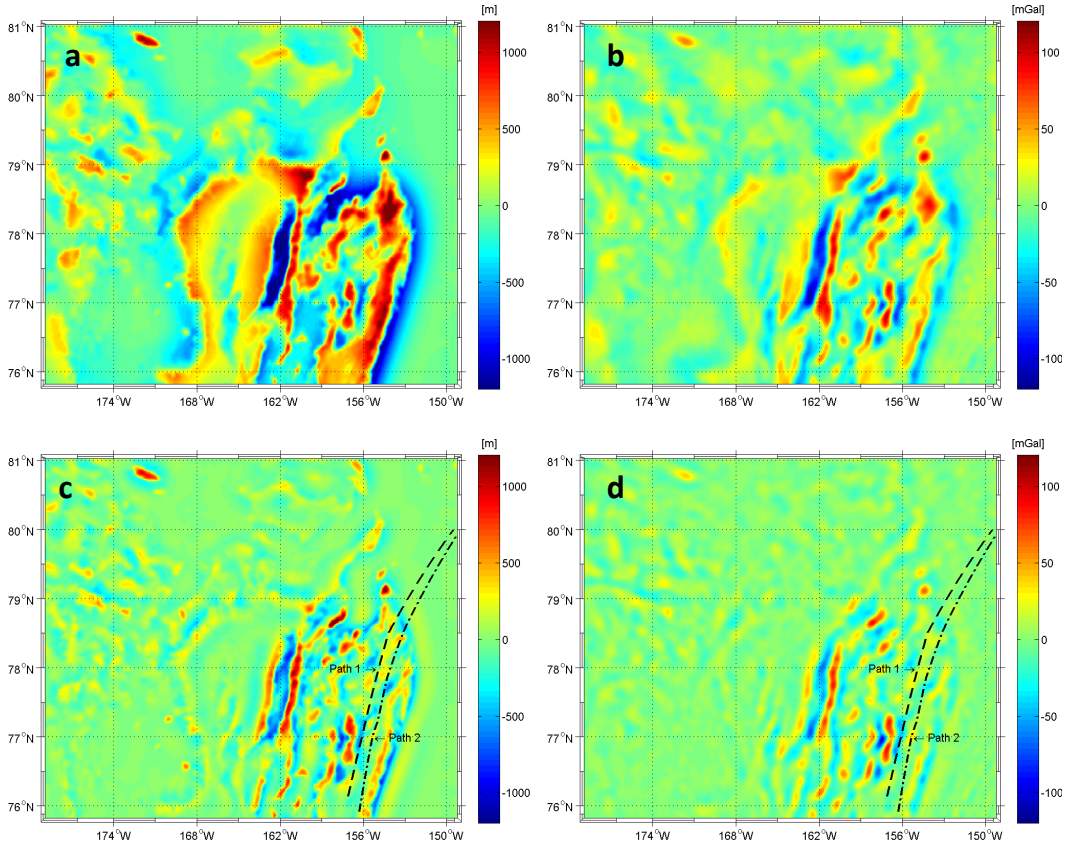

Figure 7.6: Band-pass filtered bathymetry **(a)** and gravity **(b)** when using S&S filter $W(k)$ from *Smith and Sandwell* (1994); Band-pass filtered bathymetry **(c)** and gravity **(d)** when using modified S&S filter $W_m(k)$ proposed in this thesis; two northbound Healy cruises from HE1603 crossing the Chukchi Cap (plateau) are shown by the dashed curve, which will be used for profile analysis later.

and Amundsen basin, along with shallow sea shelves around the Russian coast, are filtered out. To transform gravity to heights, the 30 km spacing $S(x,y)$ grid is interpolated (gridded to 500 m grid spacing), co-registered and multiplied with the band-pass filtered gravity grid $G_{BP}(x,y)$. This is performed by GMT *surface* module with a tension factor of 0.5 and *grdmath* grid operations.

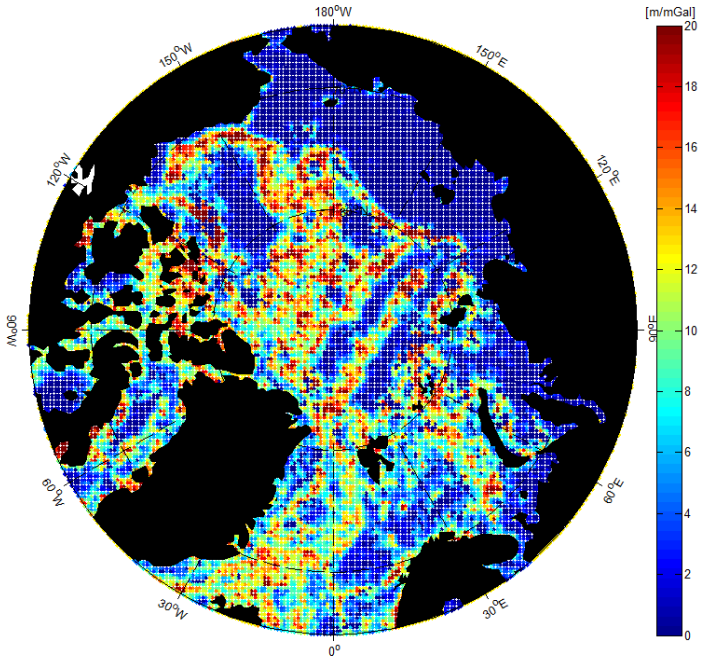

Figure 7.7: Scaling factor $S(x,y)$ estimated using the slope estimator method in Section 7.3.1 in the Arctic ocean. The grid spacing is 30 km. Negative values of $S(x,y)$ are displayed in deep blue.

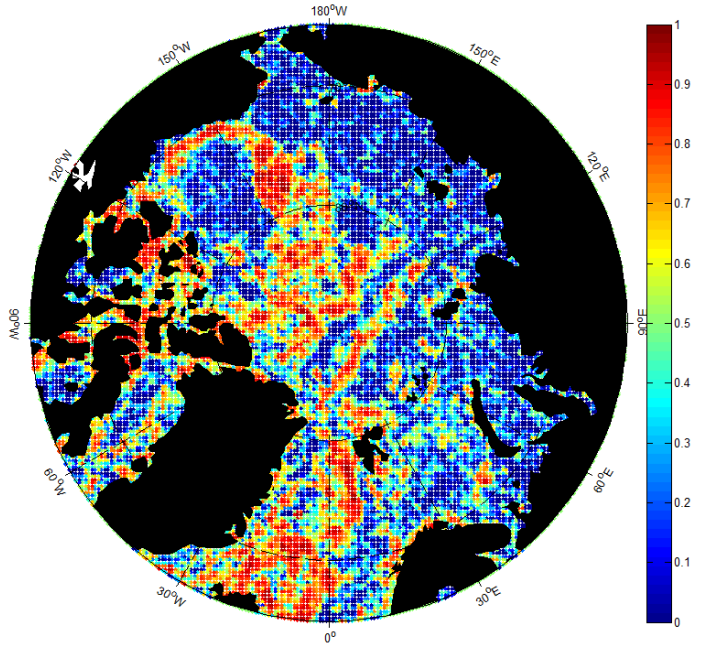

Figure 7.8: Correlation coefficients estimated at the location of scaling factor $S(x,y)$ grid nodes shown in Figure 7.7.

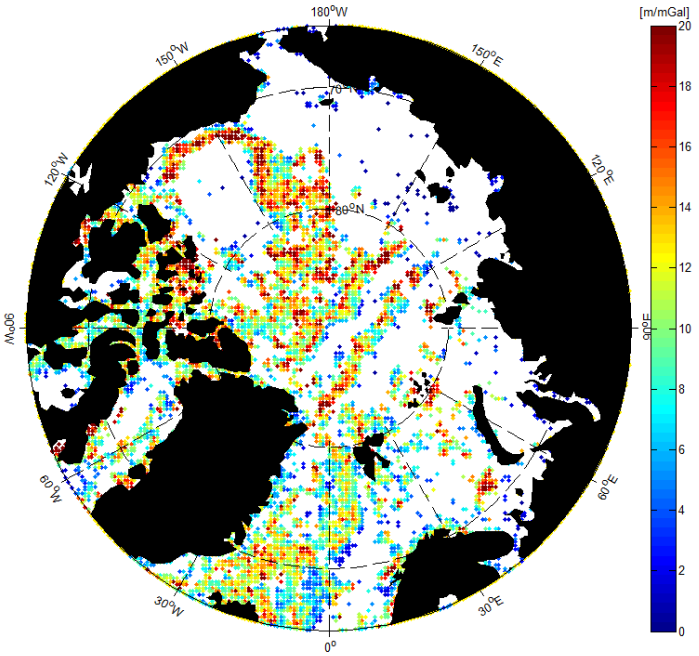

Figure 7.9: Scaling factor $S(x,y)$ grid nodes where the correlation coefficients are greater than 0.5.

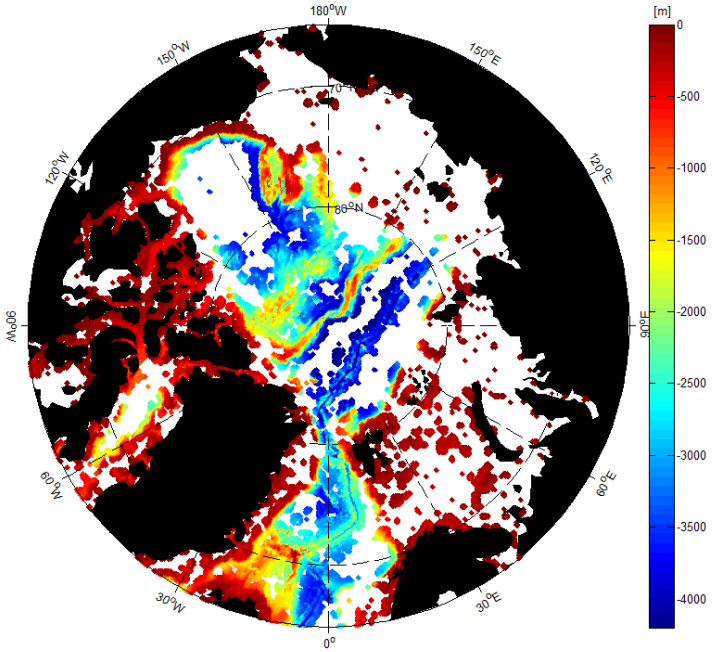

Figure 7.10: Predicted bathymetry $H_p(x,y)$ on regions where significant correlation is observed.

In the final step, the predicted bathymetry $H_p(x,y)$ can be obtained by adding the long and short wavelength bathymetry as shown in Eq.(7.1). In Figure 7.10, the predicted bathymetry $H_p(x,y)$ is shown on the regions where significant correlation between bathymetry and gravity are observed. The rest of the nodes are set to NaN values and later will be filled up with original IBCAOv3 bathymetry.

Subsequently, we perform a comparison between our prediction resulting from modified S&S filter $W_m(k)$ and the initial input bathymetry grids (IBCAOv3) on the same grid nodes. The differences are given in Figure 7.11. In particular, very large differences are observed at Gakklel ridge, which is located more than 3500 m below sea level. From the source identification grid in Figure 6.2, we can see that there are dense multi-beam surveys right along the ridge axis, which maps the detailed features of local seafloor. The cause of the differences can be attributed to the downward continued gravity to deep sea floor of approx. 4 km, which only has larger than 18 km features. Thus, in some wavelengths we don't predict bathymetry. Such large differences were also observed in the southern ocean studies from *Smith and Sandwell* (1994). Histogram of the differences (Figure 7.12) suggests long tailed distribution with a narrow peak at zero bin. When the data distribution implies non normal distribution, the Median Absolute Deviation (MAD) is a more robust parameter to measure the variability of the distribution. The mean difference is -0.5 m, the MAD and std. of the differences are 51.3 m and 81.5 m. On 85.8% of the grid nodes, the absolute differences are less than 100 m.

Table 7.1: The difference of predicted bathymetry $H_p(x,y)$ and IBCAOv3 using different filtering functions. Both grids have 500 m grid spacing and the number of grid nodes used for this evaluation is 29.8 million for S&S filter and 23.4 million for modified S&S filter. $|\triangle h|$ implies absolute difference and shows the percentage of grid nodes that are smaller than 100. Unit: m

Filter	$\lvert\triangle h\rvert < 100$	mean	MAD	std.	min	max
$W(k)$	64.8%	7.7	98.3	143.7	-1531.8	1862.2
$W_m(k)$	85.8%	-0.5	51.3	81.5	-782.9	1129.7

In addition, the comparison with bathymetry predicted using the S&S filter $W(k)$ and modified S&S filter $W_m(k)$ are given in Table 7.1. The predicted bathymetry from the S&S filter gives relatively large differences compared to the modified filter proposed in this study. This is also indicated by the histograms in Figure 7.12. Significant number of nodes with absolute differences $|\triangle h| > 250$ m are observed from the histogram (Figure 7.12a) referring to the S&S filter. The MAD of differences is almost two times larger than that of modified S&S filter. A mean difference of 7.7 m suggests that the predicted bathymetry from S&S filter is shallower than IBCAOv3. Note that the mean of differences are estimated from 29.8 million and 23.4 million samples. The mean and std. (or MAD) calculated from such a large number of samples don't reflect the regional differences over the ridges shown in Figure 7.11. Hence, we need to evaluate the predicted bathymetry in a smaller region with independent bathymetric surveys.

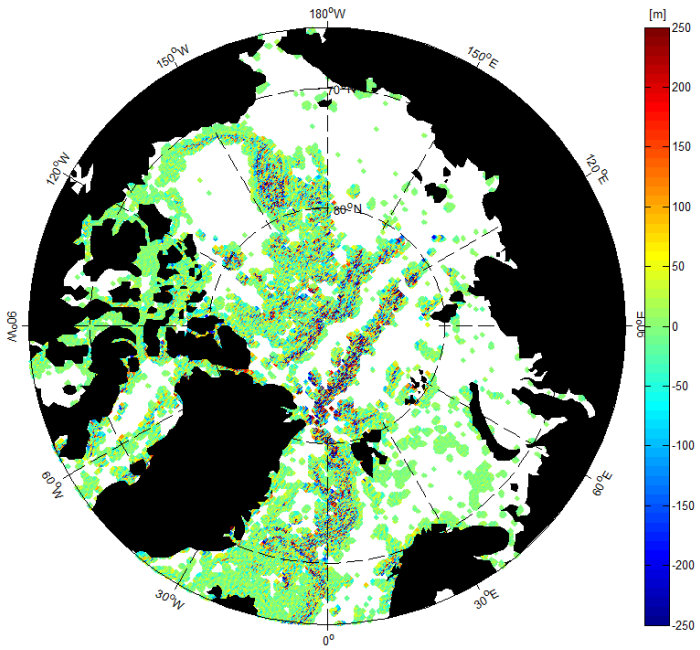

Figure 7.11: Difference of predicted bathymetry $H_p(x,y)$ and IBCAOv3 on regions where significant correlation is observed as in Figure 7.9.

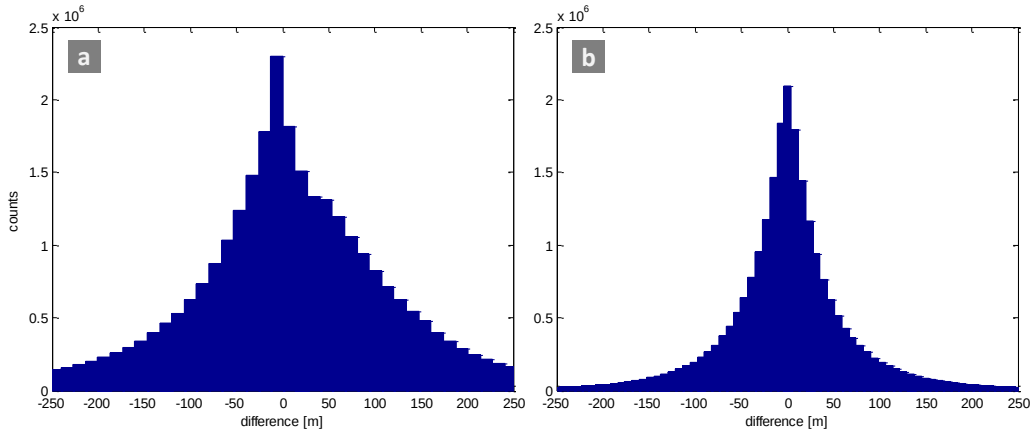

Figure 7.12: Histogram of the difference between predicted bathymetry and IBCAOv3. (a) bathymetry predicted using S&S filter subtract IBCAOv3, (b) bathymetry predicted using modified S&S filter subtract IBCAOv3, refer to Figure 7.11

.

7.5 Validation

The bathymetric sounding surveys can be accessed through NOAA National Centers for Environmental Information (NCEI, formerly NGDC) Bathymetry Data Viewer map services. There is a limited amount of ship soundings conducted after the release of IBCAOv3. Most of the ship sounding multibeam data is collected as part of Extended Continental Shelf (ECS) project and led by scientists from the University of New Hampshire and US Geological Survey. The target region of the ECS project is mainly around the Chukchi Cap and only a few cruise tracks are operated towards the North Pole (*Mayer et al.*, 2016, 2010). The differences of ECS compilation and IBCAOv3 give a mean of -11.4 m with a std. of 48.0 m. It is worth to mention that most of the cruises operated before 2012 have already been incorporated to IBCAOv3. Therefore, only several recent cruises are relatively independent for external validation, for instance HE1202 (*Mayer et al.*, 2012) and HE1603 (*Mayer et al.*, 2016).

A closer view on the differences of compiled ECS ship sounding compilations (from 2003 to 2016) and our bathymetry predictions to the north of Chukchi Cap is shown in Figure 7.13. Positive differences indicate that bathymetry inverted from gravity is deeper than ship sounding, and thus implies that the actual heights of seamount are underestimated (by as much as 400 m). Negative differences indicate that the bathymetry inverted from gravity is shallower than ship sounding by as much as 100 m (mainly over the deep relatively flat basins).

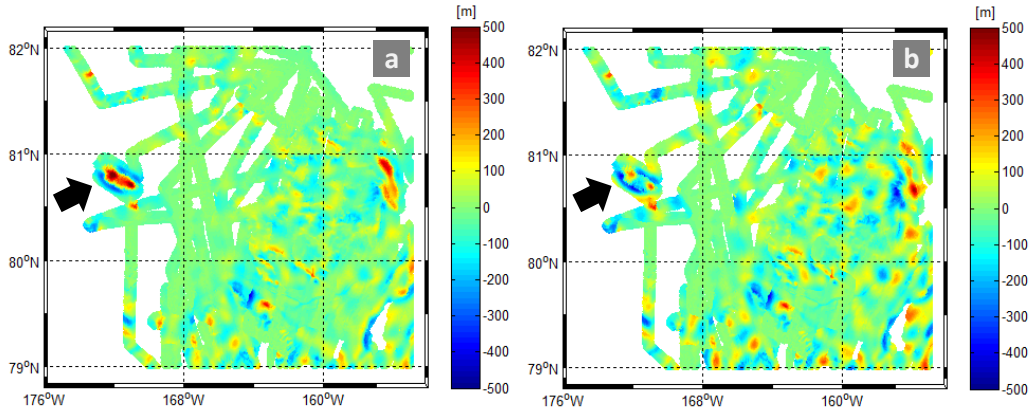

Figure 7.13: The difference of compiled ECS (multi-beam) bathymetry data and predicted bathymetry resulting from different scaling factor estimation algorithms on the north of Chukchi Cap. (a) Scaling factor estimated from slope estimator using MAD values of data pairs, (b) scaling factor estimated from RANSAC algorithm. Gravity and bathymetry were filtered with modified S&S filter $W_m(k)$. In total, 268105 multi-beam samples (500 m spacing) are used in this comparison.

In Figure 7.13, ECS bathymetry compilations are compared to bathymetry resulting from different scaling factor estimation algorithms described in Section 7.3. The results from slope estimators using MAD values appear smoother than the results obtained from RANSAC. RANSAC estimator performs better than the slope estimator over a seamount marked by the black arrow. In fact, this is exactly the spot we demonstrated the scaling factor estimation in Figure 7.4. On average, scaling factor estimated from RANSAC is 6.6 m/mGal higher than that estimated from slope estimator. Therefore, more fluctuations are visible on the results obtained

from RANSAC.

The mean difference between ECS bathymetry data and bathymetry resulting from slope estimator (refer to Figure 7.13a) is -11.6 m, with a std. of 71.7 m. It is -13.0±81.0 m for the differences referring to RANSAC in Figure 7.13b. One should be careful when employing RANSAC algorithm to entire region. We recommended to use RANSAC estimator over rugged topography with large variations.

In the following, two profiles taken from Healy cruise multi-beam sounding surveys conducted in 2016 (HE1603) are analysed. Location of the two profiles are shown in Figure 7.6. The two profiles are sampled approximately at the center beam locations of the multi-beam surveys. From south to north, the two paths cross the margin of Chukchi Cap (plateau) at the along track distance $\sim$ 300 km as shown in Figure 7.14. Along track profiles are obtained by interpolating on the predicted bathymetry and IBCAOv3 grids. The profiles referring to S&S filter are shown in Figure 7.14. In Figure 7.14, predicted bathymetry (black curve) deviates as much as 200 m from IBCAOv3 and HE1603 profiles over Chukchi plateau. Such deviations are evident on both profiles of path 1 and path 2. The profiles referring to the modified S&S filter are shown in Figure 7.15. Predicted bathymetry shows good agreement with HE1603 profiles as well as IBCAOv3. No dramatic deviations are observed on both path profiles. At the along track distance $\sim$ 200 km in subfigure 7.15a, the blue arrow indicates a spot where IBCAOv3 is problematic. At this spot, an approx. 1000 m deep valley was mapped in existing IBCAOv3. However, the ship soundings from HE1603 comply with the bathymetry inverted from gravity at this spot. The steep topography at the margin of Chukchi plateau is mapped in detail by multi-beam soundings. However, bathymetry predicted from gravity anomalies is not capable of resolving features indicated by red arrow in Figure 7.15a at the edge of Chukchi plateau.

The statistics of profile analysis referring to S&S filter in Figure 7.14 are shown in Table 7.2. The differences of predicted bathymetry and HE1603 soundings yield a mean deviation of 160.4 m for path 1 and 144.6 m for path 2. Note that HE1603 profile on path 2 agrees well (std.=54 m) with IBCAOv3, which, we believe, is an exact repeat of previous Healy cruise. On path 2, predicted bathymetry has mean difference of 144.6 m with 182.8 m standard deviation. The statistics imply severe misfit between the predicted bathymetry using S&S filter and independent Healy cruise ship soundings conducted in 2016.

Table 7.2: The statistics of the differences from profile analysis. Bathymetry prediction results from S&S filter $W(k)$. Unit: m

Profile	Difference	mean	std.	min	max
Path 1	HE1603 - $H_p(x,y)$	**160.4**	**195.7**	-134.1	731.2
	HE1603 - IBCAOv3	33.9	181.6	–295.8	1012.8
	$H_p(x,y)$ - IBCAOv3	-126.0	243.3	-636.0	677.3
Path 2	HE1603 - $H_p(x,y)$	**144.6**	**182.8**	-246.3	531.6
	HE1603 - IBCAOv3	2.3	54.1	-225.8	175.2
	$H_p(x,y)$ - IBCAOv3	-126.3	184.6	-514.6	233.8

Table 7.3: The statistics of the differences from profile analysis. Bathymetry prediction results from modified S&S filter $W_m(k)$. Unit: m

Profile	Difference	mean	std.	min	max
Path 1	HE1603 - $H_p(x,y)$	**50.8**	**119.5**	-211.9	413.8
	HE1603 - IBCAOv3	33.9	181.6	–295.8	1012.8
	$H_p(x,y)$ - IBCAOv3	-16.9	161.8	-438.6	694.0
Path 2	HE1603 - $H_p(x,y)$	**-36.9**	**77.6**	-237.4	202.6
	HE1603 - IBCAOv3	2.3	54.1	-225.8	175.2
	$H_p(x,y)$ - IBCAOv3	51.2	89.2	-233.4	285.5

The statistics of profile analysis referring to modified S&S filter in Figure 7.15 are shown in Table 7.3. In general, statistics are significantly improved compared to Table 7.2, meaning good agreement between predicted bathymetry (using modified S&S filter) and independent ship sounding. On path 1, standard deviation of differences between HE1603 and predicted bathymetry is 119.5 m, which is 39% improvement to the bathymetry using S&S filter on this profile. Moreover, the mean difference on path 1 is reduced from 160.4 m to 50.8 m. Smaller mean difference indicates consistency between predicted bathymetry and HE1603. On path 2, the mean difference is only -36.9 m with a std. of 77.6 m as shown in Table 7.3. Compared to a std. of 182.8 m from bathymetry using S&S filter, 57% improvement is obtained from bathymetry using modified S&S filter. In particular, the standard deviation of differences between HE1603 and IBCAOv3 on path 1 is 181.6 m. Differences between HE1603 and predicted bathymetry using modified S&S filter yield a std. of 119.5 m which is 33% improvement to the existing IBCAOv3.

The profile analysis and validation with independent ship soundings suggest the modified S&S filter is successful in predicting Arctic ocean bathymetry from gravity anomalies.

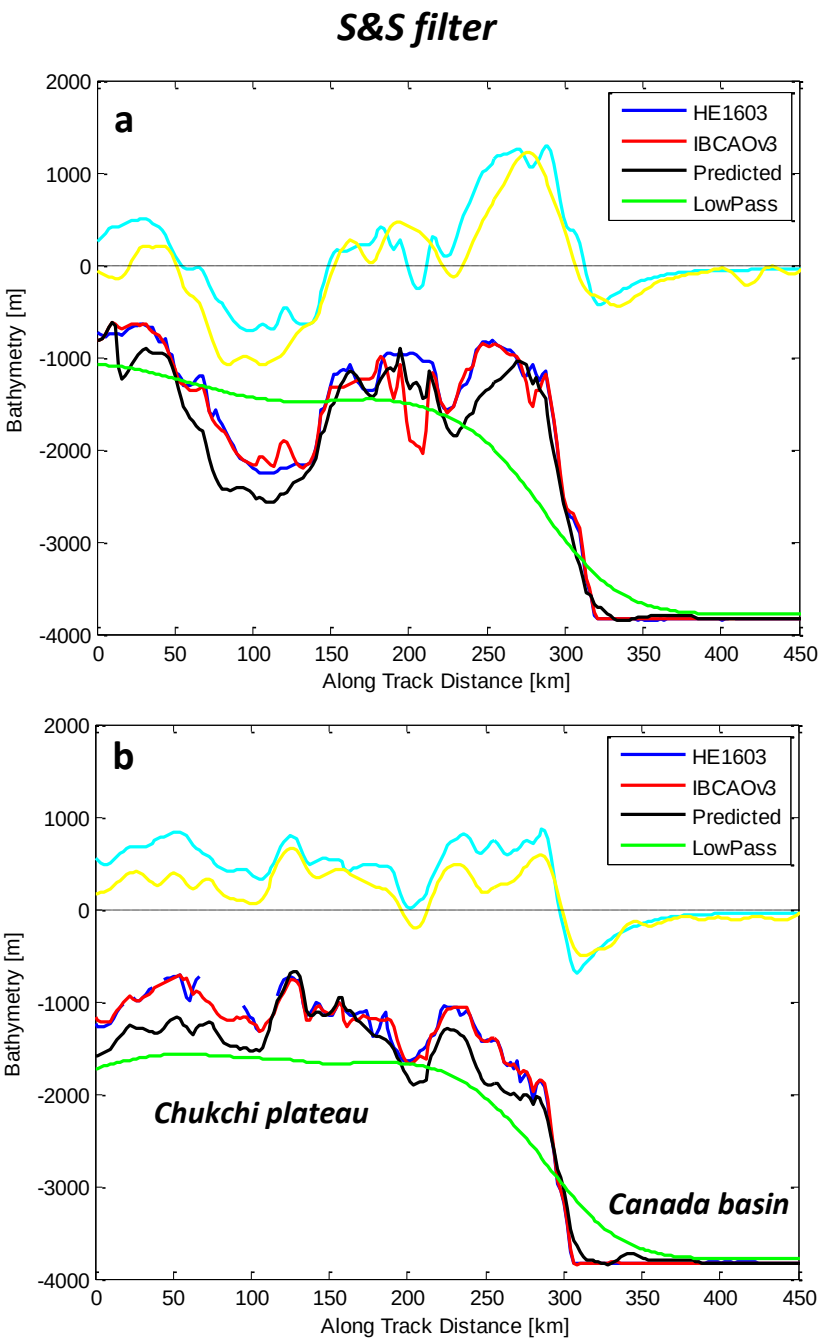

Figure 7.14: The along track profiles of Healy cruise (HE1603) (a) path 1 and (b) path 2. Predicted bathymetry using the S&S filter $W(k)$ is shown by black curve. Blue curve for the HE1603, red curve for the IBCAOv3, green curve for the low-pass filtered bathymetry $B_{long}(x,y)$, cyan for band-pass filtered bathymetry and yellow for the band-pass filtered gravity scaled by scaling factor $S(x,y)$.

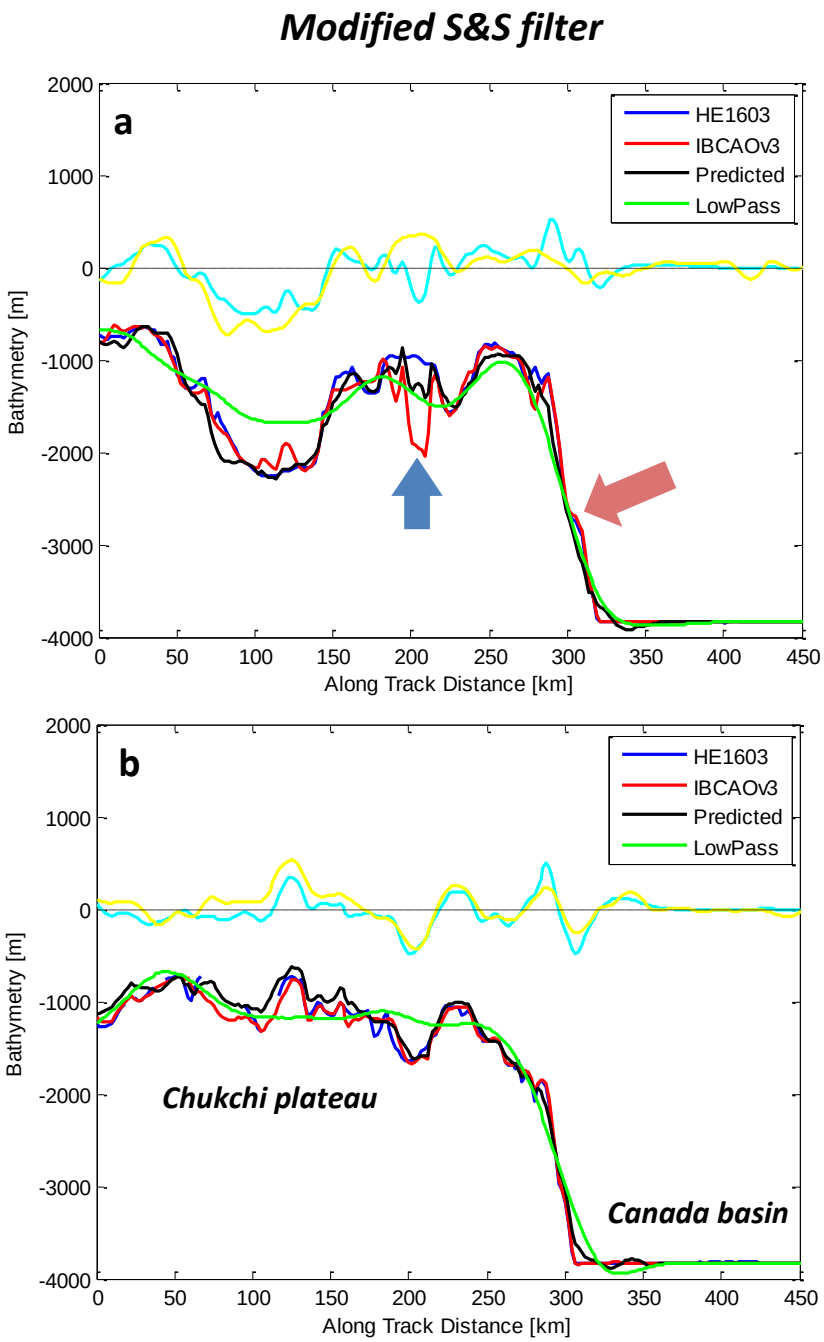

Figure 7.15: The along track profiles of Healy cruise (HE1603) (a) path 1 and (b) path 2. Predicted bathymetry using the modified S&S filter $W_m(k)$ is shown by black curve. Blue curve for the HE1603, red curve for the IBCAOv3, green curve for the low-pass filtered bathymetry $B_{long}(x,y)$, cyan for band-pass filtered bathymetry and yellow for the band-pass filtered gravity scaled by scaling factor $S(x,y)$.

7.6 Summary

The first ever Arctic bathymetry predicted from altimetric gravity anomalies is presented in this chapter.

The filtering function proposed by *Smith and Sandwell* (1994) has to be adjusted for the Arctic ocean to diminish the long wavelength problem in the gravity at high latitudes. Modified version of Smith and Sandwell filter is proposed to overcome the potential long wavelength problem in the Arctic ocean. The filtering function is used to band-pass filter the IBCAOv3 bathymetry. The gravity anomalies (DTU17 model) are also band-pass filtered and downward continued to the local sea floor.

The prediction is only done on grid nodes where the bathymetry and gravity variations are significant. Significant correlation is observed over the Chukchi Cap, along the Gakkel Ridge, Lomonosov Ridge and as well as the north Atlantic Boreas basins. Over the sedimentary basins, such as Canada basin and Amundsen basin, low or negative correlation between gravity and topography is observed. In such regions, bathymetry is not predicted from gravity.

RANSAC estimator gives higher scaling factor compared to the slope estimator and the predicted bathymetry over the rugged topography (seamounts) is closer to the accurate depth measurements from ship soundings.

Good agreement between the predicted bathymetry and input bathymetry IBCAOv3 is achieved when applying modified S&S filter. Overall, the mean difference is -0.5 m, with a std. of 81.5 m. The validation with compiled ECS bathymetry north of Chukchi plateau gives a std. of 71.7 m. Profile analysis on two Healy cruise multi-beam soundings conducted in 2016 yield 119.5 m and 77.6 m standard deviations. In addition, a questionable valley is detected in the IBCAOv3 through the profile analysis.

The uncertainty in the prediction can be attributed to several factors. Firstly, we inverted the bathymetry with the assumption of constant rock density. However, the sedimentary layers are present all over the Arctic. The sediments cover the subseafloor structures that are the main source of gravity. Thus, the correlation between gravity and bathymetry becomes less significant. Secondly, the remaining long wavelength error from the gravity model may introduce (bias) error to the predicted bathymetry.

The gravity inverted bathymetry can be combined with the existing bathymetry soundings to make a new hybrid bathymetry of the Arctic ocean.

Chapter 8

Summary, conclusions and outlook

This chapter contains a brief summary of the accomplishments and findings of the work presented in this thesis. An outlook to future work is provided based on the conclusions.

8.1 Summary and conclusions

Marine gravity modelling and bathymetry prediction from marine gravity are the two main subjects in this thesis.

Marine gravity modelling

Range precision and spatial density of altimetry observations are the two main factors limiting the accuracy and resolution of predicted marine gravity field. Before 2010, 18 months of Geosat and 11 months of ERS-1 geodetic mission data were the main source for altimetric marine gravity modelling. After 2010, CryoSat-2 has been measuring sea surface heights with a 369-day repeat cycle and improved range pre-

cision. With the novel SAR mode, along track resolution is increased to 300 m which is significantly better than ∼10km resolution of conventional satellites. Valuable observations considerably close to the coast are now available from CryoSat-2.

The study on marine gravity modelling focused on the improvement of coastal zone marine gravity from CryoSat-2 SAR mode altimetry observations in combination with Jason-1 and SARAL/Altika geodetic mission data. CryoSat-2 SAR mode acquisitions were retracked with the narrow primary peak (NPP) retracker, the SAMOSA+ retracker and the modified Brown retracker (RDSAR) described in Chapter 3. Physical retrackers (SAMOSA+ and modified Brown retracker) produce accurate and precise sea surface height observations, but struggle to fit an analytical model when the waveforms are contaminated. This happens frequently near the coastal zone and data gaps are evident near the coast. On the other hand, empirical retracker (NPP retracker) gives less precise sea surface heights compared to physical retrackers, but are able to estimate sea surface heights from nearly all available waveforms. CryoSat-2 data derived from three different retrackers were merged with Jason-1 and SARAL/Altika data to investigate the effect of retrackers on marine gravity modelling.

RTM effects were computed from digital topography (including bathymetry) models to reduce height anomalies. It was partly effective near the coast for the case study in the Mediterranean, but introduced long wavelength features in the deep sea segment. The bathymetry map of the study area was well mapped by dense ship soundings. Sediments covering the subsurface seafloor structures in the (flat) deep ocean and the assumption of constant rock density were believed to be the main error sources causing the RTM correction to be less accurate in the region. In the Indonesian case study, the height anomalies were reduced by removing RTM effects. However, large consistent residual height anomalies were found in the re-

gion causing the gravity field to be less accurate than expected. It was suggesting long wavelength problems with EGM08.

In the Mediterranean case, gravity prediction error obtained from least square collocation is less than 4 mGal near the coast, and on most of the locations better than 3 mGal. These results are much better than the Sandwell gravity field (V23.1) error in the same coastal region. Comparison to the shipborne gravity measurements suggest that gravity field predicted from altimetry data which resulting from the NPP retracker gave the best precision of 2.07 mGal. Unfortunately, the accuracy of predicted marine gravity field was hard to assess due to large errors in the "old" shipborne gravity measurements. In the Indonesian case, gravity predictions are less accurate than expected due to residual long wavelength problems in the EGM08.

Bathymetry prediction

Sea floor topography and bathymetry show linear correlation in a limited wavelength band. Based on the algorithm developed by Smith and Sandwell, 1994, bathymetry can be predicted from band-pass filtered and downward continued marine gravity anomalies in the 15−160 km wavelength band. A modified version of Smith and Sandwell (S&S) filter was proposed which limited the prediction in a band of wavelengths 15−57 km. The modified filter was designed to completely suppress wavelengths>100 km to tackle the long wavelength problems existing in EGM08. At the same time, the method to determine the scaling factor used in the bathymetry prediction was improved using the RANSAC method.

In this thesis, Arctic bathymetry was predicted from DTU17 marine gravity anomalies in the Arctic Ocean. This is the first-ever bathymetry map of the Arc-

tic Ocean predicted from marine gravity anomalies. Existing bathymetry map of the Arctic Ocean (IBCAOv3) was used as the reference bathymetry. Long wavelength (>100 km) features of sea floor topography were obtained by low-pass filtering IBCAOv3 grids. Short wavelength features that are mainly resolved by ship soundings were obtained by high-path filtering IBCAOv3 grids. Intermediate wavelength topography is then inverted from the band-pass filtered, downward continued gravity anomalies based on the use of a local scaling-factor $S(x,y)$ in regions where significant spatial correlation is found.

Linear correlation between band-pass filtered bathymetry and gravity was found to be significant(>0.5) along the ridges and continental shelf margins. Low correlations(<0.5) were observed in the sedimentary basins (Canada basin and Amundsen basin, etc.) and regions with shallow water depth. In the derivation of the Arctic bathymetry, the bathymetry was only predicted from gravity in the regions where the correlations were significant.

Bathymetry predicted using S&S filter and modified S&S filter were presented. Validation against ship sounding surveys conducted in 2016 suggest that the bathymetry predicted using modified S&S filter gave an improvement of more than 50% compared to the bathymetry predicted using S&S filter. Predicted bathymetry using the modified filter shows good agreement with two ship sounding surveys over the Chukchi plateau. A questionable valley ($\sim$1000 m) existing in IBCAOv3 was resolved from bathymetry predicted from gravity.

8.2 Outlook

CryoSat-2 is producing massive amount of precise sea surface heights from novel SAR altimetry. Jason-2 has been flying in a novel 2-year geodetic mission phase

since July 2017. The initial 2-year geodetic mission of Jason-2 will provide across track sampling of 4 km in mid-2019. This is twice denser than the 8 km across track sampling of both CryoSat-2 and Jason-1. If the mission outlives the first 2-year geodetic mission a further 2-year geodetic mission is designed to bring the across track sampling down to 2 km in 2021. The accuracy of marine gravity is expected to be further improved by the incorporating these Jason-2 geodetic mission observations.

Long wavelength problem in EGM08 found in the Indonesian case study are expected to be diminished and well modelled by including GOCE gradiometer observations and airborne gravity survey around Sulawesi island in the next generation of EGM (EGM2020).

The bathymetric results in the Arctic Ocean were very promising and bathymetry predicted from gravity anomalies can supplement the next generations of IBCAO in the Arctic Ocean in the future.

Several parameters were optimized and improved in this study. However, several additional parameters could also be improved in future predictions. Some of these parameters are the elastic plate thickness, crust density and crustal thickness which vary from region to region. More regional studies along the ridges with different choices of parameters can be investigated in the future. A smaller value for the parameter A in the low-pass filter $W_2(k)$ will allow shorter wavelength features to be present in the band-pass filtered gravity. With improved resolution and accuracy of marine gravity field, the low-pass filter can be designed to pass shorter wavelengths of gravity and thus, more detailed features of sea floor topography can be resolved from satellite altimetry as it improves in the Arctic Ocean.

The methodology for scaling factor estimation can also be improved. A combination of scaling factor estimator suggested by *Smith and Sandwell* (1994) and

the RANSAC algorithm suggested in this thesis, can be investigated in the future. RANSAC generally resulted in higher estimates compared with the slope estimator used by *Smith and Sandwell* (1994). In this way it might mitigate the underestimation of heights over the rugged topography as found by *Smith and Sandwell* (1994). A considerable amount of outliers were frequently seen in the Arctic Ocean. Other robust linear regression techniques that deal with outliers, such as repeated median estimator (*Siegel*, 1982) and Sen's slope estimator (*Sen*, 1968), can also be considered in future improvements.

Finally, ICESat-2 which was launched by NASA in September 2018, can prove to be very important to future bathymetry improvements in the Arctic Ocean. Although the mission was designed to measure ice sheet elevations and sea ice thickness, it has the potential of mapping the shallow water depth in coastal areas with calm water and as such will be an excellent supplement to bathymetry prediction from altimetric gravity and ship soundings.

Bibliography

Allan, T., and C. Morelli (1971), A geophysical study of the mediterranean sea. nato subcommittee on oceanographic research, *Tech. rep.*, Technical reports.

Alvey, A., C. Gaina, N. Kusznir, and T. Torsvik (2008), Integrated crustal thickness mapping and plate reconstructions for the high arctic, *Earth and Planetary Science Letters*, *274*(3-4), 310–321.

Andersen, O. B., and P. Knudsen (1998), Global marine gravity field from the ers-1 and geosat geodetic mission altimetry, *Journal of Geophysical Research: Oceans*, *103*(C4), 8129–8137, doi:10.1029/97JC02198.

Andersen, O. B., and P. Knudsen (2000), The role of satellite altimetry in gravity field modelling in coastal areas, *Physics and Chemistry of the Earth, Part A: Solid Earth and Geodesy*, *25*(1), 17–24.

Andersen, O. B., P. Knudsen, and P. A. M. Berry (2010), The dnsc08gra global marine gravity field from double retracked satellite altimetry, *Journal of Geodesy*, *84*(3), 191–199, doi:10.1007/s00190-009-0355-9.

Arndt, J. E., W. Jokat, B. Dorschel, R. Myklebust, J. A. Dowdeswell, and J. Evans (2015), A new bathymetry of the northeast greenland continental shelf: Constraints on glacial and other processes, *Geochemistry, Geophysics, Geosystems*, *16*(10), 3733–3753.

Balmino, G., K. Lambeck, and W. M. Kaula (1973), A spherical harmonic analysis of the earth's topography, *Journal of Geophysical Research (1896-1977)*, *78*(2), 478–481, doi:10.1029/JB078i002p00478.

Bamber, J., et al. (2013), A new bed elevation dataset for greenland, *The Cryosphere*, *7*(2), 499–510.

Banks, R., R. Parker, and S. Huestis (1977), Isostatic compensation on a continental scale: local versus regional mechanisms, *Geophysical Journal International*, *51*(2), 431–452.

Bao, L., Y. Lu, and Y. Wang (2009), Improved retracking algorithm for oceanic altimeter waveforms, *Progress in Natural Science*, *19*(2), 195–203.

Barthelmes, F. (2013), Definition of functionals of the geopotential and their calculation from spherical harmonic models, *Tech. rep.*, Deutsches Geoforschungs Zentrum (GFZ).

Barzaghi, R., et al. (2018), Geomed2: High-resolution geoid of the mediterranean, *Springer*.

Bašić, T., and R. H. Rapp (1992), Oceanwide prediction of gravity anomalies and sea surface heights using geos-3, seasat, and geosat altimeter data and etopo5u bathymetric data, *Tech. rep.*, Department of Geodetic Science and Surveying, The Ohio State University, Report No 416.

Becker, J., et al. (2009), Global bathymetry and elevation data at 30 arc seconds resolution: Srtm30_plus, *Marine Geodesy*, *32*(4), 355–371.

Bouffard, J., S. Vignudelli, P. Cipollini, and Y. Menard (2008), Exploiting the potential of an improved multimission altimetric data set over the coastal ocean, *Geophysical Research Letters*, *35*(10), doi:10.1029/2008GL033488.

Brown, G. (1977), The average impulse responce of a rough surface and its applications, *IEEE Journal of oceanic engineering*, *2*(1), 67–74.

Carron, M. J., P. R. Vogt, and W.-Y. Jung (2001), A proposed international long-term project to systematically map the world's ocean floors from beach to trench: Gomap (global ocean mapping program), *The International Hydrographic Review*, *2*(3).

Cartwright, D., and A. C. Edden (1973), Corrected tables of tidal harmonics, *Geophysical journal international*, *33*(3), 253–264.

Cartwright, D., and R. Tayler (1971), New computations of the tide-generating potential, *Geophysical Journal International*, *23*(1), 45–73.

Davis, C. H. (1995), Growth of the greenland ice sheet: A performance assessment of altimeter retracking algorithms, *IEEE Transactions on Geoscience and Remote Sensing*, *33*(5), 1108–1116.

Davis, C. H. (1997), A robust threshold retracking algorithm for measuring ice-sheet surface elevation change from satellite radar altimeters, *IEEE Transactions on Geoscience and Remote Sensing*, *35*(4), 974–979.

Dixon, T. H., M. Naraghi, M. K. McNutt, and S. M. Smith (1983), Bathymetric prediction from seasat altimeter data, *Journal of Geophysical Research: Oceans*, *88*(C3), 1563–1571, doi:10.1029/JC088iC03p01563.

Døssing, A., J. R. Hopper, A. V. Olesen, T. M. Rasmussen, and J. Halpenny (2013), New aero-gravity results from the arctic: Linking the latest cretaceous-early cenozoic plate kinematics of the north atlantic and arctic ocean, *Geochemistry, Geophysics, Geosystems*, *14*(10), 4044–4065.

Døssing, A., T. Hansen, A. Olesen, J. Hopper, and T. Funck (2014), Gravity inversion predicts the nature of the amundsen basin and its continental borderlands near greenland, *Earth and Planetary Science Letters*, *408*, 132 – 145, doi:https://doi.org/10.1016/j.epsl.2014.10.011.

Duquenne, H., M. Everaerts, and P. Lambot (2005), Merging a gravimetric model of the geoid with gps/levelling data: an example in belgium, in *Gravity, Geoid and Space Missions*, pp. 131–136, Springer.

Engen, Ø., L. N. Frazer, P. Wessel, and J. I. Faleide (2006), Prediction of sediment thickness in the norwegian–greenland sea from gravity inversion, *Journal of Geophysical Research: Solid Earth*, *111*(B11), doi:10.1029/2005JB003924.

Farr, T. G., et al. (2007), The shuttle radar topography mission, *Reviews of Geophysics*, *45*(2), doi:10.1029/2005RG000183.

Fischler, M. A., and R. C. Bolles (1981), Random sample consensus: a paradigm for model fitting with applications to image analysis and automated cartography, *Communications of the ACM*, *24*(6), 381–395.

Forsberg, R. (1984), A study of terrain reductions, density anomalies and geophysical inversion methods in gravity field modelling, *Tech. rep.*, Ohio State Univ Columbus Dept Of Geodetic Science and Surveying.

Forsberg, R. (1991), A new high-resolution geoid of the nordic area, in *Determination of the geoid*, pp. 241–250, Springer.

Forsberg, R., and M. Sideris (1993), Geoid computations by the multi-band spherical fft approach, *Manuscripta geodaetica*, *18*, 82–82.

Forsberg, R., and C. C. Tscherning (1981), The use of height data in gravity field approximation by collocation, *Journal of Geophysical Research: Solid Earth*, *86*(B9), 7843–7854.

Forsberg, R., C. Tscherning, and P. Knudsen (2008), *An overview manual for the GRAVSOFT*, Copenhagen, Denmark.

Garcia, E. S., D. T. Sandwell, and W. H. Smith (2014), Retracking cryosat-2, envisat and jason-1 radar altimetry waveforms for improved gravity field recovery, *Geophysical Journal International*, *196*(3), 1402–1422, doi:10.1093/gji/ggt469.

Gatchalian, R., R. Forsberg, and A. Olesen (2016), Pgm2016: A new geoid model for the philippines, *Tech. rep.*

Glebovsky, V. Y., E. Astafurova, A. Chernykh, M. Korneva, V. Kaminsky, and V. Poselov (2013), Thickness of the earth's crust in the deep arctic ocean: results of a 3d gravity modeling, *Russian Geology and Geophysics*, *54*(3), 247–262.

Gommenginger, C., P. Thibaut, L. Fenoglio-Marc, G. Quartly, X. Deng, J. Gómez-Enri, P. Challenor, and Y. Gao (2011), Retracking altimeter waveforms near the coasts, in *Coastal altimetry*, pp. 61–101, Springer.

Heck, B., and K. Seitz (2007), A comparison of the tesseroid, prism and point-mass approaches for mass reductions in gravity field modelling, *Journal of Geodesy*, *81*(2), 121–136, doi:10.1007/s00190-006-0094-0.

Heiskanen, W. A., and H. Moritz (1967), *Physical geodesy*, W.H. Freeman, San Francisco.

Hirt, C. (2010), Prediction of vertical deflections from high-degree spherical harmonic synthesis and residual terrain model data, *Journal of Geodesy*, *84*(3), 179–190.

Hirt, C. (2013), Rtm gravity forward-modeling using topography/bathymetry data to improve high-degree global geopotential models in the coastal zone, *Marine Geodesy*, *36*(2), 183–202.

Hofmann-Wellenhof, B., and H. Moritz (2006), *Physical geodesy*, Springer Science & Business Media, Vienna, doi:10.1007/978-3-211-33545-1.

Hwang, C., and B. Parsons (1995), Gravity anomalies derived from seasat, geosat, ers-1 and topex/poseidon altimetry and ship gravity: a case study over the reykjanes ridge, *Geophysical Journal International*, *122*(2), 551–568.

Hwang, C., E.-C. Kao, and B. Parsons (1998), Global derivation of marine gravity anomalies from seasat, geosat, ers-1 and topex/poseidon altimeter data, *Geophysical Journal International*, *134*(2), 449–459.

Hwang, C., J. Guo, X. Deng, H.-Y. Hsu, and Y. Liu (2006), Coastal gravity anomalies from retracked geosat/gm altimetry: improvement, limitation and the role of airborne gravity data, *Journal of Geodesy*, *80*(4), 204–216.

Jain, M., O. B. Andersen, J. Dall, and L. Stenseng (2015), Sea surface height determination in the arctic using cryosat-2 sar data from primary peak empirical retrackers, *Advances in Space Research*, *55*(1), 40–50.

Jakobsson, M., N. Cherkis, J. Woodward, R. Macnab, and B. Coakley (2000), New grid of arctic bathymetry aids scientists and mapmakers, *EOS, Transactions American Geophysical Union*, *81*(9), 89–96.

Jakobsson, M., R. Macnab, L. Mayer, R. Anderson, M. Edwards, J. Hatzky, H. W. Schenke, and P. Johnson (2008), An improved bathymetric portrayal of the arctic ocean: Implications for ocean modeling and geological, geophysical and oceanographic analyses, *Geophysical Research Letters*, *35*(7).

Jakobsson, M., et al. (2012), The international bathymetric chart of the arctic ocean (ibcao) version 3.0, *Geophysical Research Letters*, *39*(12), doi:10.1029/2012GL052219.

Jamil, H., et al. (2017), Airborne geoid mapping of land and sea areas of east malaysia, *Journal of Geodetic Science*, *7*(1), 84–93.

Jordan, S. K. (1972), Self-consistent statistical models for the gravity anomaly, vertical deflections, and undulation of the geoid, *Journal of Geophysical Research*, *77*(20), 3660–3670.

Kaas, E., B. Sørensen, C. C. Tscherning, and M. Veicherts (2013), Multi-processing least squares collocation: Applications to gravity field analysis, *Journal of Geodetic Science*, *3*(3), 219–223.

Kearsley, W. (1977), Non-stationary estimation in gravity prediction problems., *Tech. rep.*, Department of Geodetic Science and Surveying, The Ohio State University, Report No 256.

Kenyon, S., R. Forsberg, and B. Coakley (2008), New gravity field for the arctic, *Eos, Transactions American Geophysical Union*, *89*(32), 289–290, doi:10.1029/2008EO320002.

Knudsen, P. (1987), Estimation and modelling of the local empirical covariance function using gravity and satellite altimeter data, *Bulletin Geodesique*, *61*(2), 145–160.

Knudsen, P., and M. Brovelli (1993), Collinear and cross-over adjustment of geosat erm and seasat altimeter data in the mediterranean sea, *Surveys in geophysics*, *14*(4-5), 449–459.

Laske, G. (1997), A global digital map of sediment thickness, *Eos Trans. AGU*, *78*, F483.

Le Brocq, A. M., A. J. Payne, and A. Vieli (2010), An improved antarctic dataset for high resolution numerical ice sheet models (albmap v1), *Earth System Science Data*, *2*(2), 247–260, doi:10.5194/essd-2-247-2010.

Lequentrec-Lalancette, M., C. Salaűn, S. Bonvalot, D. Rouxel, and S. Bruinsma (2016), Exploitation of marine gravity measurements of the mediterranean in the validation of global gravity field models, in *International Symposium on Earth and Environmental Sciences for Future Generations*, pp. 63–67, Springer.

Martin-Puig, C., G. Ruffini, J. Marquez, D. Cotton, M. Srokosz, P. Challenor, K. Raney, and J. rome Benveniste (2008), Theoretical model of sar altimeter over water surfaces, in *IGARSS 2008-2008 IEEE International Geoscience and Remote Sensing Symposium*, vol. 3, pp. III–242, IEEE.

May, S. D., and A. Grantz (1990), Sediment thickness in the southern canada basin, *Marine Geology*, *93*, 331–347.

Mayer, L., B. Calder, and D. Mosher (2012), Us law of the sea cruise to map and sample the us arctic ocean margin, *Tech. rep.*, Center for Coastal and Ocean Mapping.

Mayer, L., B. Calder, and D. Mosher (2016), Us law of the sea cruise to map and sample the us arctic ocean margin, healy 1603, *Tech. rep.*, Center for Coastal and Ocean Mapping.

Mayer, L., M. Jakobsson, G. Allen, B. Dorschel, R. Falconer, V. Ferrini, G. Lamarche, H. Snaith, and P. Weatherall (2018), The nippon foundation—gebco seabed 2030 project: The quest to see the world's oceans completely mapped by 2030, *Geosciences*, *8*(2), 63.

Mayer, L. A., A. Armstrong, B. Calder, and J. Gardner (2010), Sea floor mapping in the arctic: support for a potential us extended continental shelf, *The International Hydrographic Review*, (3), 14–23.

Mayer-Gürr, T., et al. (2015), The new combined satellite only model goco05s, doi:10.13140/RG.2.1.4688.6807.

McKenzie, D., and C. Bowin (1976), The relationship between bathymetry and gravity in the atlantic ocean, *Journal of Geophysical Research*, *81*(11), 1903–1915.

Moritz, H. (1978), Least-squares collocation, *Reviews of Geophysics*, *16*(3), 421–430, doi:10.1029/RG016i003p00421.

Moritz, H. (1980), *Advanced Physical Geodesy*, Herbert Wichmann, Karlsruhe, Germany.

Nagy, D., G. Papp, and J. Benedek (2000), The gravitational potential and its derivatives for the prism, *Journal of Geodesy*, *74*(7), 552–560, doi:10.1007/s001900000116.

Nagy, D., G. Papp, and J. Benedek (2002), Corrections to "the gravitational potential and its derivatives for the prism", *Journal of Geodesy*, *76*(8), 475–475, doi:10.1007/s00190-002-0264-7.

Nettleton, L. (1939), Determination of density for reduction of gravimeter observations, *Geophysics*, *4*(3), 176–183.

Nielsen, K., L. Stenseng, O. Andersen, and P. Knudsen (2017), The performance and potentials of the cryosat-2 sar and sarin modes for lake level estimation, *Water*, *9*(6), 374.

Olesen, A. V., and R. Forsberg (2007), Airborne scalar gravimetry for regional gravity field mapping and geoid determination, in *1st Meeting of the International Gravity Field Service*.

Omang, O., and R. Forsberg (2000), How to handle topography in practical geoid determination: three examples, *Journal of Geodesy*, *74*(6), 458–466.

Pail, R., T. Fecher, D. Barnes, J. F. Factor, S. A. Holmes, T. Gruber, and P. Zingerle (2018), Short note: the experimental geopotential model xgm2016, *Journal of Geodesy*, *92*(4), 443–451, doi:10.1007/s00190-017-1070-6.

Parker, R. (1973), The rapid calculation of potential anomalies, *Geophysical Journal of the Royal Astronomical Society*, *31*(4), 447–455.

Passaro, M., P. Cipollini, S. Vignudelli, G. D. Quartly, and H. M. Snaith (2014), Ales: A multi-mission adaptive subwaveform retracker for coastal and open ocean altimetry, *Remote Sensing of Environment*, *145*, 173–189.

Passaro, M., S. K. Rose, O. B. Andersen, E. Boergens, F. M. Calafat, D. Dettmering, and J. Benveniste (2018), Ales+: Adapting a homogenous ocean retracker for satellite altimetry to sea ice leads, coastal and inland waters, *Remote Sensing of Environment*, *211*, 456–471.

Pavlis, N. K., S. A. Holmes, S. C. Kenyon, and J. K. Factor (2012), The development and evaluation of the earth gravitational model 2008 (egm2008), *Journal of Geophysical Research: Solid Earth*, *117*(B4), 1–38, doi:10.1029/2011JB008916.

Raney, R. K. (1998), The delay/doppler radar altimeter, *IEEE Transactions on Geoscience and Remote Sensing*, *36*(5), 1578–1588.

Rapp, R. H. (1979), Geos 3 data processing for the recovery of geoid undulations and gravity anomalies, *Journal of Geophysical Research: Solid Earth*, *84*(B8), 3784–3792.

Ray, C., C. Martin-Puig, M. P. Clarizia, G. Ruffini, S. Dinardo, C. Gommenginger, and J. Benveniste (2015), Sar altimeter backscattered waveform model, *IEEE Transactions on Geoscience and Remote Sensing*, *53*(2), 911–919.

Rummel, R., R. H. Rapp, H. Suenkel, and C. C. Tscherning (1988), Comparisons of global topographic/isostatic models to the earth's observed gravity field, *Tech. rep.*, Department of Geodetic Science and Surveying, The Ohio State University, Report No 388.

Sandwell, D., E. Garcia, K. Soofi, P. Wessel, M. Chandler, and W. H. Smith (2013), Toward 1-mgal accuracy in global marine gravity from cryosat-2, envisat, and jason-1, *The Leading Edge*, *32*(8), 892–899.

Sandwell, D. T., and W. H. Smith (2005), Retracking ers-1 altimeter waveforms for optimal gravity field recovery, *Geophysical Journal International*, *163*(1), 79–89.

Sandwell, D. T., and W. H. F. Smith (2009), Global marine gravity from retracked geosat and ers-1 altimetry: Ridge segmentation versus spreading rate, *Journal of Geophysical Research: Solid Earth*, *114*(B1), doi:10.1029/2008JB006008.

Sandwell, D. T., R. D. Müller, W. H. Smith, E. Garcia, and R. Francis (2014), New global marine gravity model from cryosat-2 and jason-1 reveals buried tectonic structure, *Science*, *346*(6205), 65–67.

Sansò, F., and M. G. Sideris (2013), *Geoid determination: theory and methods*, Springer Science & Business Media.

Schaffer, J., R. Timmermann, J. E. Arndt, S. S. Kristensen, C. Mayer, M. Morlighem, and D. Steinhage (2016), A global, high-resolution data set of ice sheet topography, cavity geometry, and ocean bathymetry, *Earth System Science Data*, *8*(2), 543–557, doi:10.5194/essd-8-543-2016.

Scharroo, R. (2016), Rads rdsar algorithm theoretical basis document, version0. 3, cp4o project report, 2014-updated may 2016, *http://www. satoc. eu/projects/CP4O/docs/tud_rdsar_atbd. pdf*.

Scharroo, R., E. Leuliette, J. Lillibridge, D. Byrne, M. Naeije, and G. Mitchum (2013), Rads: Consistent multi-mission products, in *Proc. of the Symposium on*, vol. 20, p. 4.

Schwarz, K., M. Sideris, and R. Forsberg (1990), The use of fft techniques in physical geodesy, *Geophysical Journal International*, *100*(3), 485–514.

Sen, P. K. (1968), Estimates of the regression coefficient based on kendall's tau, *Journal of the American statistical association*, *63*(324), 1379–1389.

Siegel, A. F. (1982), Robust regression using repeated medians, *Biometrika*, *69*(1), 242–244.

Sjöberg, L. (2005), A discussion on the approximations made in the practical implementation of the remove–compute–restore technique in regional geoid modelling, *Journal of Geodesy*, *78*(11-12), 645–653.

Smith, W. H. (2015), Resolution of seamount geoid anomalies achieved by the saral/altika and envisat ra2 satellite radar altimeters, *Marine Geodesy*, *38*(sup1), 644–671.

Smith, W. H., and D. T. Sandwell (2004), Conventional bathymetry, bathymetry from space, and geodetic altimetry, *Oceanography*, *17*(1), 8–23.

Smith, W. H. F. (1993), On the accuracy of digital bathymetric data, *Journal of Geophysical Research: Solid Earth*, *98*(B6), 9591–9603, doi:10.1029/93JB00716.

Smith, W. H. F., and D. T. Sandwell (1994), Bathymetric prediction from dense satellite altimetry and sparse shipboard bathymetry, *Journal of Geophysical Research: Solid Earth*, *99*(B11), 21,803–21,824, doi:10.1029/94JB00988.

Smith, W. H. F., and D. T. Sandwell (1997), Global sea floor topography from satellite altimetry and ship depth soundings, *Science*, *277*(5334), 1956–1962, doi:10.1126/science.277.5334.1956.

Tocho, C., G. S. Vergos, and M. G. Sideris (2012), Investigation of topographic reductions for marine geoid determination in the presence of an ultra-high resolution reference geopotential model, in *Geodesy for Planet Earth*, edited by S. Kenyon, M. C. Pacino, and U. Marti, pp. 419–426, Springer Berlin Heidelberg, Berlin, Heidelberg.

Tscherning, C., and R. Forsberg (1986), Geoid determination in the nordic countries—a status report, in *Proc. 10. General Meeting of the Nordic Geodetic Commission, Helsinki*, vol. 29, pp. 279–290.

Tscherning, C. C. (1994), Geoid determination by least-square collocation using gravsoft, in *International School for the Determination and Use of the Geoid, Lecture Notes*, pp. 135–164.

Tscherning, C. C., and R. H. Rapp (1974), Closed covariance expressions for gravity anomalies, geoid undulations, and deflections of the vertical implied by anomaly degree variance models., *Tech. rep.*, OHIO STATE UNIV COLUMBUS DEPT OF GEODETIC SCIENCE.

Tziavos, I. N., G. S. Vergos, and V. N. Grigoriadis (2009), Investigation of topographic reductions and aliasing effects on gravity and the geoid over greece based on various digital terrain models, *Surveys in Geophysics*, *31*(1), 23, doi:10.1007/s10712-009-9085-z.

Verron, J., et al. (2015), The saral/altika altimetry satellite mission, *Marine Geodesy*, *38*(sup1), 2–21.

Vignudelli, S., P. Cipollini, L. Roblou, F. Lyard, G. P. Gasparini, G. Manzella, and M. Astraldi (2005), Improved satellite altimetry in coastal systems: Case study of the corsica channel (mediterranean sea), *Geophysical Research Letters*, *32*(7), doi:10.1029/2005GL022602.

Walcott, R. (1970), Flexural rigidity, thickness, and viscosity of the lithosphere, *Journal of Geophysical Research*, *75*(20), 3941–3954.

Watts, A. B. (1978), An analysis of isostasy in the world's oceans 1. hawaiian-emperor seamount chain, *Journal of Geophysical Research: Solid Earth*, *83*(B12), 5989–6004.

Watts, A. B. (2001), *Isostasy and Flexure of the Lithosphere*, Cambridge University Press.

Watts, A. B., D. T. Sandwell, W. H. F. Smith, and P. Wessel (2006), Global gravity, bathymetry, and the distribution of submarine volcanism through space and time, *Journal of Geophysical Research: Solid Earth*, *111*(B8), doi:10.1029/2005JB004083.

Weatherall, P., et al. (2015), A new digital bathymetric model of the world's oceans, *Earth and Space Science*, *2*(8), 331–345, doi:10.1002/2015EA000107.

Werner, M. (2001), Shuttle radar topography mission (srtm) mission overview, *Frequenz*, *55*(3-4), 75–79.

Wessel, P., and W. H. F. Smith (1991), Free software helps map and display data, *Eos, Transactions American Geophysical Union*, *72*(41), 441–446, doi:10.1029/90EO00319.

Wessel, P., and W. H. F. Smith (1996), A global, self-consistent, hierarchical, high-resolution shoreline database, *Journal of Geophysical Research: Solid Earth*, *101*(B4), 8741–8743, doi:10.1029/96JB00104.

Wessel, P., D. T. Sandwell, and S.-S. Kim (2010), The global seamount census, *Oceanography*, *23*(1), 24–33.

Wessel, P., W. H. F. Smith, R. Scharroo, J. Luis, and F. Wobbe (2013), Generic mapping tools: Improved version released, *Eos, Transactions American Geophysical Union*, *94*(45), 409–410, doi:10.1002/2013EO450001.

Wingham, D., C. Rapley, and H. Griffiths (1986), New techniques in satellite altimeter tracking systems, in *Proceedings of IGARSS*, vol. 86, pp. 1339–1344.

Wingham, D., et al. (2006), Cryosat: A mission to determine the fluctuations in earth's land and marine ice fields, *Advances in Space Research*, *37*(4), 841 – 871, doi:https://doi.org/10.1016/j.asr.2005.07.027.

Yildiz, H., R. Forsberg, J. Ågren, C. Tscherning, and L. Sjöberg (2012), Comparison of remove-compute-restore and least squares modification of stokes' formula techniques to quasi-geoid determination over the auvergne test area, *Journal of Geodetic Science*, *2*(1), 53–64.

Zhang, S., and D. T. Sandwell (2017), Retracking of saral/altika radar altimetry waveforms for optimal gravity field recovery, *Marine Geodesy*, *40*(1), 40–56.

Appendices

Appendix A

Source identification grids

In this appendix, the Source IDentification (SID) grids of GEBCO and SRTM30_PLUS grids will be presented to support the case study of Mediterranean and Indonesia in Chapter 4.

A.1 Mediterranean case

The SRTM30_PLUS includes the EMODnet ship soundings in most of our study area. Only near the coastal lines, Sandwell topography grids inverted from gravity anomalies filled the data gaps. The stripes in Figure A.1 is due to the gridline/pixel node registration when producing the grids. The GEBCO_2014 SID shown in Figure A.2 is quite similar to SRTM30_PLUS SID in Figure A.1. Relatively more EMODnet ship soundings are integrated to GEBCO_2014. Therefore, we proceed with GEBCO_2014 grids in the RTM.

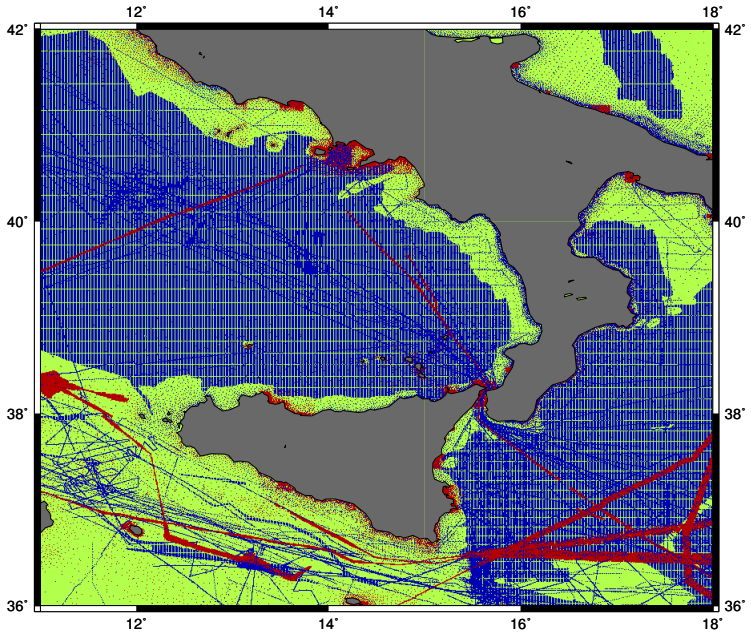

Figure A.1: Source identification grids of SRTM30_PLUS V11 released in November 2014. The light green color refers to the Sandwell topographic grids (*Sandwell et al.* (2013), V18.1), the blue color refers to the EMODnet ship soundings, and the red color refers to other (soundings) sources.

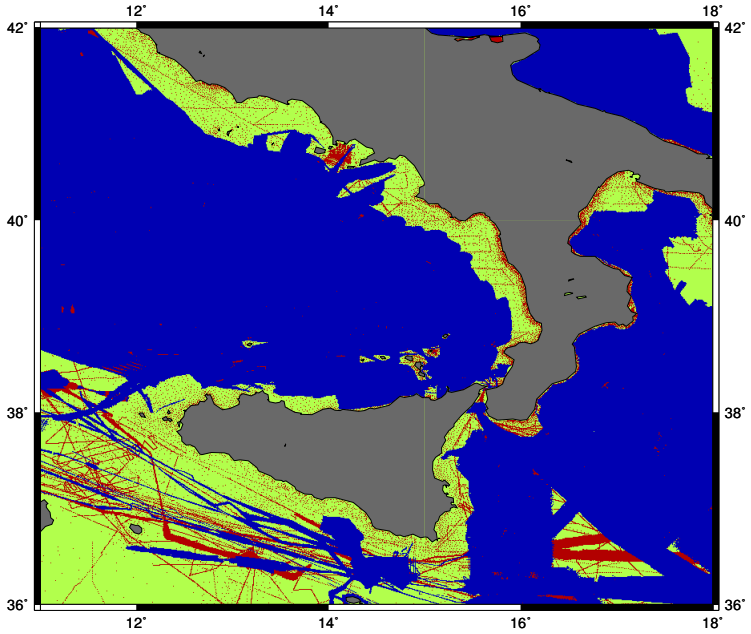

Figure A.2: Source identification grids of GEBCO_2014 released in December 2014. The light green color refers to the Sandwell topographic grids (V11.1), the blue color refers to the EMODnet ship soundings, and the red color refers to other (soundings) sources.

A.2 Indonesian case

Very few ship sounding surveys are observed from the SID grdis in the study area. As shown in Figure A.3 and A.4, the Sandwell topographic grids inverted from gravity anomalies are the main source of bathymetry in the region. By the year 2014, whether the new version of Sandwell global topography is integrated to GEBCO_2014 production remains unknown. It is clear that the Sandwell global topography V18.1 is used in the production of SRTM30_PLUS. Therefore, we proceed with SRTM30_PLUS topography for the RTM.

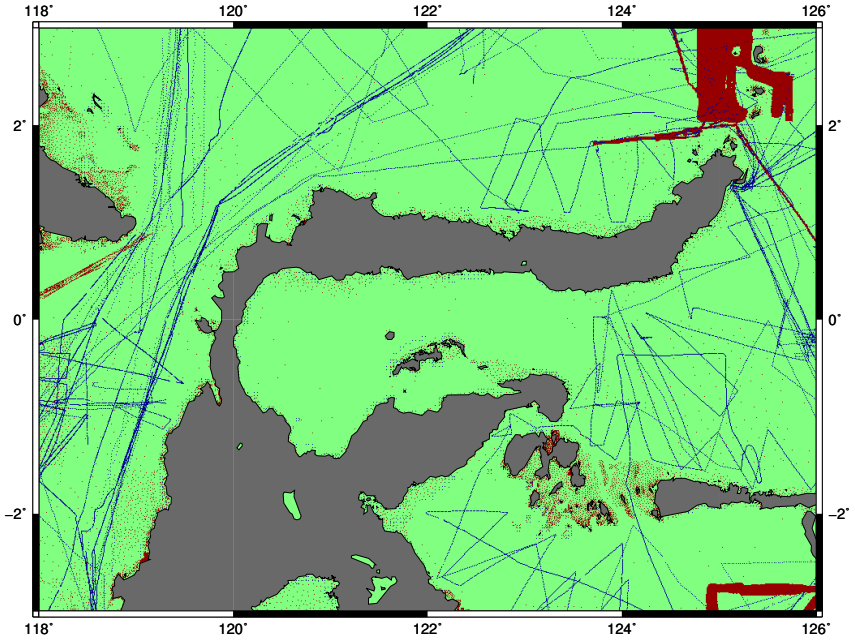

Figure A.3: Source identification grids of SRTM30_PLUS V11 released in November 2014. The light green color refers to the Sandwell topographic grids (*Sandwell et al.* (2013), V18.1), the blue and red colors refer to other (soundings) sources.

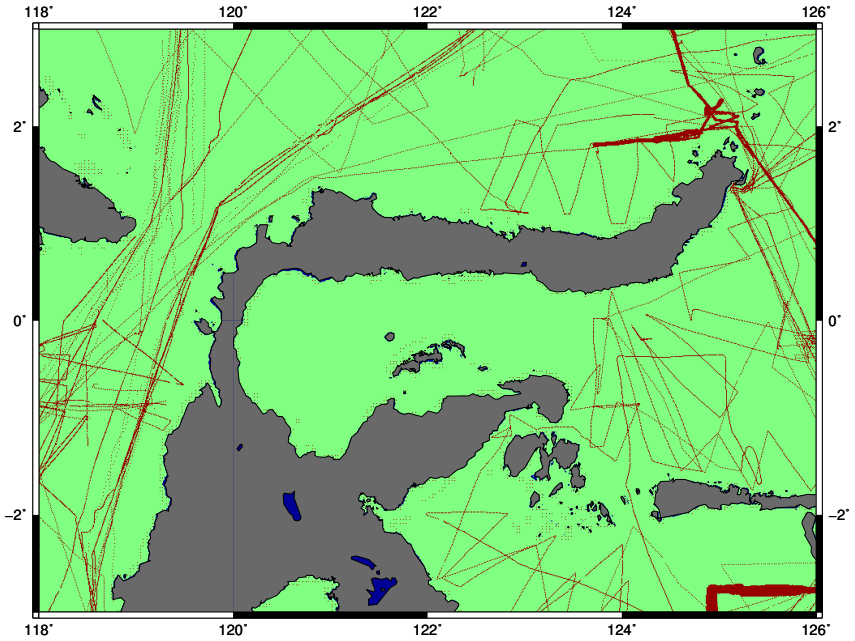

Figure A.4: Source identification grids of GEBCO_2014 released in December 2014. The light green color refers to the Sandwell topographic grids (V11.1), the blue color refers to the SRTM land topography V2.0, and the red color refers to other (soundings) sources.

Appendix B

Error estimates

In the following, we present the number of observations per 0.1° cells from three different altimetry archives and the location of larger error estimates through the least square collocation in the Mediterranean case in Section 4.1.

B.1 Number of observations per cell

The number of observations per 0.1° cells are shown in Figure B.1. The west and north margin of the patch have less observations due to the boundary clipping. Along the coastal lines at the south and east, we have relatively more altimetry observations from LARS dataset than the other two. The additional altimetry observations are mainly observed near the coastal lines.

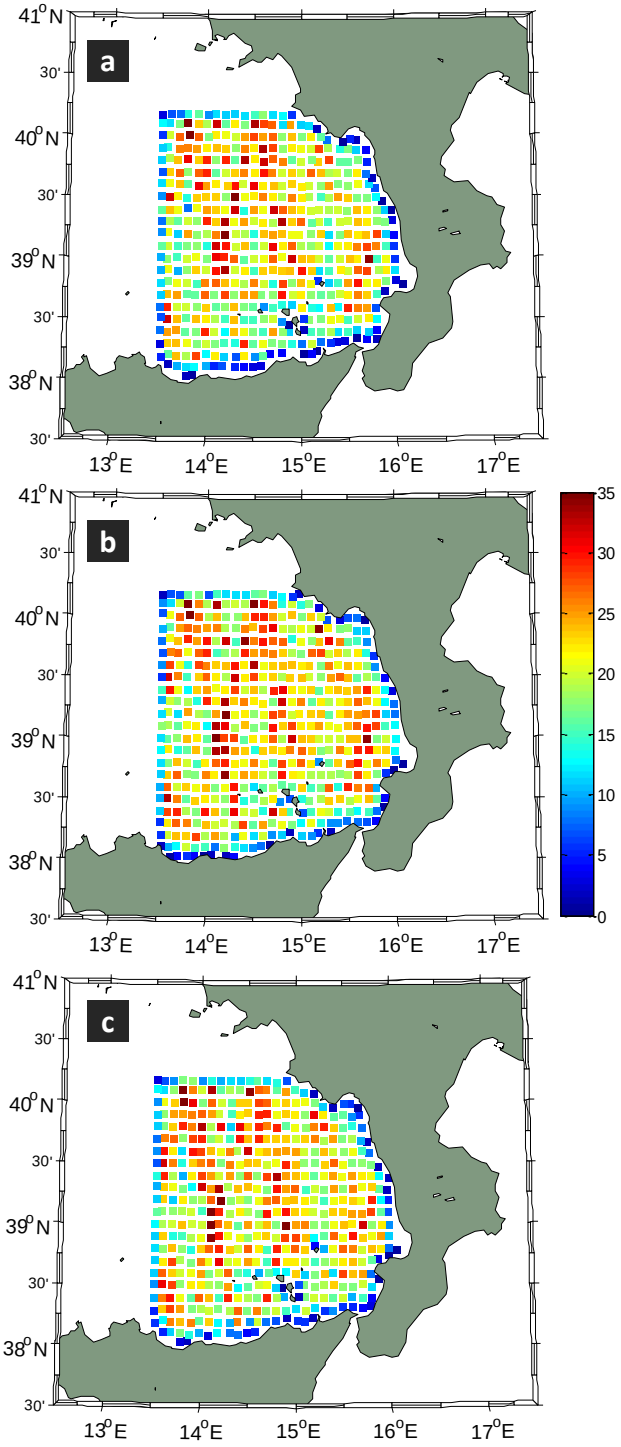

Figure B.1: The number of observations per 0.1° cell in the (a) RADS (b) LARS and (c) GPOD datasets.

B.2 Gravity anomalies with large prediction error

The locations of gravity anomalies with larger than 3 mGal prediction errors are shown in Figure B.2. The spatial distribution of these samples also implies the the spatial coverage of the altimetry observations. The majority of the samples are located where we have sparse altimetry observations as shown in Figure B.1. In total, 104, 53, and 63 samples (correspond to three different data archives) have such relatively larger (>3 mGal) prediction error. In fact, only one of the gravity anomaly estimations predicted from LARS and GPOD data has larger than 4 mGal prediction error, while it is 16 samples for RADS data. Figure B.3 shows the Sandwell gravity field (V23.1; *Sandwell et al.* (2014)) error in the same area. The prediction error goes up to 10 mGal in the coastal zone from the Sandwell gravity prediction, whereas we obtain better than 4 mGal prediction error almost all samples in the study area.

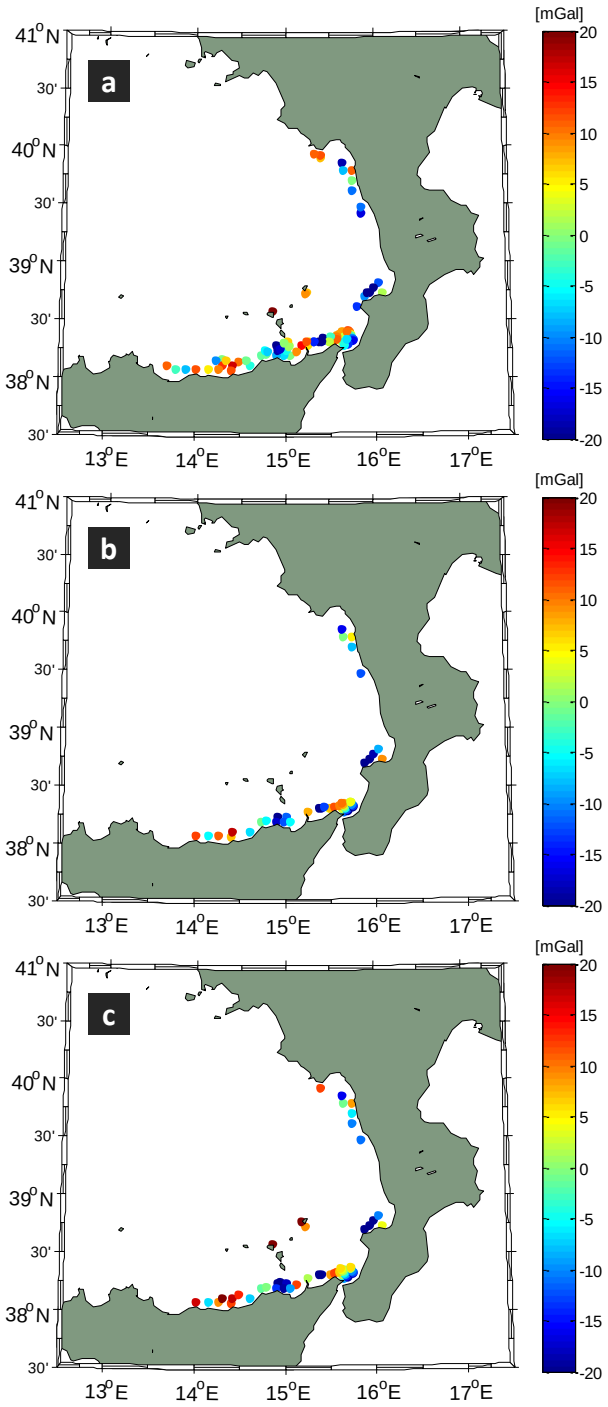

Figure B.2: The location of residual gravity anomalies estimated via LSC algorithm where prediction error is larger than 3 mGal. Three subfigures refer to the source of altimetry data i.e., (a) RADS (b) LARS and (c) GPOD datasets.

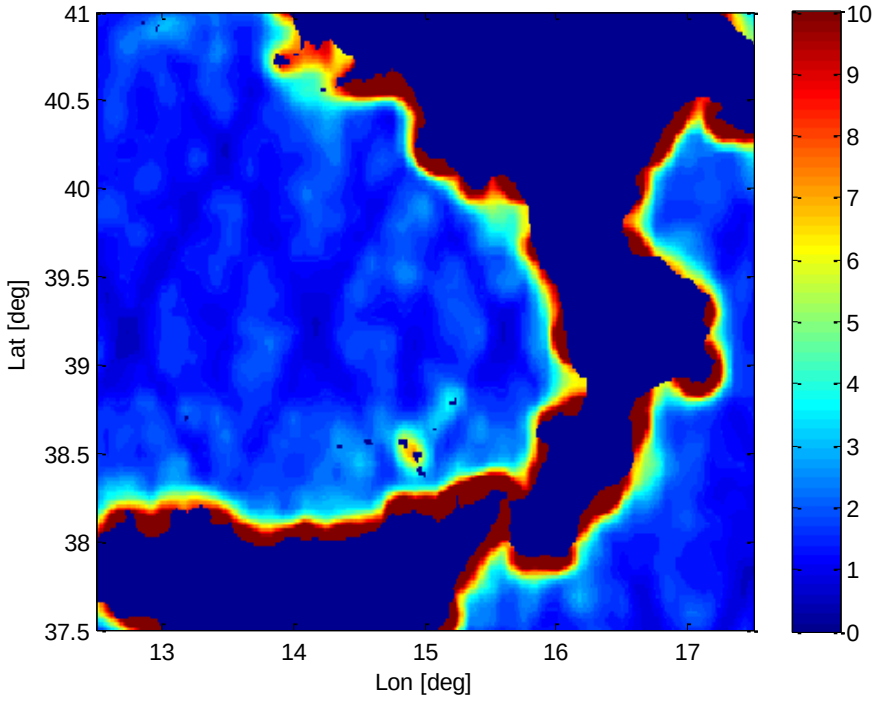

Figure B.3: Sandwell gravity field V23.1 error in the Mediterranean study. Unit: mGal

Appendix C

Publications

C.1 Improved Arctic Ocean Bathymetry derived from DTU17 Gravity model

Paper published in *Earth and Space Science*. Submitted on 13 October 2018. Accepted on 20 June 2019. Available online since 8 July 2019.

Earth and Space Science

RESEARCH ARTICLE
10.1029/2018EA000502

Special Section:
The Arctic: An AGU Joint Special Collection

Improved Arctic Ocean Bathymetry Derived From DTU17 Gravity Model

Adili Abulaitijiang[1], Ole Baltazar Andersen[1], and David Sandwell[2]

[1]DTU Space, Technical University of Denmark, Lyngby, Denmark, [2]Scripps Institute of Oceanography, University of California, San Diego, La Jolla, CA, USA

Key Points:
- The first ever Arctic bathymetry inverted from DTU17 gravity anomalies is presented
- Good agreement between the ship soundings and inverted bathymetry is achieved

Supporting Information:
- Supporting Information S1

Correspondence to:
A. Abulaitijiang,
adili@space.dtu.dk

Citation:
Abulaitijiang, A., Andersen, O. B., & Sandwell, D. (2019). Improved Arctic Ocean bathymetry derived from DTU17 gravity model. *Earth and Space Science*, *6*. https://doi.org/10.1029/2018EA000502

Received 13 OCT 2018
Accepted 20 JUN 2019
Accepted article online 8 JUL 2019

Abstract The existing bathymetry map of the Arctic is a compilation of ship soundings and digitized contours. Due to the presence of all-year sea ice, costly operations and political restrictions, dense and full coverage of the Arctic is not possible, leaving huge gaps between the existing surveys. In this paper, we make use of the existing Arctic bathymetry IBCAOv3 and invert Arctic bathymetry from the recent altimetric gravity model DTU17, whose accuracy is improved significantly with revised data processing strategy. The long and short wavelength components are preserved from IBCAOv3. The band-pass-filtering function proposed by Smith and Sandwell (1994, https://doi.org/10.1029/94JB00988) is adapted for the Arctic by reducing the cutoff wavelength. The predicted bathymetry is within 100 m on 85.8% of the grid nodes, when compared to the IBCAOv3. The consistency of the prediction is validated with two independent profiles from Healy cruises conducted in 2016 over the Chukchi Cap. A questionable valley in the IBCAOv3 is detected with gravity and at this spot, bathymetry predicted from gravity is consistent with independent multibeam soundings. The gravity-inverted bathymetry could be combined with ship soundings for the next generation of Arctic bathymetry map.

1. Introduction

The sea floor topography plays an important role in understanding geological tectonic evolution, geophysical and oceanographic studies, for example, ice-ocean interaction, ocean circulation, and tidal modeling (Cancet et al., 2018). Several global bathymetry models of the oceans are developed, namely, the General Bathymetric Chart of the Oceans (GEBCO, latest version GEBCO_2019; Weatherall et al., 2015), Refined Topography data set (RTopo, latest version RTopo-2; Schaffer et al., 2016), and the new global topography SRTM30_PLUS (Becker et al., 2009). The global models are combinations of different data sources dedicated for Arctic, Antarctic, and general oceans. RTopo-2 includes new regional data sets released recently, for example, the Greenland continental shelf and fjords (Arndt et al., 2015; Bamber et al., 2013) and the edges of Antarctic ice shelf (Le Brocq et al., 2010). The latest bed topography of Greenland (BedMachine, Version 3) is developed by integrating new bathymetry data from different sources (Morlighem et al., 2017). All the models partially or fully integrate the International Bathymetric Chart of the Arctic Ocean (IBCAO) to achieve complete coverage in the Arctic regions.

However, the Arctic Ocean bathymetry is not well surveyed due to the presence of sea ice and harsh climate in the polar region. There have been campaigns to map the sea floor topography through ship sounding, but it only covers the very small fraction of the entire Arctic, and meanwhile, it is very costly to operate. The most recent release of IBCAO (Version 3.0, IBCAOv3; Jakobsson et al., 2012) is obtained by interpolating the sparse ship sounding data into a loosely constrained regular grid. Where the grid cells are unconstrained by ship soundings, depths are obtained by interpolation. Digitized bathymetric contours are extensively used for gridding and to fill the data gaps. The Arctic bathymetry and the source of ship sounding data used in the IBCAOv3 production are shown in Figure 1.

Most part of the Arctic Ocean, such as the East Siberian Sea, Chukchi Sea, Kara Sea, and Barents Sea, are very shallow, with average depth ranging from 50 to 230 m. These continental shelves are relatively flat and have steep topographic variations at the margins to the major basins (e.g., Canada basin). A physiographic classification of Arctic Ocean seafloor and general description of geological features are presented by Jakobsson et al. (2003). The Chukchi Cap extends from the north of Alaska toward the Arctic Ocean and has been the region of interest in extending the definition of the continental shelf seaward following Article 76 of United Nations Convention of the Law of the Sea (Gardner et al., 2006). The thickness of

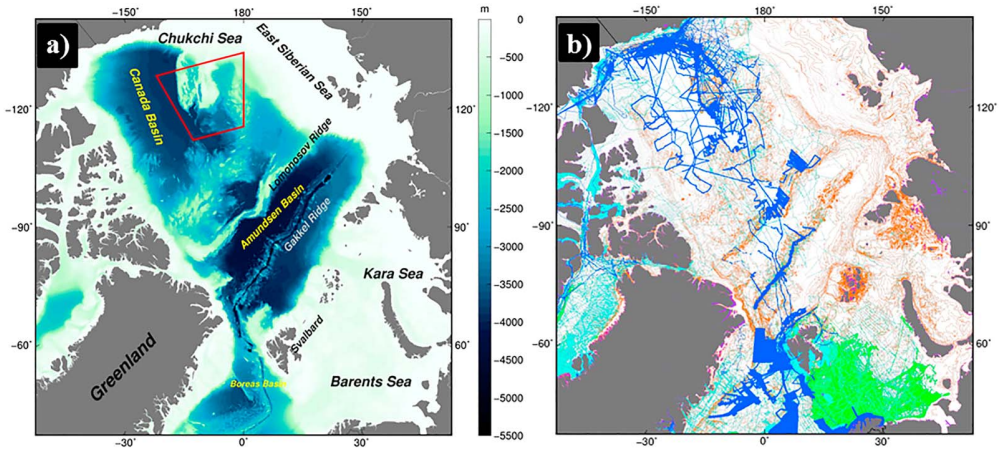

Figure 1. Maps showing (a) the IBCAOv3 bathymetry; the area bounded by the red box is Chukchi Cap (plateau); (b) the source of the ship sounding data used for IBCAOv3 production (Jakobsson et al., 2012); purple color indicates data from land digital elevation model, blue color indicates data from multibeam data, cyan color indicates single-beam data, green indicates data from Olex (www.olex.no), and orange indicates depth contours from digitized charts.

sediments (Døssing et al., 2014; Laske & Masters, 1997) in the deep Amundsen basin is approximately 2 km, while it is up to 11 km in the Canada basin (May & Grantz, 1990). The sedimentary basins appear nearly flat on the bathymetry maps.

The sea surface gravity and sea floor topography relationship is described by McKenzie and Bowin (1976) and Parker (1973). On a limited bandwidth, the linear correlation between band-pass-filtered gravity and bathymetry is estimated by statistical Pearson's correlation coefficient and the gravity-to-topography ratio (or scaling factor) can be determined by robust linear regression.

Smith and Sandwell (1994) developed the algorithm to predict the bathymetry from gravity in the 1990s. The global bathymetry models predicted from altimetric gravity so far goes up to latitude 81°N; however, the bathymetry beyond that latitude has not been predicted from gravity due to the less accurate marine gravity at high latitudes. Gravity inversion has been applied for the large-scale subcrust geometry estimation and sediment thickness mapping, in combination with seismic soundings (Alvey et al., 2008; Engen et al., 2006; Glebovsky et al., 2013). However, the accuracy of the existing bathymetry (IBCAOv3) is still uncertain at the high latitudes.

In this paper, we present the first result of Arctic bathymetry map inverted from the most recent altimetric gravity model DTU17. The spatial correlation between band-pass-filtered gravity and bathymetry is made to estimate the scaling parameter between gravity and bathymetry. The results from Smith and Sandwell (1994) algorithm and its modified version are presented and validated with the input IBCAOv3. Predicted bathymetry is validated with two multibeam ship sounding surveys that are released after the production of IBCAOv3 in 2012.

2. Data and Algorithm

2.1. Bathymetry Data

The existing bathymetry map IBCAOv3 is a compilation of multibeam, single-beam, Olex seabed mapping (www.olex.no) system and digital contour maps with a grid spacing of 500 m (Polar Stereographic projection, with true latitude at 75°N) and reveals detailed features on the sea floor. The bathymetry grid nodes are well constrained when the sounding data are available. However, the areas with no soundings are interpolated to fill the gaps (Jakobsson et al., 2012). The IBCAOv3 serves as the base for the input bathymetry grid.

2.2. Gravity Data

The accuracy of long wavelength (greater than 100 km) gravity field in the Arctic is slightly poorer than that in the midlatitudes. The long wavelength signal in the DTU17 gravity model (Andersen & Knudsen, 2019) is from Earth Gravitational Model 2008 (EGM2008; Pavlis et al., 2012), in which the primary data source in the

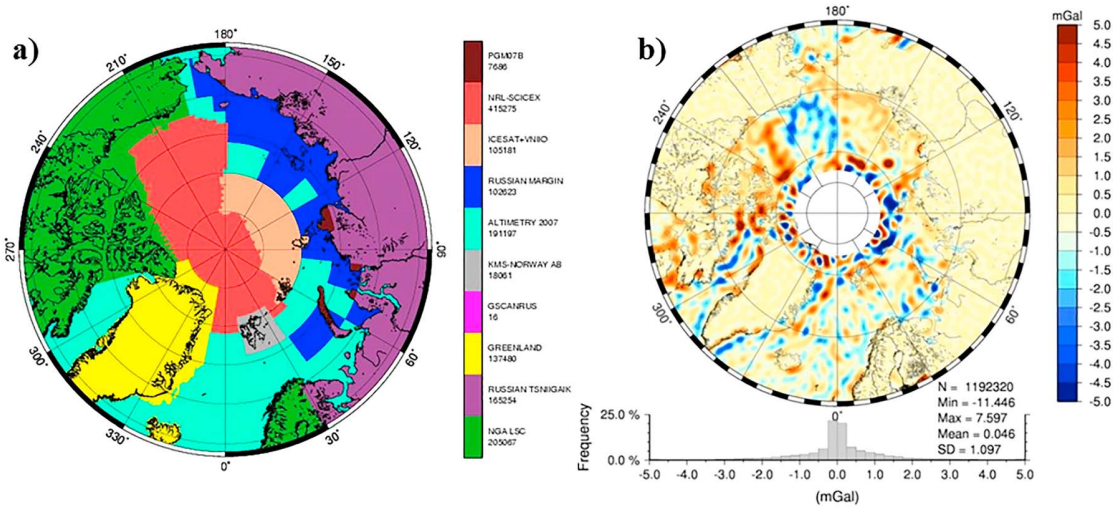

Figure 2. (a) The source of gravity data information in the ArcGP project (Kenyon & Forsberg, 2008); (b) The difference of ArcGP gravity field (EGM2008) and combined satellite-only gravity model GOCO05S (Mayer-Gürr et al., 2015) up to degree and order 200 (corresponding half-wavelength 100 km). Courtesy of Simon Holmes.

Arctic is from the Arctic Gravity Project (ArcGP; Kenyon & Forsberg, 2008), see Figure 2. As much as 5 mGal difference is observed on the long wavelength gravity field, when the ArcGP gravity anomalies are compared to GOCO05S satellite-only gravity model (Mayer-Gürr et al., 2015). The differences are partly attributed to the patched gravity data from multiple sources in the ArcGP. Moreover, the differences at higher latitudes (>80°N) are significant (Pail et al., 2018). If not filtered properly, these could be translated into bathymetry prediction error.

The altimetric gravity model developed at DTU Space included the 25 years of satellite altimetry data over the ocean. Between 70°N and 81.5°N, the ERS-1/2, EnviSat, 7 years of CryoSat-2 altimetry data, and 1 year of SARAL/AltiKa data from geodetic phase is used; between 81.5°N and 88°N, only CryoSat-2 data is used; the remaining polar gap is filled by the ArcGP gravity compilations. The latest version DTU17 marine gravity model (1-arcmin grid spacing) is released with a main improvement in the Arctic where the accuracy is increased from 9.82 (for EGM2008) to 3.78 mGal when compared to the LOMGRAV-09 aerogeophysical survey north of Greenland between 82°N and 90°N (see Figure S1 and S2 in the supporting information). The huge improvement in the Arctic motivated us to predict the bathymetry from gravity. The geographic grid of DTU17 is coregistered to the IBCAOv3 bathymetry grid using Polar Stereographic projection.

2.3. Land Mask

In addition to the input bathymetry and gravity grids, we need a land mask so to constrain the correlation analysis only to the points over the ocean. The Global Self-consistent, Hierarchical, High-resolution Geography database (Wessel & Smith, 1996) coastlines assembled in the Generic Mapping Tool (Wessel & Smith, 1991; Wessel et al., 2013) are imported and coregistered with the bathymetry grid using Polar Stereographic projection.

2.4. Algorithm

In the Polar Stereographic coordinate system, the coordinates of a grid node are given by easting and northing. For simplicity, the coordinates are denoted by a symbol x in the following. The predicted bathymetry $H_p(x)$ can be written as the sum of the long wavelength component of the input bathymetry $B_{long}(x)$, inverted topography from band-pass-filtered gravity $G_{BP}(x)$ and remaining short-wavelength components from the high-pass filter of the input bathymetry $B_{\text{short}}(x)$, as below

$$H_p(x) = B_{\text{long}}(x) + S(x) \cdot G_{BP}(x) + B_{\text{short}}(x), \tag{1}$$

where $S(x)$ is the scaling factor used to convert gravity to topography, with unit m/mGal.

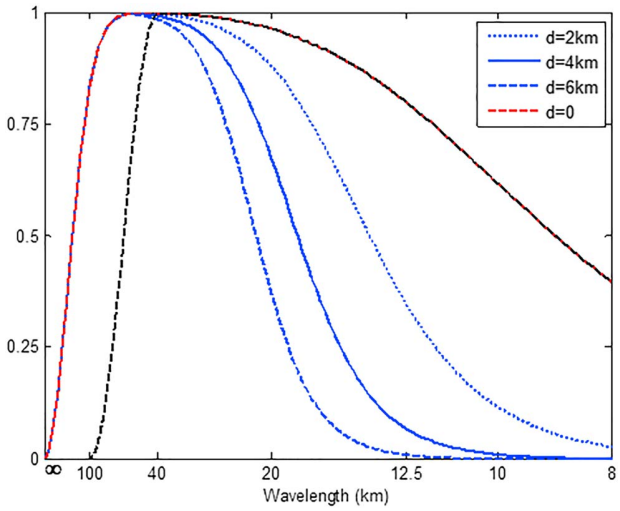

Figure 3. The S&S filter $W(k) = W_1(k)W_2(k)$ without exponential term at different depth d is shown in blue color. Modified S&S filter $W_m(k) = W_c(k)W_2(k)$ with $d = 0$, is shown by the black dashed curve. The horizontal axis is converted from wave number k to wavelength in kilometer.

The details of algorithm used for the development of Arctic bathymetry can be referred to the paper from Smith and Sandwell (1994). The assumed correlation in the wavelength between the downward continued gravity and bathymetry is between 15 and 160 km. In the Arctic, there might be errors on the long wavelength components in the gravity. Therefore, a proper band-pass-filtering function has to be designed to obtain the band-pass-filtered gravity and bathymetry.

The band-pass-filtering function proposed by Smith and Sandwell (1994) is referred as Smith&Sandwell (S&S) filter in the following sections. The general form is

$$W(k) = W_1(k) \cdot W_2(k) \cdot \exp[2\pi kd], \tag{2}$$

where $W_1(k)$ is a high-pass Gaussian filter; $W_2(k)$ is a low-pass filter, the exponential term is the downward continuation operator, in which d is the depth in kilometers, and k is the wave number with unit per kilometer; the forms for $W_1(k)$ and $W_2(k)$ are

$$W_1(k) = 1 - \exp\left[-2(\pi ks)^2\right], \tag{3}$$

$$W_2(k) = \left\{1 + Ak^4 \exp[4\pi kd]\right\}^{-1}. \tag{4}$$

The s in $W_1(k)$ is the Gaussian parameter ($s = 30$ km) with assumed crust thickness of 7 km; the $W_1 = 0.5$ when $k^{-1} = 160$ km; the A parameter in $W_2(k)$ is a constant chosen by the spectral coherence (between bathymetry and gravity) analysis, here we used $A = 6{,}233$ km^4; $W_2(k)$ is a function of depth, and in the deeper ocean depths (e.g., $d = 6$ km), the gravity signal is suppressed by this filter at "longer" wavelengths, compared to that of shallow sea floor (e.g., $d = 2$ km), see Figure 3.

As described in the previous section, the long wavelength error in the Arctic has to be suppressed to avoid the prediction error in the bathymetry. A new filter is designed to accommodate the S&S filter for the Arctic. Here it is referred as modified S&S filter $W_m(k)$. A cosine-taper filter $W_c(k)$ replaces the $W_1(k)$ high-pass filter to cut off the wavelength greater than 100 km and pass the wavelength shorter than 40 km.

$$W_c(k) = 0.5 \times \left[1 + \cos\left(\pi \bullet \frac{k - k_p}{k_c - k_p}\right)\right], \tag{5}$$

where the k_c is the cutoff wave number (1/100 km^{-1}) and k_p is the high-pass wave number (1/40 km^{-1}). Thus, the $W_c = 0.5$ when $k^{-1} = 57$ km. Then, the modified S&S filter is given by

$$W_m(k) = W_c(k) \cdot W_2(k) \cdot \exp[2\pi kd]. \tag{6}$$

The combination of $W_1(k)$ and $W_2(k)$ yields a band-pass-filtering function as shown in Figure 3. All the operations are conducted in the wave number domain. Since the grids are uniformly sampled in the polar stereographic projection (500-m grid spacing), we apply forward Fourier transform to the entire grid.

The long wavelength component of the input bathymetry $B_{\text{long}}(x)$ is obtained by low-pass filtering as below

$$B_{\text{long}}(k) = B(k)[1 - W_*(k)] \tag{7}$$

where $B(k)$ is a Fourier transform of the input bathymetry grid (IBCAOv3), $W_*(k)$ is either $W_1(k)$ in equation (3) or $W_c(k)$ in equation (4).

The bathymetry grid is filtered with $W(k)$ or $W_m(k)$ to obtain the band-pass-filtered bathymetry $B_{\text{BP}}(k)$, where the depth term $d = 0$, which corresponds to the red or black dashed curve in Figure 3.

After applying the filtering function, an inverse Fourier transform is needed to achieve the band-pass-filtered version of the gravity $G_{\text{BP}}(x)$ and bathymetry $B_{\text{BP}}(x)$ grids, and the gravity-to-topography scaling

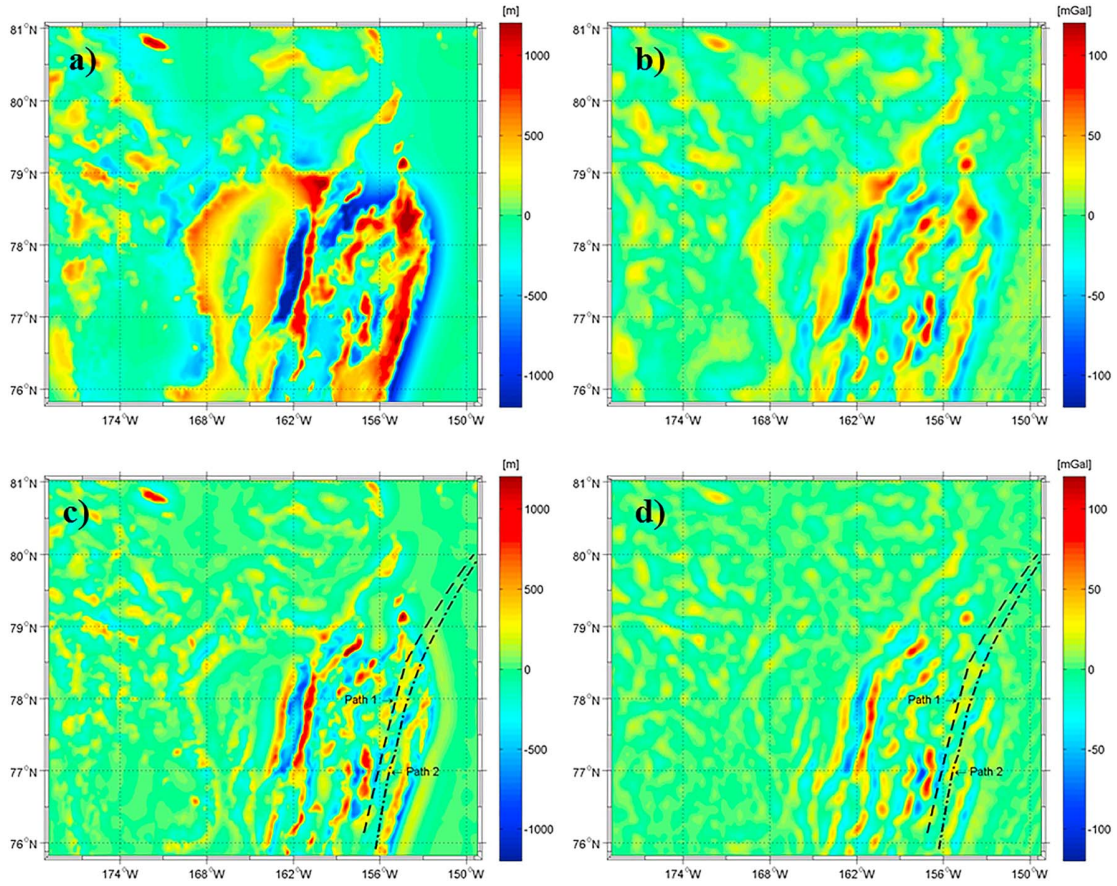

Figure 4. Band-pass-filtered bathymetry (a) and gravity (b) when using $W(k)$ from Smith and Sandwell (1994); Band-pass-filtered bathymetry (c) and gravity (d) when using modified S&S filter $W_m(k)$ proposed in this paper. Two northbound Healy cruises from HE1603 crossing the Chukchi Cap are shown by the dashed curve, which will be used for profile analysis later.

parameter $S(x)$ is estimated from these two data sets. In Figure 4, the band-pass-filtered bathymetry and gravity of the area bounded by the red box in Figure 1a are shown. The remaining long wavelength features are evident when using the $W(k)$ filter (in which $W_1 = 0.5$ when $k^{-1} = 160$ km).

Following Smith and Sandwell (1994), we make use of the Median Absolute Deviation (MAD) of the $G_{\mathrm{BP}}(x)$ and $B_{\mathrm{BP}}(x)$ values g_{mad} and h_{mad} for the estimation of $S(x)$, see equation (8). The Smith and Sandwell approach is denoted as "slope estimator" in the following. The grid spacing of $S(x)$ is 30 km, and gravity and bathymetry pairs within the 30-km radius block are used for one scaling factor estimation. Meanwhile, only grid nodes over the oceans (through a land-ocean mask) are used for this estimation.

$$S(x) = \mathrm{sign}[\rho]\frac{h_{\mathrm{mad}}}{g_{\mathrm{mad}}}, \tag{8}$$

where ρ is the linear correlation coefficient estimated from data pairs. The correlation can be any value between -1 and 1. The sign of the correlation coefficient is assigned to the scaling factor $S(x)$ as indicated in equation (8).

The magnitude of $S(x)$ is subject to the small changes in g_{mad} and h_{mad}. Alternative to the slope estimator (equation (8)), we can use RANdom SAmple Consensus (RANSAC) algorithm (Fischler & Bolles, 1981) as a robust estimator of the scaling parameter $S(x)$. An example of the RANSAC estimates along with the slope estimators (equation (8)) are shown in Figure 5. The scaling parameter $S(x)$ is estimated at the center of the 30-km radius block. One scaling factor (slope of the line fitted to the scattered pairs in Figures 5e and 5f) is estimated for a pair of band-pass-filtered gravity and bathymetry block. In contrast, the linear least squares

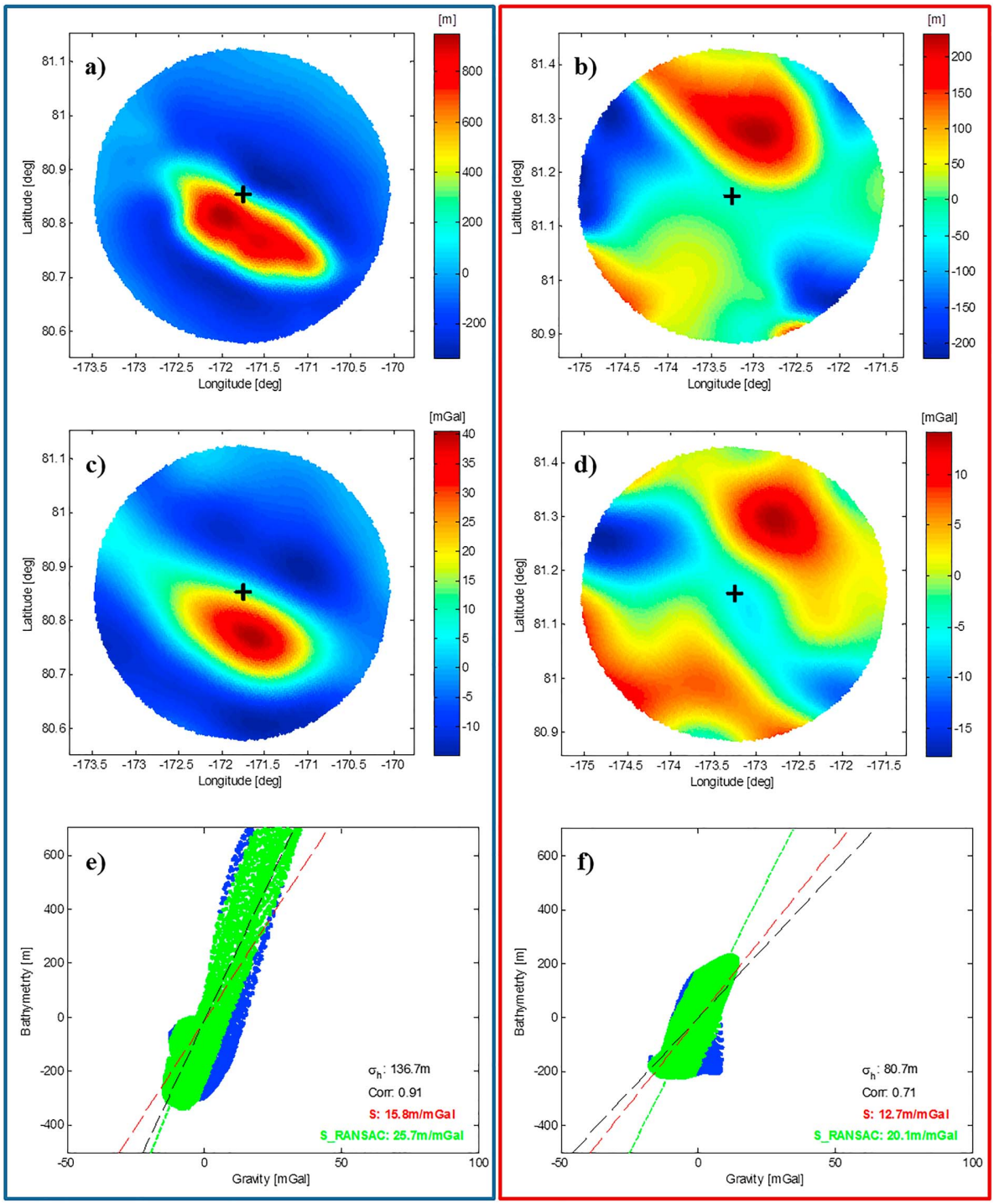

Figure 5. Illustrations of scaling factor estimations at two different locations. Blue frame on the left refers to a spot over a seamount, while the red frame on the right refers to a region with moderate topographic variations. Top two rows: band-pass-filtered bathymetry (a and b) and gravity (c and d) in a 30-km radius cap. Thick black + marker shows the center of the cap and it is the location of local scaling factor $S(x)$. Bottom row: local scaling factor $S(x)$ (e and f; slope of the lines) estimated using different algorithms. Red line for the slope estimator (equation (8)), green for the RANSAC estimator and black for the least squares fitting. The scattered points for band-pass-filtered bathymetry and gravity are marked in blue, while the green RANSAC inliers are superimposed on them. RANSAC = RANdom SAmple Consensus.

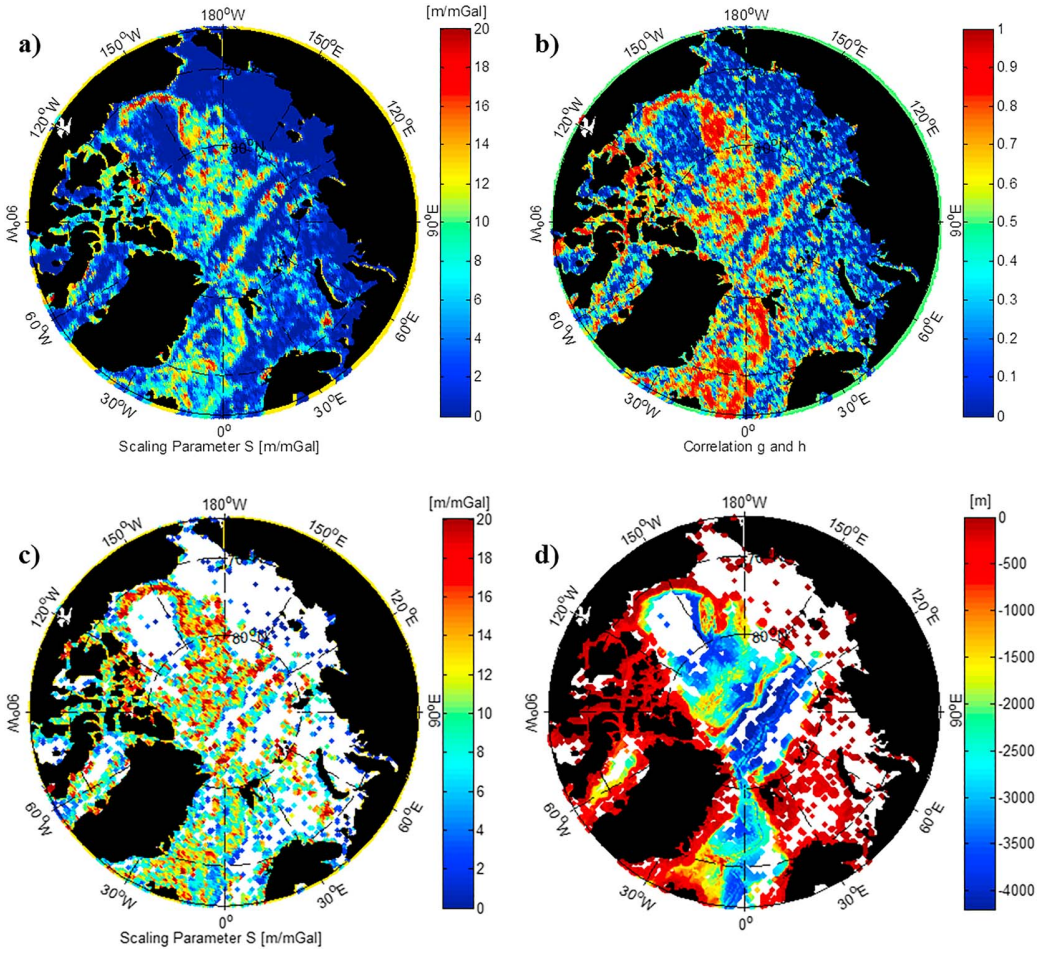

Figure 6. (a) Scaling factor $S(x)$ estimated on 30-km spacing grid nodes, (b) correlation coefficients between band-pass-filtered gravity and bathymetry on a grid spacing of 30 km in the Arctic, when the modified S&S filter $W_m(k)$ is used. (c) Scaling parameters where correlation between topography and gravity is higher than 0.5. (d) Predicted bathymetry on grid nodes where significant correlations are observed.

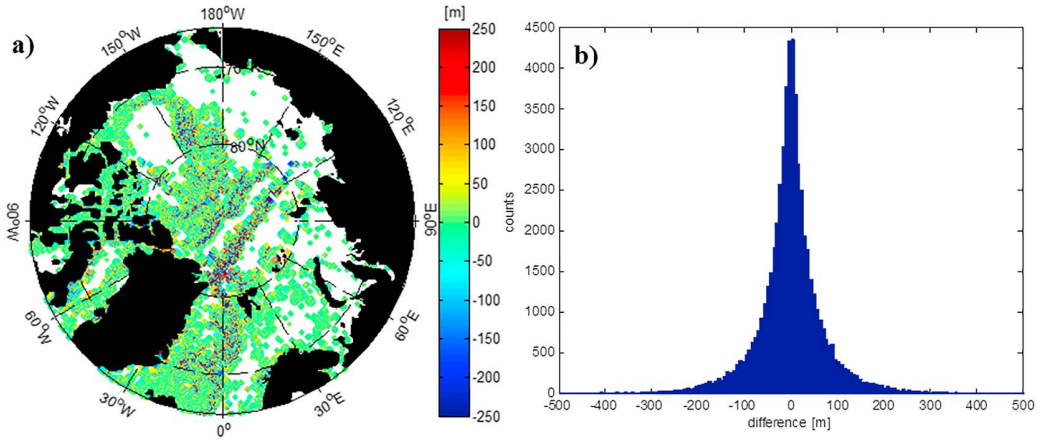

Figure 7. (a) The difference of predicted bathymetry and IBCAOv3, when the modified S&S filter $W_m(k)$ is used. (b) Histogram of differences between predicted bathymetry and IBCAOv3.

Table 1
The Difference of Predicted Bathymetry $H_p(x)$ and IBCAOv3 Using Different High-Pass Filtering Functions, $|\Delta h|$ Implies Absolute Difference and Showing the Percentage of Grid Nodes That Are Smaller Than 100 m

High-pass filter	$\|\Delta h\| < 100$	Mean	Std.	Min	Max
$W_1(k)$	64.8%	7.7	143.7	−1531.8	1,862.2
$W_c(k)$	85.8%	−0.5	81.5	−782.9	1,129.7

Note. Unit: m.

fitting (LSF, shown in black dashed line in Figure 5, bottom panel) is also tested. The estimated slope from LSF is close to RANSAC, but it could deviate dramatically from the RANSAC estimates when the data pairs are widely scattered, see Figure 5f.

The advantage of RANSAC algorithm is that it will try to search for the most "inliers" in the scattered data, and the "outliers" will not be considered for the slope estimation. As shown in Figure 5, the RANSAC algorithm fits to the general extent of the scattered data. A difference of 10 m/mGal in the scaling factor gives a difference of 400 m in the predicted bathymetry, which is significant over the seamounts..

3. Results

The scaling parameter and spatial correlation on a grid spacing of 30 km is shown in Figures 6a and 6b. On most part of the shallow continental shelf in the Arctic, both the correlation and scaling factor is low. In such parts, we simply set $S(x) = 0$, and keep the original bathymetry grid values.

Moderate correlation and scaling factor $S(x)$ are obtained over the Chukchi Cap, along the Gakkel Ridge, Lomonosov Ridge, and the north Atlantic Boreas basin. The topography is inverted from gravity in these regions.

We used a correlation threshold of 0.5 to filter out the low correlation nodes in the $S(x)$ grid (Figure 6c). The ocean ridges and continental shelf margins are visible after screening out nodes with low correlation. Grid nodes at the sedimentary Canada basin and Amundsen basin, along with shallow continental shelves around the Russian coast, are filtered out. To achieve the predicted heights, the 30-km spacing $S(x)$ grid is interpolated and coregistered with the band-pass-filtered gravity grid $G_{\mathrm{BP}}(x)$. This is achieved by General Mapping Tool *surface* module. Then the converted bathymetry can be computed. At the very final step, the fine scale features of the bathymetry $B_{\mathrm{short}}(x)$ (derived from $[1 - W_2(k)]$ high-pass filter) should be added back, to have the predicted bathymetry $H_p(x)$, see Figure 6d.

Subsequently, we can compare our prediction resulting from modified S&S filter $W_m(k)$ with the initial input bathymetry grids (IBCAOv3) on the same grid nodes. The differences are shown in Figure 7. The mean difference is −0.5 m and the standard deviation (std.) of the differences is 81.5 m. On 85.8% of the grid nodes, the absolute differences are less than 100 m. This indicates that the bathymetry inverted from gravity has good agreement with the existing bathymetry of the Arctic in general. However, very large differences are observed at Gakklel ridge, which is located more than 3,500 m below sea level. From the source identification grid in Figure 1b, we can observe that there are dense multibeam surveys right along the ridge axis, which maps the detailed features of local seafloor. The cause of the differences can be attributed to the

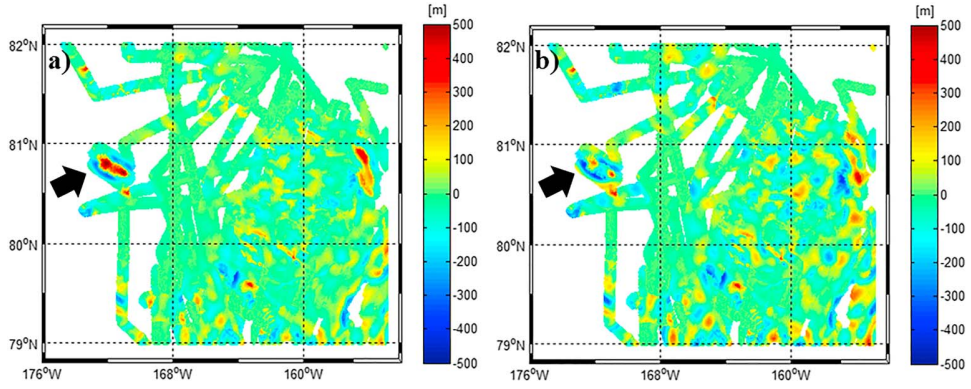

Figure 8. The difference of compiled ECS (multibeam) bathymetry data and predicted bathymetry resulting from different scaling factor estimation algorithms on the north of Chukchi Cap. (a) Scaling factor estimated from Smith and Sandwell approach (equation (8)), (b) scaling factor estimated from RANSAC algorithm. Gravity and bathymetry were filtered with modified S&S filter $W_m(k)$. In total, 268,105 multibeam samples (500-m spacing) are used in this comparison.

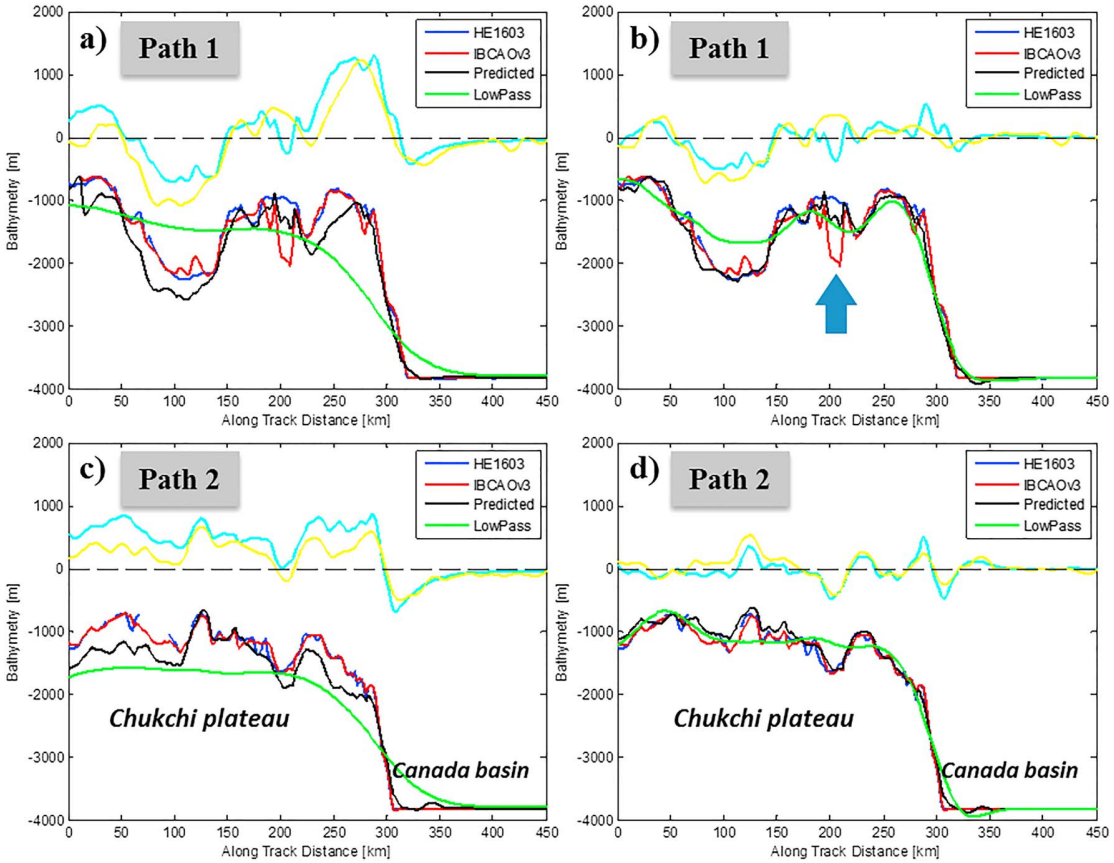

Figure 9. The along-track profiles of Healy cruise path 1 (a, b) and path 2 (c, d). Subfigures (a) and (c) refer to the results from the Smith and Sandwell (1994) filter. Subfigures (b) and (d) refer to the results from the modified filter $W_m(k)$. Blue curve for the HE1603, red curve for the IBCAOv3, black curve for the predicted bathymetry in this study, green curve for the low-pass filtered bathymetry $B_{\text{long}}(x)$, cyan for band-pass-filtered bathymetry, and yellow for the band-pass-filtered gravity which is scaled by scaling factor $S(x)$.

downward continued gravity to deep sea floor of ~4 km, which only resolve larger than 18-km features. Thus, in some wavelengths we do not predict bathymetry. Such large differences were also observed in the southern ocean studies from Smith and Sandwell (1994).

In addition, the comparison with bathymetry predicted using the S&S filter $W(k)$ and its modified version $W_m(k)$ (the main difference is $W_1(k)$ and $W_c(k)$ for the high-pass filtering) is given in Table 1. The predicted bathymetry from the S&S filter gives relatively large differences compared to the modified filter proposed in this study.

4. Validation

The bathymetric sounding surveys can be accessed through NOAA National Centers for Environmental Information (NCEI, formerly NGDC) Bathymetry Data Viewer map services. There are limited amounts of ship soundings conducted after the release of IBCAOv3. Most of the ship sounding multibeam data are collected as part of Extended Continental Shelf (ECS) project and led by scientists from the University of New Hampshire and U.S. Geological Survey. The target region of ECS project is mainly around the Chukchi Cap and only few cruise tracks operated toward the North Pole (Mayer et al., 2016; Mayer & Armstrong, 2012). The differences of ECS compilation and IBCAOv3 give a mean of −11.4 m with a std. of 48.0 m. It is worth to mention that most of the cruises that operated before 2012 have already been incorporated to IBCAOv3. Therefore, only several latest cruises are relatively independent for external validation, for instance, HE1202 (Mayer & Armstrong, 2012) and HE1603 (Mayer et al., 2016).

Table 2
The Statistics of the Differences From Profile Analysis

Profiles	Differece	Mean	Std.	Min	Max
Path 1	HE1603 − $H_p(x)_1$	160.4	195.7	−134.1	731.2
	HE1603 − IBCAOv3	33.9	181.6	−295.8	1012.8
	$H_p(x)_1$ − IBCAOv3	−126.0	243.3	−636.0	677.3
Path 2	HE1603 − $H_p(x)_2$	114.6	182.8	−246.3	531.6
	HE1603 − IBCAOv3	2.3	54.1	−225.8	175.2
	$H_p(x)_2$ − IBCAOv3	−126.3	184.6	−514.6	233.8

Note. Bathymetry prediction results from S&S filter $W(k)$. $H_p(x)_1$ and $H_p(x)_2$ are profiles for paths 1 and 2, respectively. Refer to the profiles in Figures 9a and 9c. Unit: m.

A closer view on the difference of compiled ECS ship sounding compilations (from 2003 to 2016) and our bathymetry estimate to the north of Chukchi Cap is shown in Figure 8. Positive differences indicate that the bathymetry predicted from gravity is deeper than ship soundings, and thus implies that the actual heights of seamount are underestimated (by as much as 400 m). Negative differences indicate that the predicted bathymetry is shallower than ship soundings, ~100 m (mainly over the deep relatively flat basins). In Figure 8, ECS bathymetry compilations are compared to bathymetry resulting from different scaling factor estimation algorithms described in section 2.4. The results from scaling factor $S(x)$ estimated using slope estimator (equation (8)) appear smoother than the results obtained from RANSAC. RANSAC estimator performs better than the slope estimator over a seamount marked by the black arrow. In fact, this is exactly the spot where we demonstrated the scaling factor estimation in Figure 5a. On average, scaling factor estimated from RANSAC is 6.6 m/mGal higher than that estimated from slope estimator. Therefore, more fluctuations are visible on the results obtained from RANSAC (Figure 8b). The mean difference between ECS bathymetry data and bathymetry resulting from slope estimator (refer to Figure 8a) is −11.6 m, with a std. of 71.7 m. It is -13.0 ± 81.0 m for the differences referring to RANSAC in Figure 8b. One should be careful when employing RANSAC algorithm to entire region. We recommended using RANSAC estimator over rugged topography with large variations.

In the following, two profiles taken from Healy cruise multibeam sounding surveys conducted in 2016 (HE1603) are analyzed. Locations of the two profiles are shown in Figure 4c. From south to north, the two paths cross the margin of Chukchi Cap (plateau) at the along-track distance ~300 km as shown in Figure 9. The profiles referring to S&S filter are shown in Figures 9a and 9c, where predicted bathymetry (black curve) deviates as much as 200 m from IBCAOv3 and HE1603 profiles over Chukchi plateau. Such deviations are evident on both profiles of paths 1 and 2. The profiles referring to the modified S&S filter are shown in Figures 9b and 9d. Compared to the results from S&S filter, predicted bathymetry shows good agreement with HE1603 profiles as well as IBCAOv3. No dramatic deviations are observed on both profiles. At the along-track distance ~200 km in Figure 9b, the blue arrow indicates a spot where IBCAOv3 is problematic. At this spot, an ~1,000-m-deep valley was mapped in existing IBCAOv3. However, the ship soundings from HE1603 comply with the bathymetry inverted from gravity at this spot.

The statistics of the profile analysis along the two paths (see locations in Figure 4c) are shown in Tables 2 and 3. When using the S&S filter, both the mean and std. of the differences are large compared to the results from the modified S&S filter. On path 1, standard deviation of differences between HE1603 and predicted bathymetry is 119.5 m, which is 39% improvement to the bathymetry using S&S filter on this profile. Moreover, the mean difference on path 1 is reduced from 160.4 to 50.8 m. Smaller mean difference indicates consistency between predicted bathymetry and HE1603. On path 2, the mean difference is only −36.9 m with a std. of 77.6 m as shown in Table 3. Compared to a std. of 182.8 m from bathymetry using S&S filter, 57% improvement is obtained from bathymetry using modified S&S filter. In particular, the standard deviation of differences between HE1603 and IBCAOv3 on path 1 is 181.6 m. Differences between HE1603 and predicted bathymetry using modified S&S filter yield a std. of 119.5 m, which is 33% improvement to the existing IBCAOv3.

Table 3
The Statistics of the Differences From Profile Analysis

Profiles	Difference	Mean	Std.	Min	Max
Path 1	HE1603 − $H_p(x)_1$	50.8	119.5	−211.9	413.8
	HE1603 − IBCAOv3	33.9	181.6	−295.8	1012.8
	$H_p(x)_1$ − IBCAOv3	−16.9	161.8	−438.6	694.0
Path 2	HE1603 − $H_p(x)_2$	−36.9	77.6	−237.4	202.6
	HE1603 − IBCAOv3	2.3	54.1	−225.8	175.2
	$H_p(x)_2$ − IBCAOv3	51.2	89.2	−233.4	285.5

Note. Bathymetry prediction results from the modified S&S filter $W_m(k)$. $H_p(x)_1$ and $H_p(x)_2$ are profiles for paths 1 and 2, respectively. Refer to the profiles in Figures 9b and 9d. Unit: m.

The profile analysis and validation with independent ship soundings suggest that the modified S&S filter is successful in predicting Arctic Ocean bathymetry from gravity anomalies.

5. Summary

The accuracy of marine gravity in the Arctic Ocean was found to be significantly improved in the DTU17 marine gravity model. The improvement in gravity motivated us to predict bathymetry from gravity anomalies in the Arctic Ocean. In this paper, we presented the first ever Arctic bathymetry predicted from marine gravity. The Smith&Sandwell filter has to

be adjusted for the Arctic to diminish the long wavelength error in the gravity at the high latitudes. Modified version of Smith&Sandwell filter is proposed to overcome the potential long wavelength problem in the Arctic Ocean.

The prediction is only done on grid nodes where the bathymetry and gravity variations are significant. Significant correlation is observed over the Chukchi Cap, along the Gakkel Ridge, Lomonosov Ridge, and the north Atlantic Boreas basins. On most of the shallow water regions and the sedimentary basins, such as Canada basin and Amundsen basin, low or negative correlation between gravity and topography is observed. In such regions, bathymetry is not predicted from gravity.

The scaling factor is an important parameter in predicting bathymetry from gravity. The Smith and Sandwell approach (slope estimator) tends to underestimate the actual seafloor topography. RANSAC algorithm suggested in this study was found to be effective over the rugged topography (e.g., seamounts) and predicted bathymetry is closer to the accurate depth measurements from ship soundings.

Good agreement between the predicted bathymetry and input bathymetry IBCAOv3 is achieved when applying modified Smith&Sandwell filter. Overall, the mean difference is −0.5 m, with a std. of 81.5 m. The validation with compiled ECS bathymetry over the north of Chukchi Cap, and two Healy cruise profiles shows good consistency between the predicted bathymetry and ship soundings. In addition, a questionable valley is detected in the IBCAOv3 through the profile analysis.

The uncertainty in the prediction can be attributed to several factors. First, we inverted the bathymetry with the assumption of constant rock density. However, the sedimentary layers are present all over the Arctic. The sediments cover the subseafloor structures that are the main source of gravity. Thus, the correlation between gravity and bathymetry becomes less significant. Second, the remaining long wavelength error from the gravity model may introduce (bias) error to the predicted bathymetry. Third, different scaling factor estimation techniques give different results. The application of robust linear regression techniques is important for the scaling parameter estimations. Last but not least, the linear approximation of the relationship between gravity and topography may not be sufficient at regions with high (seafloor) topographic relief.

The bathymetry predicted from gravity can be combined with the existing bathymetry soundings to make a new hybrid bathymetry of the Arctic, which will be helpful in filling the data gaps between the sparse ship soundings.

Acknowledgments
We thank the NOAA National Centers for Environmental Information (NCEI) for providing IBCAOv3 and the ship soundings available via https://maps.ngdc.noaa.gov/viewers/bathymetry/. This work is partly supported by ESA "CryoSat Plus for Oceans" (CP4O) project. The predicted arctic bathymetry is available via https://ftp.space.dtu.dk/pub/ArcticBATH/.

References

Alvey, A., Gaina, C., Kusznir, N. J., & Torsvik, T. H. (2008). Integrated crustal thickness mapping and plate reconstructions for the high Arctic. *Earth and Planetary Science Letters*, *274*(3-4), 310–321. https://doi.org/10.1016/j.epsl.2008.07.036

Andersen, O. B., & Knudsen, P. (2019). *The DTU17 global marine gravity field—First validation results*, *International Association of Geodesy Symposia*, (). Berlin, Heidelberg: Springer.

Arndt, J. E., Jokat, W., Dorschel, B., Myklebust, R., Dowdeswell, J. A., & Evans, J. (2015). A new bathymetry of the Northeast Greenland continental shelf: Constraints on glacial and other processes. *Geochemistry, Geophysics, Geosystems*, *16*, 3733–3753. https://doi.org/10.1002/2015GC005931

Bamber, J. L., Griggs, J. A., Hurkmans, R. T. W. L., Dowdeswell, J. A., Gogineni, S. P., Howat, I., et al. (2013). A new bed elevation dataset for Greenland. *The Cryosphere*, *7*, 499–510. https://doi.org/10.5194/tc-7-499-2013

Becker, J. J., Sandwell, D. T., Smith, W. H. F., Braud, J., Binder, B., Depner, J., et al. (2009). Global bathymetry and elevation data at 30 arc seconds resolution: SRTM30_PLUS. *Marine Geodesy*, *32*(4), 355–371. https://doi.org/10.1080/01490410903297766

Cancet, M., Andersen, O. B., Lyard, F., Cotton, D., & Benveniste, J. (2018). Arctide2017, a high-resolution regional tidal model in the Arctic Ocean. *Advances in Space Research*, *62*(6), 1324–1343, ISSN 0273-1177. https://doi.org/10.1016/j.asr.2018.01.007

Døssing, A., Hansen, T. M., Olesen, A. V., Hopper, J. R., & Funck, T. (2014). Gravity inversion predicts the nature of the Amundsen Basin and its continental borderlands near Greenland. *Earth and Planetary Science Letters*, *408*, 132–145. https://doi.org/10.1016/j.epsl.2014.10.011

Engen, Ø., Frazer, L. N., Wessel, P., & Faleide, J. I. (2006). Prediction of sediment thickness in the Norwegian–Greenland Sea from gravity inversion. *Journal of Geophysical Research*, *111*, B11403. https://doi.org/10.1029/2005JB003924

Fischler, M. A., & Bolles, R. C. (1981). Random sample consensus: A paradigm for model fitting with applications to image analysis and automated cartography. *Communications of the ACM*, *24*(6), 381–395.

Gardner, J. V., Mayer, L. A., & Armstrong, A. (2006). Mapping supports potential submission to U.N. Law of the Sea. *Eos Transactions American Geophysical Union*, *87*(16), 157–160. https://doi.org/10.1029/2006EO160002

Glebovsky, V. Y., Astafurova, E. G., Chernykh, A. A., Korneva, M. A., Kaminsky, V. D., & Poselov, V. A. (2013). Thickness of the Earth's crust in the deep Arctic Ocean: Results of a 3D gravity modeling. *Russian Geology and Geophysics*, *54*(3), 247–262.

Jakobsson, M., Grantz, A., Kristoffersen, Y., & Macnab, R. (2003). Physiographic provinces of the Arctic Ocean seafloor. *Geological Society of America Bulletin*, *115*(12), 1443–1455.

Jakobsson, M., Mayer, L., Coakley, B., Dowdeswell, J. A., Forbes, S., Fridman, B., et al. (2012). The International Bathymetric Chart of the Arctic Ocean (IBCAO) Version 3.0. *Geophysical Research Letters*, *39*, L12609. https://doi.org/10.1029/2012GL052219

Kenyon, S., & Forsberg, R. (2008). New gravity field for the Arctic. *Eos, Transactions American Geophysical Union*, *89*(32), 289. https://doi.org/10.1029/2008EO320002

Laske, G., & Masters, G. (1997). A global digital map of sediment thickness. *Eos Transactions American Geophysical Union*, *78*, F483.

Le Brocq, A. M., Payne, A. J., & Vieli, A. (2010). An improved Antarctic dataset for high resolution numerical ice sheet models (ALBMAP v1). *Earth System Science Data*, *2*(2), 247–260. https://doi.org/10.5194/essd-2-247-2010

May, S. D., & Grantz, A. (1990). Sediment thickness in the southern Canada Basin. *Marine Geology*, *93*, 331–347.

Mayer, L. A., & Armstrong, A. (2012). US Law of the Sea cruise to map and sample the US Arctic Ocean margin. University of New Hampshire (UNH), Center for Coastal and Ocean Mapping (CCOM)/Joint Hydrographic Center (JHC)

Mayer, L. A., Calder, B., & Mosher, D. C. (2016). US Law of the Sea cruise to map and sample the US Arctic Ocean margin, Healy 1603. Center for Coastal and Ocean Mapping/Joint Hydrographic Center, University of New Hampshire, Durham, NH

Mayer-Gürr, T., Kvas, A., Klinger, B., Rieser, D., Zehentner, N., Pail, R., et al. (2015). The new combined satellite only model GOCO05s. https://doi.org/10.13140/RG.2.1.4688.6807

McKenzie, D., & Bowin, C. (1976). The relationship between bathymetry and gravity in the Atlantic Ocean. *Journal of Geophysical Research*, *81*(11), 1903–1915. https://doi.org/10.1029/JB081i011p01903

Morlighem, M., Williams, C. N., Rignot, E., An, L., Arndt, J. E., Bamber, J. L., et al. (2017). BedMachine v3: Complete bed topography and ocean bathymetry mapping of Greenland from multibeam echo sounding combined with mass conservation. *Geophysical Research Letters*, *44*, 11,051–11,061. https://doi.org/10.1002/2017GL074954

Pail, R., Fecher, T., Barnes, D., Factor, J. F., Holmes, S. A., Gruber, T., & Zingerle, P. (2018). Short note: The experimental geopotential model XGM2016. *Journal of Geodesy*, *92*, 443–451. https://doi.org/10.1007/s00190-017-1070-6

Parker, R. L. (1973). The rapid calculation of potential anomalies. *Geophysical Journal of the Royal Astronomical Society*, *31*, 447–455. https://doi.org/10.1111/j.1365-246X.1973.tb06513.x

Pavlis, N. K., Holmes, S. A., Kenyon, S. C., & Factor, J. K. (2012). The development and evaluation of the Earth Gravitational Model 2008 (EGM2008). *Journal of Geophysical Research*, *117*, B04406. https://doi.org/10.1029/2011JB008916

Schaffer, J., Timmermann, R., Arndt, J. E., Kristensen, S. S., Mayer, C., & Morlighem, M. (2016). A global, high-resolution data set of ice sheet topography, cavity geometry, and ocean bathymetry. *Earth System Science Data*, *8*(2), 543–557.

Smith, W. H. F., & Sandwell, D. T. (1994). Bathymetric prediction from dense satellite altimetry and sparse shipboard bathymetry. *Journal of Geophysical Research*, *99*(B11), 21,803–21,824. https://doi.org/10.1029/94JB00988

Weatherall, P., Marks, K. M., Jakobsson, M., Schmitt, T., Tani, S., Arndt, J. E., et al. (2015). A new digital bathymetric model of the world's oceans. *Earth and Space Science*, *2*, 331–345. https://doi.org/10.1002/2015EA000107

Wessel, P., & Smith, W. H. (1991). Free software helps map and display data. *Eos, Transactions American Geophysical Union*, *72*(41), 441–446.

Wessel, P., Smith, W. H., Scharroo, R., Luis, J., & Wobbe, F. (2013). Generic mapping tools: improved version released. *Eos, Transactions American Geophysical Union*, *94*(45), 409–410.

Wessel, P., & Smith, W. H. F. (1996). A global, self-consistent, hierarchical, high-resolution shoreline database. *Journal of Geophysical Research*, *101*(B4), 8741–8743. https://doi.org/10.1029/96JB00104

C.2 Coastal marine gravity modelling from satellite altimetry – Case study in the Mediterranean

Conference proceedings for Gravity, Geoid and Height Systems 2 (GGHS) 2018 held in Copenhagen, Denmark. Paper accepted for publication in *Journal of Geodetic Science*. First submitted on 30 November 2018. Accepted on 26 April 2019.

Research Article Open Access

Adili Abulaitijiang*, Ole Baltazar Andersen, Riccardo Barzaghi, and Per Knudsen

Coastal marine gravity modelling from satellite altimetry – case study in the Mediterranean

DOI: DOI
Received ..; revised ..; accepted ..

Abstract: The coastal marine gravity field is not well modelled due to poor data coverage. Recent satellite altimeters provide reliable altimetry observations near the coast, filling the gaps between the open ocean and land. We show the potential of recent satellite altimetry for the coastal marine gravity modelling using the least squares collocation technique. Gravity prediction error near the coast is better than 4 mGal. The modelled gravity anomalies are validated with sparse shipborne gravimetric measurements. We obtained 4.86 mGal precision when using the altimetry data with the best coastal coverage and retracked with narrow primary peak retracker. The predicted gravity field is an enhancement to EGM2008 over the coastal regions. The potential improvement in altimetric marine gravity will be beneficial for the next generation of EGM development.

Keywords: Coastal marine gravity, Least squares collocation, Satellite altimetry

1 Introduction

Marine gravity anomalies are of great importance for studying the Earth's tectonic structure and ocean bathymetry [1–5]. Satellite altimetry measurements are the main source in recovering short wavelength components of the marine gravity field. The traditional altimetry (footprint larger than 10 km) can only reach up to 30 km away from the coast leaving a data gap near the shore. Since the launch of CryoSat-2 in 2010 [6], with the novel Synthetic Aperture Radar (SAR) mode, we can obtain reliable altimetry data benefiting from the high along track resolution (only ∼300 m). SARAL/Altika [7] has smaller footprint and higher range precision than the conventional Ku-band radar altimeters. Therefore, limiting the data gap is possible with a combination of recent altimetry satellites like CryoSat-2 and SARAL/Altika.

The development of marine gravity field requires better altimetric range precision and data coverage. The improved range precision can be achieved by optimal retracking methods. Hwang et al. [8] highlighted the importance of retracking methods in the coastal marine gravity field modelling around Taiwan. Studies show great improvement in coastal altimetric products by optimized data processing strategy [9–11]. Passaro et al. [12, 13] developed adapted waveform retrackers that perform well both for the oceans and coastal waveforms.

Andersen and Kundsen [14] highlighted the role of satellite altimetry in the gravity modelling using the Geosat and ERS-1 geodetic missions and compared the altimeter-derived gravity anomalies with marine and airborne gravimetric measurements in coastal regions characterized by the narrow continental shelf and shallow water areas, respectively. However, its ability degraded within roughly 10 km of the coast. Hirt [15, 16] investigated the role of topography/bathymetry model in gravity field determination in coastal zones, and showed that the bathymetry data were beneficial for filling the gap between terrestrial and shipborne gravity data. Although CryoSat-2 showed great potential for coastal mean dynamic topography (MDT) modelling [17], coastal geoid determination remains problematic in some areas due to the poor data coverage between land and open ocean areas.

In this paper, we show the potential of marine gravity modelling near the coastal zones from recent satellite altimetry. The Least Squares Collocation (LSC) method is used for the derivation of gravity anomalies from the measured sea surface heights. Residual Terrain Modelling (RTM) is considered in the modelling process. For CryoSat-2, three different altimetry datasets are used to examine the effect of waveform retrackers in marine gravity modelling. In the final step, the predicted gravity anomalies are validated against shipborne measurements and EGM2008.

***Corresponding Author: Adili Abulaitijiang:** DTU Space, Technical University of Denmark, Lyngby, DK-2800, Denmark, E-mail: adili@space.dtu.dk
Ole Baltazar Andersen: DTU Space, Technical University of Denmark, Lyngby, DK-2800, Denmark
Riccardo Barzaghi: Politecnico di Milano, Milan, Italy
Per Knudsen: DTU Space, Technical University of Denmark, Lyngby, DK-2800, Denmark

2 Methods

We model the coastal gravity field within the framework of remove-compute-restore (RCR) methodology [18–20].

The altimetry measurements, Sea Surface Heights (SSH) can be split into several components as follows

$$SSH = N^{EGM} + N_r + \mathrm{MDT}^{EGM} + N^{RTM} + \epsilon(t) + e \quad (1)$$

where N^{EGM} is geoid height from an Earth Gravitational Model (EGM), MDT^{EGM} is the mean dynamic topography associated with EGM, N_r is the residual height anomaly, N^{RTM} is contribution from topography, $\epsilon(t)$ is the time dependent components that can be diminished by post processing procedures such as the cross-over adjustment [21], e is the error term remaining in the data.

In the remove step, the EGM geoid height, MDT and contributions from Residual Terrain Modelling (RTM) are removed from the original data to reduce the signal. We choose EGM2008 [22] as the reference model. The MDT model associated with EGM2008 has a maximum spherical harmonic degree and order (d/o) 180. The RTM [23, 24] is considered for reducing the height anomalies, which accounts for the local features that have the shorter wavelengths than that of EGM removed earlier. As for the detailed terrain model, SRTM (Shuttle Radar Topography Missions) (3"×3") and GEBCO (General Bathymetric Chart of the Oceans) (30"×30") are combined to derive a uniform digital terrain model (DTM) with a spatial resolution of 3"×3" over land and ocean. The cross-over adjustment follows right after the RTM approach.

After the signal reduction and cross-over adjustment procedures, we have the "clean" residual height anomalies N_r, and only the residual gravity field is modelled in the computation step. Two techniques can be used to convert the height anomalies to gravity anomalies, which are the Fast Fourier Transform (FFT) method [18, 25] and Least Squares Collocation (LSC) method [23, 26, 27]. The advantage of LSC is that it can handle heterogeneous observations and the observations are not necessarily gridded as in the case of FFT. Moreover, LSC provides the error estimates of the predicted signal quantity. The disadvantage of LSC is that it requires intensive computational power, as the size of the normal equation increases with the number of observations.

In its simplest form, the LSC can be represented in the form of

$$\Delta g = C_{(\Delta g,h)} \left[C_{(\Delta g,h)} + D_{(h,h)} \right]^{-1} h \quad (2)$$

where $C_{(.)}$ denotes the covariance function, $D_{(.)}$ denotes the noise variance of the observations h. h in the equation refers to the residual height anomaly N_r in Eq.(1)

The covariance function modelling is a crucial step in the LSC. A covariance model is fitted to the empirical covariance estimates [28] from the observations. There are several covariance models available, e.g.,[29–31] , but the model proposed by Tscherning and Rapp [32] is sufficient in our modelling. The covariance of the anomalous potential T between the two points $P(\phi, \lambda, r)$ and $Q(\phi', \lambda', r')$ is given by

$$\begin{aligned} \mathrm{Cov}\{T_P, T_Q\} = \alpha \sum_{n=2}^{1080} \left(\sigma_n^{ERR}\right)^2 \left(\frac{R^2}{rr'}\right)^{n+1} P_n(\cos\psi) \\ + \sum_{n=1081}^{\infty} \left(\sigma_n^{TR}\right)^2 \left(\frac{R^2}{rr'}\right)^{n+1} P_n(\cos\psi) \end{aligned} \quad (3)$$

where α is the scaling parameter to be estimated, $\left(\sigma_n^{ERR}\right)^2$ are the error degree variances from the EGM2008 model, $\left(\sigma_n^{TR}\right)^2$ are the degree variance model proposed by Tscherning and Rapp, R is the mean earth radius, $P_n(\cos\psi)$ is the Legendre polynomials with ψ being the spherical distance between the two points.

In the restore step, we need to add back what we have removed. Specifically, the reference gravity anomalies from EGM2008 and RTM gravity anomalies are computed and added to the predicted gravity anomalies from LSC (or FFT). Thus, the full wavelength marine gravity is attained by the RCR approach.

3 Coastal marine gravity modelling

Since we are working on the coastal zone, the altimetry tracks terminate near the coastline. Hence, gridding of the altimetry data is not recommended. Therefore, the FFT method is not considered in this work. We make use of the along track data which are non-uniformly scattered and unstacked.

So far we have 8 years of CryoSat-2 data available, but using all the altimetry observations yield large covariance matrix, which is hard to invert in LSC. Data downsampling(or thinning) is an option, but the behaviour of empirical covariances also changes before and after downsampling. For the altimetry data we use two years (2014 and 2015) of CryoSat-2, one year of SARAL/Altika drifting phase and one year of Jason-1 geodetic mission data for the modelling. The precision of observations from different satellite missions are slightly different. For instance, Jason-1, a traditional Ku-band radar altimeter, has a large footprint and 6∼7 cm range precision [33],

while the Ka-band SARAL/Altika has the 3∼4 cm range precision [34], which is similar to the CryoSat-2 SAR mode observations. Jason-1 has a 66° orbit inclination while the other two satellite have near polar orbits. The inclusion of Jason-1 data is important as it provides more inter-satellite cross-over points in a small region, which is beneficial for the cross-over adjustment.

The RTM is conducted by prism integration [24]. The terrain correction (TC), cross-over adjustment (CRSADJ), empirical covariance estimation (EMPCOV),covariance fitting (COVFIT), geodetic collocation (GEOCOL) modules from GRAVSOFT package [35] are extensively used for the marine gravity modelling.

For the study area, we selected the north of Sicily island with geodetic boundaries $13.5° < \lambda < 16.2°$ and $38° < \varphi < 40.2°$. The Aeolian Islands in the Tyrrhenian Sea are located in the center of tested area which is bounded by the Italian Peninsula on the east. The area spans more than 200 km in both latitude and longitude direction. CryoSat-2 operates in the SAR mode in the study area.

3.1 Data preparation

CryoSat-2 data can be obtained from several sources. Firstly, the altimetry data is extracted from Radar Altimeter Database System (RADS)[36]. It is a database for all types of altimetry missions. The CryoSat-2 SAR mode acquisitions are processed by a technique called ReducedSAR (RDSAR)[37] in the RADS database. Secondly, we use the Lars Altimetry Retracking System (LARS) altimetry database developed at DTU, where CryoSat-2 waveforms are retracked with different empirical retrackers. For the LARS data, we choose the narrow primary peak retracker[38] that produces SSHs with the least along track noise (meaning better range precision). Last but not least, we ordered CryoSat-2 data from Grid Processing On Demand (GPOD) service (https://gpod.eo.esa.int/) maintained by European Space Agency (ESA). In RADS, the waveforms are retracked with a modified Brown retracker [39], while a physical retracker dedicated for the coastal areas, i.e.,SAMOSA+ [40] is employed in the GPOD service. The GPOD data has the best height precision (<2 cm) than the other two datasets. Moreover, the Jason-1 and SARAL/Altika data are extracted from RADS only. CryoSat-2 observations retrieved from three different datasets are merged with SARAL/Altika and Jason-1 data and the combined datasets are identified by the names RADS, LARS and GPOD in the following. Only 1-Hz observations are used for marine gravity modelling.

We initially tested the altimetry data (SSHs) from RADS and removed the EGM2008 geoid heights up to d/o 2190 and MDT associated with EGM2008. The residual height anomalies after cross-over adjustment are shown in Fig.1 along with the empirical covariance estimates. The residual signal remaining after removing the EGM2008 (d/o 2190) is so small with a standard deviation (std.) of 0.038 m. When removing the full resolution EGM2008 model, the signal-to-noise ratio (SNR) in the residual field is so small and it will be hard to fit a proper covariance model as shown in Fig.1b.

In this study, we intentionally preserve some signal from the EGM2008 model to increase the SNR in the residual height anomalies. Hence, we reduce the maximum spherical harmonic degree of the EGM2008 model to 1080. The shortest half-wavelength of the reference EGM2008 (d/o 1080) is around 20 km (10 arc-minute resolution). The wavelength is still smaller than the extent of the region (∼200 km).

The RADS residual height anomalies after removing EGM2008 (d/o 1080) and MDT with and without RTM effects are shown in Fig.2. The RTM effects are supposed to reduce the residual signal, but the residual signal is partly "enhanced" by subtracting the RTM contributions. Outside the ellipse in Fig.2b, the residual height anomalies are indeed reduced by removing RTM effects. Inside the ellipse, the signal is stronger and longer wavelength features can be observed. The bathymetry is mostly deep (∼ 3500 m) and flat in the area bounded by the ellipse. The additional signal also distorts the empirical covariance estimates. In Fig.2c, the correlation length of height anomalies with N^{RTM} removed (red curve) is apparently longer than that without removing N^{RTM} (blue curve). The long wavelength features introduced by removing N^{RTM} make it hard to fit the Tscherning&Rapp covariance model as well. Hence, we proceed without removing (or restoring) the RTM contributions in this study.

The height anomalies after the cross-over adjustment for RADS, LARS and GPOD data are shown in Fig.3. We can observe that the LARS and GPOD data are closer to the coastal lines than the RADS data and have slightly more observations. The statistics of the height anomalies are shown in Table 1.

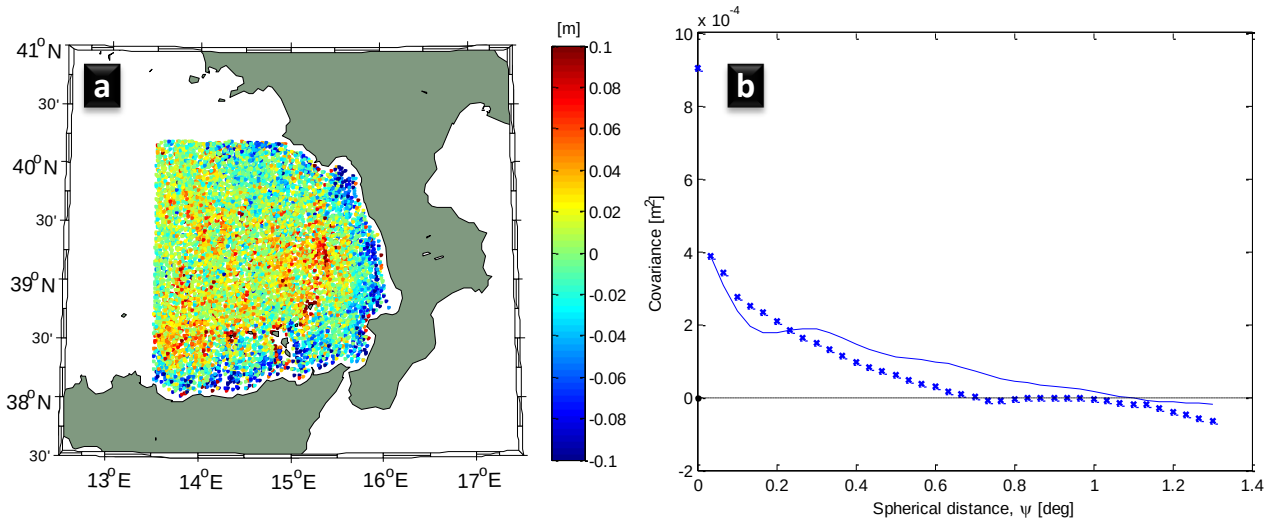

Fig. 1. (a) Residual height anomaly after cross-over adjustment for only removing the EGM2008 model (d/o 2190). (b) empirical covariance (* symbols) and Tscherning&Rapp covariance model fitting (curved lines).

Table 1. Statistic of residual height anomalies after cross-over adjustment. Unit: m

Database	# obs.	mean	std.	min	max
RADS	9471	0.003	0.059	-0.460	0.265
LARS	10304	0.003	0.061	-0.282	0.343
GPOD	9896	0.003	0.059	-0.289	0.304

3.2 Empirical covariance and covariance modelling

The empirical covariances are modelled with EMPCOV module from GRAVSOFT package. For the covariance modelling, the variance term estimated by EMPCOV is excluded, due to the fact that it contains both the signal and noise, and sometimes the signal is insignificant (or very low signal-to-noise ratio). The covariance model fit to the empirical covariances are shown in Fig.4. In general, the Tscherning&Rapp covariance model fits well with the discrete empirical covariances at the short wavelengths. We can also observe the correlation length of altimetry data, which is around 0.1° spherical distance (approx. 10 km resolution).

3.3 Gravity anomalies from LSC and Validation

The GEOCOL19 program with parallel processing option[41] is used to derive the marine gravity anomalies along the shipborne gravity measurements from Morelli cruises[42] and Bureau Gravimétrique International (BGI) database. The shipborne measurements are post-processed and downsampled to a 7.5" grid cells for the purpose of Mediterranean gravimetric geoid modelling (see GEOMED2 project for details [43]). To save the computation time, we further downsampled by a factor of four and get 2264 samples in the study area. The data will be used for the validations later.

The output from LSC is the residual gravity anomalies. The error estimates of the predictions have a median value of 2.38, 2.35 and 2.28 mGal for RADS, LARS and GPOD data, respectively. The prediction error near the coastal lines tends to be higher due to the sparse altimetry observations. On almost all prediction points, the prediction error is smaller than 4 mGal for LARS and GPOD data, which is significantly better than Sandwell gravity field V23.1 [44] errors in the same coastal region.

We restore the full gravity signal by adding the EGM2008 gravity anomalies (d/o 1080) to the residual gravity anomalies predicted from LSC. Then, a direct comparison with shipborne measurements can be conducted. The statistics comparing predicted gravity, EGM2008 and shipborne measurements are shown in Table 2. Note that the EGM2008 and ship gravity are not error-free. The standard deviations of the differences reflects the relative precision of the predicted gravity anomalies. The altimetric gravity anomalies agree with ship measurements with a std. of 5.05, 4.86 and 5.03 mGal, respectively. The difference of ship measurements and EGM2008 has a std. of 5.13 mGal. By using altimetry for marine gravity modelling, we get minor im-

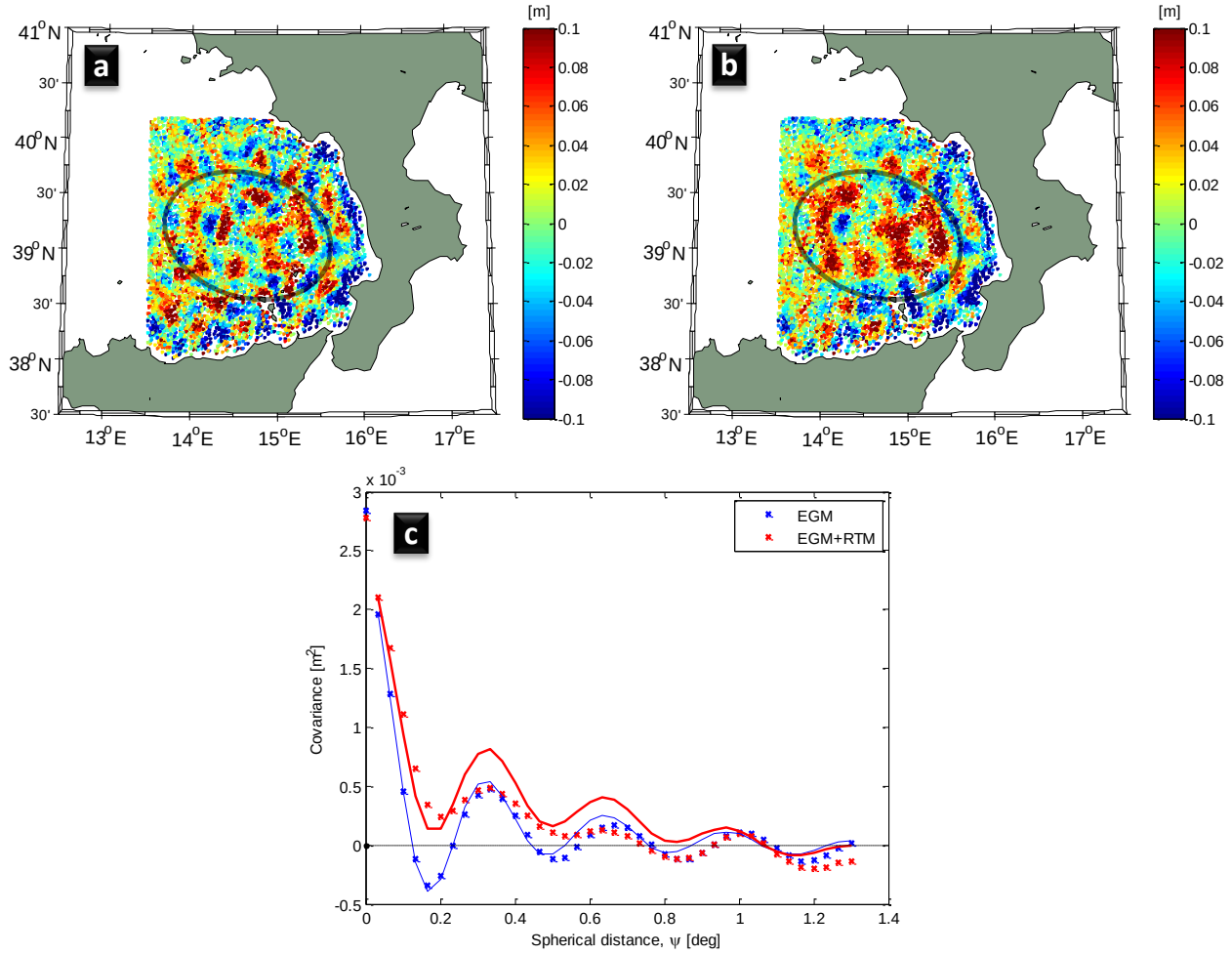

Fig. 2. Residual height anomaly from RADS dataset after cross-over adjustment (a) for only removing the EGM2008 (d/o 1080) (b) for removing the EGM2008 (d/o 1080) and also RTM effects (c) empirical covariance (* symbols) and Tscherning&Rapp covariance model fitting (curved lines). The blue curves refers to (a) while the red curves refers to (b). The area bounded by ellipse has deep and flat bathymetry.

provement. The relative precision of altimetric gravity anomalies compared to EGM2008 is 3.50, 3.36 and 3.48 mGal, respectively. In both cross-comparisons, the gravity anomalies predicted from LARS altimetry database have the best relative precision.

The residuals of predicted gravity anomalies (from LARS data) and EGM2008 are shown in Fig.5. The shipborne gravity samples are divided into "Coastal area" and "Open sea" based on the distance to the closest shorelines. We have 347 samples that are located within 15 km distance from land or islands. The rest are "Open sea" samples. The difference between gravity anomalies predicted from recent altimetry data (LARS) and shipborne gravity surveys are shown in Fig.6. We compare the predicted gravity field and EGM2008 against shipborne gravity. As shown in Table 2, in coastal areas, the std. is reduced from 6.63 mGal to 5.91 mGal, which is 11% improvement. In the open oceans, the improvement is smaller (only 4%).

We assume the error sources are independent between EGM2008, shipborne gravity and predicted gravity anomalies. Thus, we can estimate the precision of the individual dataset through error propagation. This may not be a fair assumption as the gravity data or old altimetric gravity anomalies are integrated to the development of EGM2008. Take the gravity anomalies estimated from recent altimetry data (LARS) as an example. The standard deviation of the predicted gravity anomalies is $\sigma^{LARS} = 2.07$ mGal. The error in the EGM2008 and ship measurements are $\sigma^{EGM} = 2.64$ mGal and $\sigma^{Ship} = 4.39$ mGal, respectively. The estimates suggest that the shipborne measurements are not optimal for assessing the accuracy of the predicted gravity anomalies. Nevertheless,

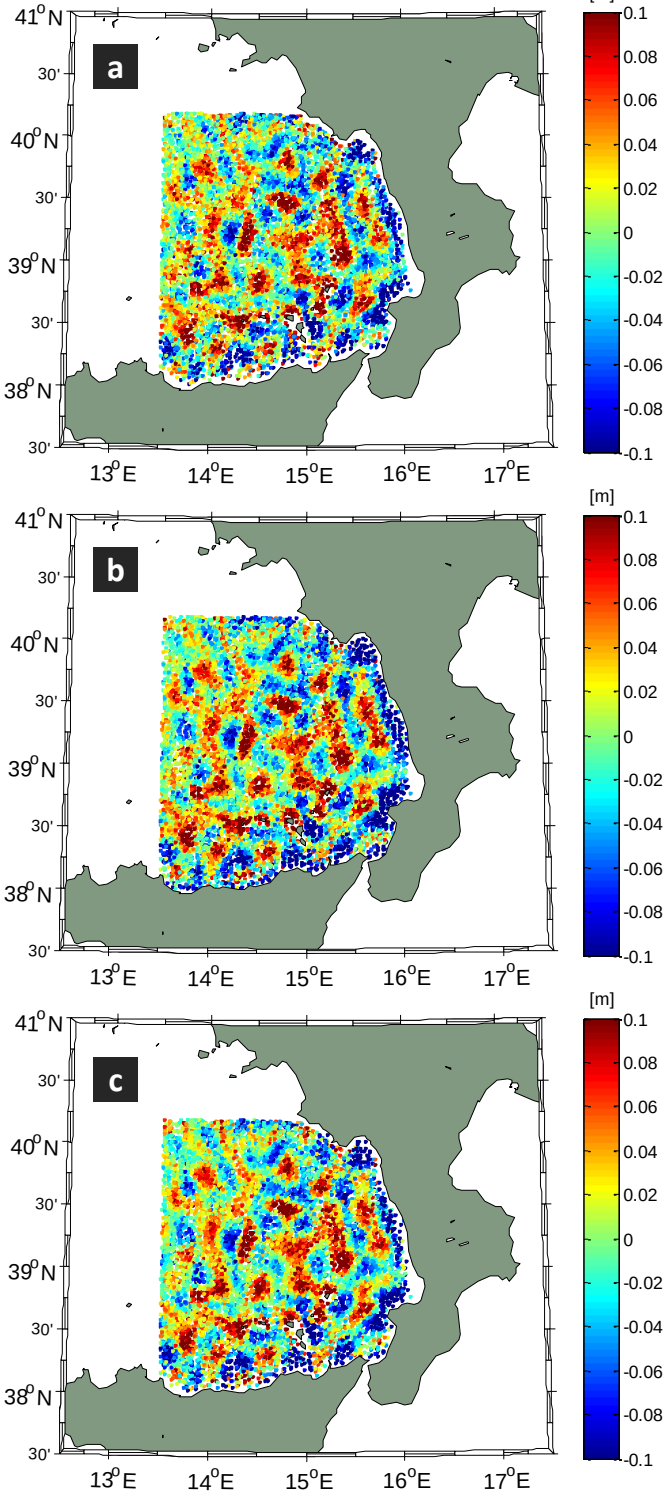

Fig. 3. Residual height anomaly after cross-over adjustment (a) RADS (b) LARS (c) GPOD. Only EGM2008 (d/o 1080) is removed.

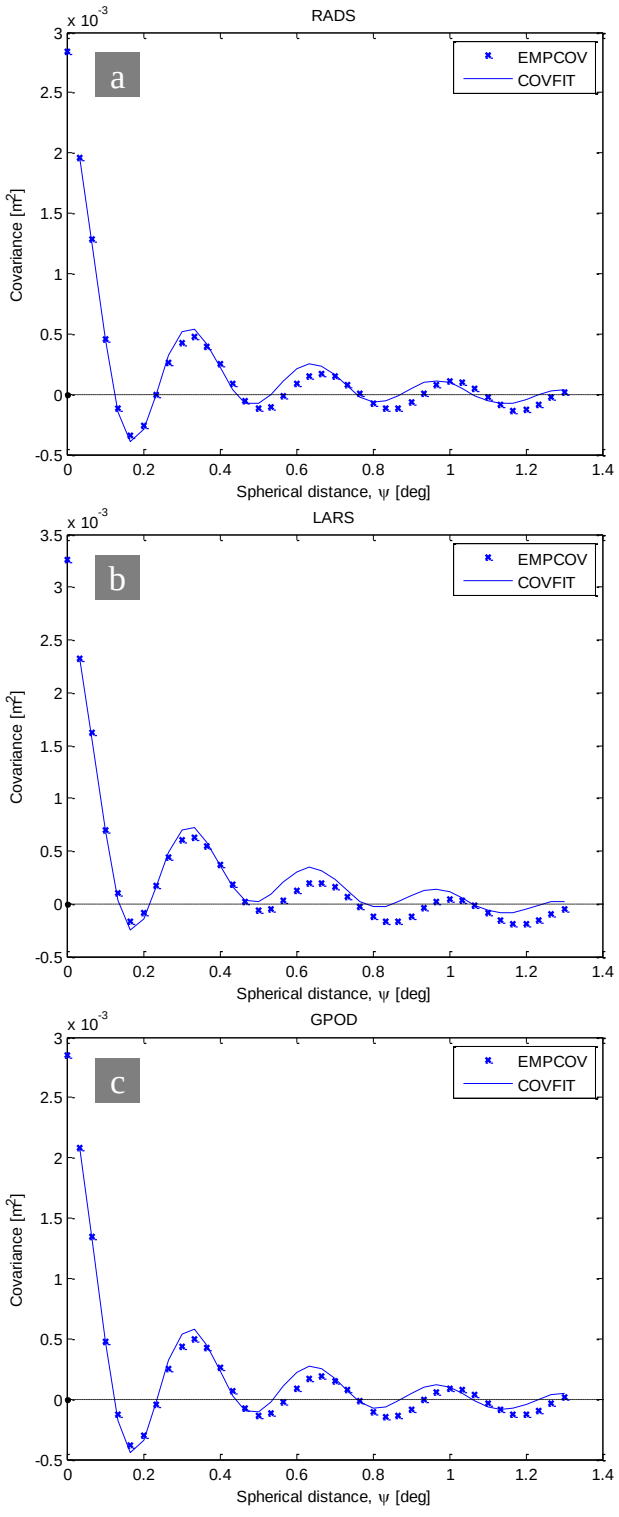

Fig. 4. Empirical covariances (* symbols) and covariance model fits (blue continuous curves) for residual height anomalies shown in Fig.3 (a) RADS (b) LARS (c) GPOD.

Table 2. Statistic of the difference between predicted gravity anomalies from 3 different datasets, shipborne gravimetry $\triangle g^{Ship}$ and EGM2008, in total 2264 samples. Based on the distance away from the nearest coastal line (15 km), 347 samples are located in the "Coastal area". The other 1917 points are used as "Open sea" samples. Unit: mGal

		mean	std.	min	max
All samples	$\triangle g^{RADS}$ **Vs.** $\triangle g^{EGM}$	0.21	3.50	-15.6	14.5
	$\triangle g^{LARS}$ **Vs.** $\triangle g^{EGM}$	0.41	3.36	-16.8	20.1
	$\triangle g^{GPOD}$ **Vs.** $\triangle g^{EGM}$	0.26	3.48	-20.8	14.9
	$\triangle g^{Ship}$ **Vs.** $\triangle g^{EGM}$	0.50	5.13	-18.5	78.9
	$\triangle g^{RADS}$ **Vs.** $\triangle g^{Ship}$	-0.38	5.05	-79.7	24.8
	$\triangle g^{LARS}$ **Vs.** $\triangle g^{Ship}$	-0.18	4.86	-78.7	18.7
	$\triangle g^{GPOD}$ **Vs.** $\triangle g^{Ship}$	-0.33	5.03	-79.6	19.5
Coastal area (<15 km)	$\triangle g^{RADS}$ **Vs.** $\triangle g^{EGM}$	0.74	5.69	-14.7	14.5
	$\triangle g^{LARS}$ **Vs.** $\triangle g^{EGM}$	1.02	5.47	-16.8	20.1
	$\triangle g^{GPOD}$ **Vs.** $\triangle g^{EGM}$	0.47	5.81	-20.8	14.9
	$\triangle g^{Ship}$ **Vs.** $\triangle g^{EGM}$	-0.85	6.63	-18.5	33.5
	$\triangle g^{RADS}$ **Vs.** $\triangle g^{Ship}$	1.45	6.54	-20.1	24.8
	$\triangle g^{LARS}$ **Vs.** $\triangle g^{Ship}$	1.73	5.91	-21.9	18.7
	$\triangle g^{GPOD}$ **Vs.** $\triangle g^{Ship}$	1.18	6.61	-21.3	19.5
Open sea (>15 km)	$\triangle g^{RADS}$ **Vs.** $\triangle g^{EGM}$	0.11	2.93	-15.6	10.4
	$\triangle g^{LARS}$ **Vs.** $\triangle g^{EGM}$	0.30	2.81	-11.6	10.2
	$\triangle g^{GPOD}$ **Vs.** $\triangle g^{EGM}$	0.22	2.86	-11.6	11.2
	$\triangle g^{Ship}$ **Vs.** $\triangle g^{EGM}$	0.74	4.77	-18.2	78.9
	$\triangle g^{RADS}$ **Vs.** $\triangle g^{Ship}$	-0.72	4.66	-79.7	15.3
	$\triangle g^{LARS}$ **Vs.** $\triangle g^{Ship}$	-0.53	4.56	-78.7	18.1
	$\triangle g^{GPOD}$ **Vs.** $\triangle g^{Ship}$	-0.61	4.64	-79.6	18.1

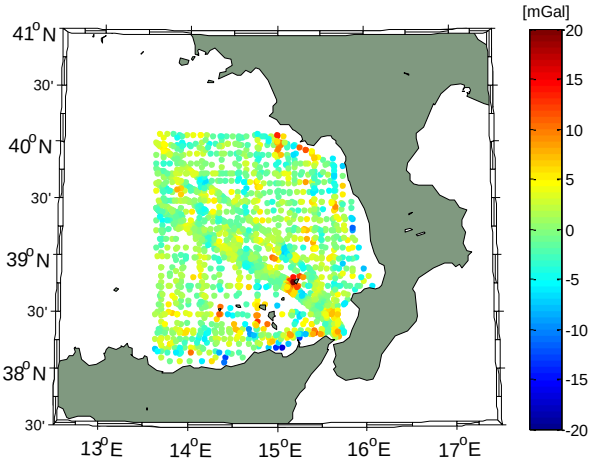

Fig. 5. Difference of LARS altimetric gravity anomalies and EGM2008 over the shipborne survey locations. In total, 2264 samples.

in this region, 2.07 mGal of error in the altimetric gravity anomalies is quite encouraging.

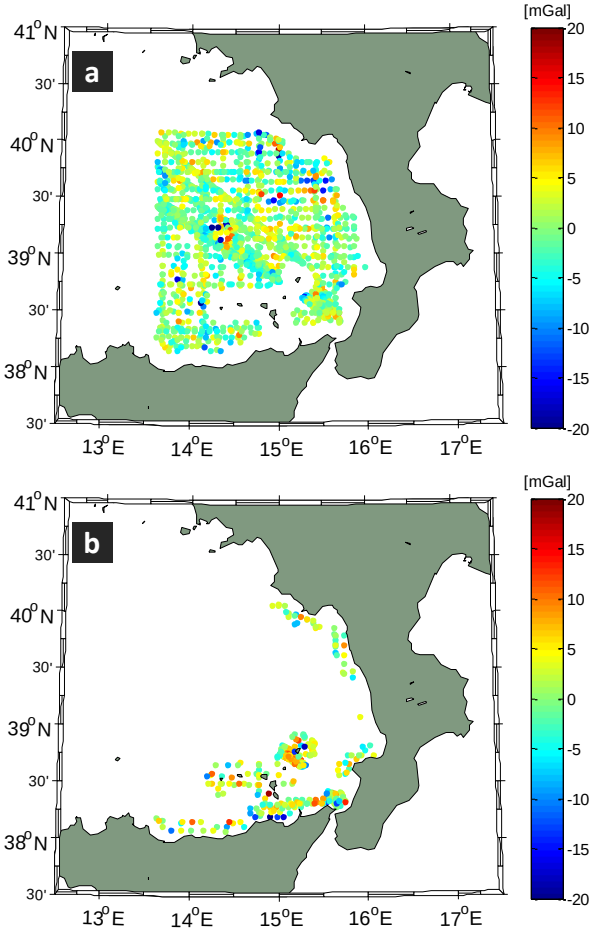

Fig. 6. Difference of (LARS) altimetric gravity anomalies and shipborne gravity (a) over the open ocean (std.=4.56 mGal), (b) in the coastal area (std.=5.91 mGal). Most of the "coastal area" samples are located around the Aeolian islands and north of Sicily island.

4 Summary

Altimetry data from CryoSat-2, SARAL/Altika and Jason-1 geodetic missions are valuable for improving marine gravity not only over the open oceans, but also near the coast. In this study, we showed the potential of recent satellite altimetry in modelling the coastal marine gravity. In the test area north of Sicily island in the Mediterranean Sea, the RTM signal reduction is effective near the coastal relief but not in the deep bathymetric part in the center of study area. The deep water areas likely have sediments that buried the subseafloor structures associated with gravity. Hence, we proceeded without considering RTM contributions in this study.

Gravity field predicted from altimetry data with the most coastal coverage and retracked with the narrow pri-

mary peak retracker gives the best precision of 2.07 mGal. Gravity prediction error from LSC is less than 4 mGal near the coast. The standard deviation is 4.86 mGal when predicted gravity anomalies are compared to shipborne gravity used for GEOMED2 project. This is slightly better than a std. of 5.13 mGal between shipborne gravity and EGM2008. Residual gravity field with respect to EGM2008 is an enhancement to EGM2008. In particular, we got 11% improvement in the coastal area. DTU marine gravity models with improvements in the coastal zones will be incorporated to the next generation of EGM, e.g., EGM2020, in the future.

5 Acknowledgements

The authors would like to thank two anonymous reviewers for their constructive comments and discussions. We acknowledge the processed altimetry data from RADS, LARS database and ESA GPOD service. The ICGEM service provided geoid and gravity anomalies up to desired d/o from EGM2008. We thank GEOMED2 project for providing the shipborne gravity measurements for validations.

References

[1] Parker R. The rapid calculation of potential anomalies. Geophysical Journal of the Royal Astronomical Society. 1973;31(4):447–455.

[2] Døssing A, Hansen TM, Olesen AV, Hopper J, Funck T. Gravity inversion predicts the nature of the Amundsen Basin and its continental borderlands near Greenland. Earth and Planetary Science Letters. 2014;408:132–145.

[3] Engen Ø, Frazer LN, Wessel P, Faleide JI. Prediction of sediment thickness in the Norwegian–Greenland Sea from gravity inversion. Journal of Geophysical Research: Solid Earth. 2006;111(B11).

[4] Smith WHF, Sandwell DT. Bathymetric prediction from dense satellite altimetry and sparse shipboard bathymetry. Journal of Geophysical Research: Solid Earth. 1994;99(B11):21803–21824. Available from: https://agupubs.onlinelibrary.wiley.com/doi/abs/10.1029/94JB00988.

[5] Sandwell DT, Müller RD, Smith WHF, Garcia E, Francis R. New global marine gravity model from CryoSat-2 and Jason-1 reveals buried tectonic structure. Science. 2014;346(6205):65–67. Available from: http://science.sciencemag.org/content/346/6205/65.

[6] Wingham D, Francis C, Baker S, Bouzinac C, Brockley D, Cullen R, et al. CryoSat: A mission to determine the fluctuations in Earth's land and marine ice fields. Advances in Space Research. 2006;37(4):841–871.

[7] Verron J, Sengenes P, Lambin J, Noubel J, Steunou N, Guillot A, et al. The SARAL/AltiKa altimetry satellite mission. Marine Geodesy. 2015;38(sup1):2–21.

[8] Hwang C, Guo J, Deng X, Hsu HY, Liu Y. Coastal gravity anomalies from retracked Geosat/GM altimetry: improvement, limitation and the role of airborne gravity data. Journal of Geodesy. 2006;80(4):204–216.

[9] Vignudelli S, Cipollini P, Roblou L, Lyard F, Gasparini GP, Manzella G, et al. Improved satellite altimetry in coastal systems: Case study of the Corsica Channel (Mediterranean Sea). Geophysical Research Letters. 2005;32(7). Available from: https://agupubs.onlinelibrary.wiley.com/doi/abs/10.1029/2005GL022602.

[10] Bouffard J, Vignudelli S, Cipollini P, Menard Y. Exploiting the potential of an improved multimission altimetric data set over the coastal ocean. Geophysical Research Letters. 2008;35(10). Available from: https://agupubs.onlinelibrary.wiley.com/doi/abs/10.1029/2008GL033488.

[11] Gommenginger C, Thibaut P, Fenoglio-Marc L, Quartly G, Deng X, Gómez-Enri J, et al. Retracking altimeter waveforms near the coasts. In: Coastal altimetry. Springer; 2011. p. 61–101.

[12] Passaro M, Cipollini P, Vignudelli S, Quartly GD, Snaith HM. ALES: A multi-mission adaptive subwaveform retracker for coastal and open ocean altimetry. Remote Sensing of Environment. 2014;145:173–189.

[13] Passaro M, Rose SK, Andersen OB, Boergens E, Calafat FM, Dettmering D, et al. ALES+: Adapting a homogenous ocean retracker for satellite altimetry to sea ice leads, coastal and inland waters. Remote Sensing of Environment. 2018;211:456–471.

[14] Andersen OB, Knudsen P. The role of satellite altimetry in gravity field modelling in coastal areas. Physics and Chemistry of the Earth, Part A: Solid Earth and Geodesy. 2000;25(1):17–24.

[15] Hirt C. Prediction of vertical deflections from high-degree spherical harmonic synthesis and residual terrain model data. Journal of Geodesy. 2010;84(3):179–190.

[16] Hirt C. RTM gravity forward-modeling using topography/bathymetry data to improve high-degree global geopotential models in the coastal zone. Marine Geodesy. 2013;36(2):183–202.

[17] Idžanović M, Ophaug V, Andersen OB. The coastal mean dynamic topography in Norway observed by CryoSat-2 and GOCE. Geophysical Research Letters. 2017;44(11):5609–5617.

[18] Schwarz K, Sideris M, Forsberg R. The use of FFT techniques in physical geodesy. Geophysical Journal International. 1990;100(3):485–514.

[19] Sjöberg L. A discussion on the approximations made in the practical implementation of the remove–compute–restore technique in regional geoid modelling. Journal of Geodesy. 2005;78(11-12):645–653.

[20] Omang O, Forsberg R. How to handle topography in practical geoid determination: three examples. Journal of Geodesy. 2000;74(6):458–466.

[21] Knudsen P, Brovelli M. Collinear and cross-over adjustment of Geosat ERM and Seasat altimeter data in the Mediterranean Sea. Surveys in geophysics. 1993;14(4-5):449–459.

[22] Pavlis NK, Holmes SA, Kenyon SC, Factor JK. The development and evaluation of the Earth Gravitational Model 2008 (EGM2008). Journal of Geophysical Research: Solid Earth. 2012;117(B4):1–38. Available from: https://agupubs.onlinelibrary.wiley.com/doi/abs/10.1029/2011JB008916.

[23] Forsberg R, Tscherning CC. The use of height data in gravity field approximation by collocation. Journal of Geophysical Research: Solid Earth. 1981;86(B9):7843–7854.

[24] Forsberg R. A study of terrain reductions, density anomalies and geophysical inversion methods in gravity field modelling. Ohio State Univ Columbus Dept Of Geodetic Science and Surveying, Report No 355; 1984.

[25] Forsberg R, Sideris M. Geoid computations by the multi-band spherical FFT approach. Manuscripta geodaetica. 1993;18:82–82.

[26] Moritz H. Least-squares collocation. Reviews of Geophysics. 1978;16(3):421–430. Available from: https://agupubs.onlinelibrary.wiley.com/doi/abs/10.1029/RG016i003p00421.

[27] Basic T, Rapp R. Oceanwide prediction of gravity anomalies and sea surface heights using Geos-3, Seasat, and Geosat altimeter data and ETOPO5U bathymetric data. Department of Geodetic Science and Surveying, The Ohio State University, Report No 416; 1992.

[28] Knudsen P. Estimation and modelling of the local empirical covariance function using gravity and satellite altimeter data. Bulletin Geodesique. 1987;61(2):145–160.

[29] Jordan SK. Self-consistent statistical models for the gravity anomaly, vertical deflections, and undulation of the geoid. Journal of Geophysical Research. 1972;77(20):3660–3670.

[30] Kearsley W. Non-Stationary Estimation in Gravity Prediction Problems. Department of Geodetic Science and Surveying, The Ohio State University, Report No 256; 1977.

[31] Duquenne H, Everaerts M, Lambot P. Merging a gravimetric model of the geoid with GPS/levelling data: an example in Belgium. In: Gravity, Geoid and Space Missions. Springer; 2005. p. 131–136.

[32] Tscherning CC, Rapp RH. Closed Covariance Expressions for Gravity Anomalies, Geoid Undulations, and Deflections of the Vertical Implied by Anomaly Degree Variance Models. Department of Geodetic Science and Surveying, The Ohio State University, Report No 208; 1974.

[33] Garcia ES, Sandwell DT, Smith WHF. Retracking CryoSat-2, Envisat and Jason-1 radar altimetry waveforms for improved gravity field recovery. Geophysical Journal International. 2014;196(3):1402–1422. Available from: http://dx.doi.org/10.1093/gji/ggt469.

[34] Zhang S, Sandwell DT. Retracking of SARAL/AltiKa radar altimetry waveforms for optimal gravity field recovery. Marine Geodesy. 2017;40(1):40–56.

[35] Forsberg R, Tscherning C, Knudsen P. An overview manual for the GRAVSOFT. Copenhagen, Denmark; 2008.

[36] Scharroo R, Leuliette E, Lillibridge J, Byrne D, Naeije M, Mitchum G. RADS: Consistent multi-mission products. In: Proc. of the Symposium on. vol. 20; 2013. p. 4.

[37] Scharroo R. RADS RDSAR Algorithm Theoretical Basis Document, Version0. 3, CP4O Project Report, 2014-updated May 2016. http://www satoc eu/projects/CP4O/docs/tud_rdsar_atbd pdf. 2016;.

[38] Jain M, Andersen OB, Dall J, Stenseng L. Sea surface height determination in the Arctic using Cryosat-2 SAR data from primary peak empirical retrackers. Advances in Space Research. 2015;55(1):40–50.

[39] Brown G. The average impulse responce of a rough surface and its applications. IEEE Journal of oceanic engineering. 1977;2(1):67–74.

[40] Ray C, Martin-Puig C, Clarizia MP, Ruffini G, Dinardo S, Gommenginger C, et al. SAR altimeter backscattered waveform model. IEEE Transactions on Geoscience and Remote Sensing. 2015;53(2):911–919.

[41] Kaas E, Sørensen B, Tscherning CC, Veicherts M. Multiprocessing least squares collocation: Applications to gravity field analysis. Journal of Geodetic Science. 2013;3(3):219–223.

[42] Allan T, Morelli C. A geophysical study of the Mediterranean sea. Nato Subcommittee on oceanographic Research. Technical reports; 1971.

[43] Barzaghi R, Carrion D, Vergos G, Tziavos I, Grigoriadis V, Natsiopoulos D, et al. GEOMED2: High-Resolution Geoid of the Mediterranean. Springer. 2018;.

[44] Sandwell DT, Müller RD, Smith WH, Garcia E, Francis R. New global marine gravity model from CryoSat-2 and Jason-1 reveals buried tectonic structure. Science. 2014;346(6205):65–67.

DTU Space
National Space Institute
Technical University of Denmark

Elektrovej 328
DK-2800 Kgs. Lyngby

Tel +45 4525 9500
Fax +45 4525 9575

http://www.space.dtu.dk